Cy. 1

DETERMINATION OF THE EXCITED STATE DENSITY

DISTRIBUTION WITHIN A NONEQUILIBRIUM,

FREELY EXPANDING ARGON ARCJET PLUME

Property of U. S. Air F.
F40600-7...

ENGINE TEST FACILITY
ARNOLD ENGINEERING DEVELOPMENT CENTER
AIR FORCE SYSTEMS COMMAND
ARNOLD AIR FORCE STATION, TENNESSEE 37389

March 1977

Final Report for Period 1 July 1974 — 1 January 1976

Approved for public release; distribution unlimited.

Prope...
F40...1

Prepared for

DIRECTORATE OF TECHNOLOGY
ARNOLD ENGINEERING DEVELOPMENT CENTER
ARNOLD AIR FORCE STATION, TENNESSEE 37389

This report has been reviewed by the Information Office (OI) and is releasable to the National Technical Information Service (NTIS). At NTIS, it will be available to the general public, including foreign nations.

APPROVAL STATEMENT

This technical report has been reviewed and is approved for publication.

FOR THE COMMANDER

MARION L. LASTER
Research & Development
  Division
Directorate of Technology

ROBERT O. DIETZ
Director of Technology

REPORT DOCUMENTATION PAGE		READ INSTRUCTIONS BEFORE COMPLETING FORM
1. REPORT NUMBER AEDC-TR-77-23	2. GOVT ACCESSION NO.	3. RECIPIENT'S CATALOG NUMBER
4. TITLE (and Subtitle) DETERMINATION OF THE EXCITED STATE DENSITY DISTRIBUTION WITHIN A NONEQUILIBRIUM, FREELY EXPANDING ARGON ARCJET PLUME		5. TYPE OF REPORT & PERIOD COVERED Final Report, 1 July 1974 – 1 January 1976
		6. PERFORMING ORG. REPORT NUMBER
7. AUTHOR(s) C. C. Limbaugh, ARO, Inc.		8. CONTRACT OR GRANT NUMBER(s)
9. PERFORMING ORGANIZATION NAME AND ADDRESS Arnold Engineering Development Center (DY) Air Force Systems Command Arnold Air Force Station, TN 37389		10. PROGRAM ELEMENT, PROJECT, TASK AREA & WORK UNIT NUMBERS Program Element 65807F
11. CONTROLLING OFFICE NAME AND ADDRESS Arnold Engineering Development Center (DYFS) Arnold Air Force Station, TN 37389		12. REPORT DATE March 1977
		13. NUMBER OF PAGES 126
14. MONITORING AGENCY NAME & ADDRESS(if different from Controlling Office)		15. SECURITY CLASS. (of this report) UNCLASSIFIED
		15a. DECLASSIFICATION/DOWNGRADING SCHEDULE N/A

16. DISTRIBUTION STATEMENT (of this Report)

Approved for public release; distribution unlimited.

17. DISTRIBUTION STATEMENT (of the abstract entered in Block 20, if different from Report)

18. SUPPLEMENTARY NOTES

Available in DDC.

19. KEY WORDS (Continue on reverse side if necessary and identify by block number)

radiation
spectra
collisions
energy transfer

arc-jet engines
distribution functions
excited state densities
nonequilibrium flow

20. ABSTRACT (Continue on reverse side if necessary and identify by block number)

The distribution of the population densities of the excited states of argon was determined at two axial positions in the non-equilibrium, freely expanding plume of an argon d-c arcjet. Narrow-line absorption and concomitant radial inversion were used to obtain densities of the first four excited states of argon, which include the two metastable and two resonance states. Abel inversion of the absolute radiance measurements of emission from

DD FORM 1473 1 JAN 73   EDITION OF 1 NOV 65 IS OBSOLETE

20. ABSTRACT (Continued)

several spectral lines provided the number density of highly excited states, the excitation or electron temperature, and the electron number density. The distribution functions observed were decidedly nonequilibrium, with the first four excited states ranging from a factor of two to a factor of ten larger than that required for Saha equilibrium with the free electron density. Calculations of the predicted distribution function were made by solution of a set of Eigenstate Rate Equations coupled with the effects of a free-jet gas dynamic expansion. Results of the calculations suggest that the Gryzinski form of the collisional excitation and de-excitation cross sections predicts a stronger collisional coupling between excited states and a slightly faster rate of recombination than were observed in the experimental data. Except for the low-lying states, which are strongly dependent upon the detailed form of the cross sections, the excited state population density predictions were within the known uncertainties of measured recombination rates.

PREFACE

CONTENTS

ILLUSTRATIONS

TABLES

APPENDIXES

1.0 INTRODUCTION

1.1 APPROACH AND OBJECTIVE

It is a general characteristic of high enthalpy gas flows that some of the gas species can be in highly excited internal energy states. The extent of this excitation is, of course, dependent upon the identity of the specie and the particular method by which energy is introduced into the gas. When the gas conditions are such that a high collision frequency is maintained, the available energy is partitioned among the various modes according to well-known classical thermodynamic concepts. In this case, observation of certain microscopic quantities (for example, the radiance of emitted spectral radiation) will indicate the physical state (temperature and density) of the gas, and the energy contained in the other modes can be determined via the equipartition theorem. In other cases, however, the gas flow process may be such that the collision frequency is decreased quickly, for instance by a rapid expansion into vacuum, and the gas species in some highly excited states will not undergo a sufficient number of collisions to distribute the internal energy into other energy modes in a manner described by equilibrium concepts. Freezing of rotational and vibrational energy states during a gas expansion are well-known examples of such nonequilibrium behavior (Ref. 1).

When the method of excitation involves collisional energies sufficiently large to produce ionization, the internal electronic states of the specie can become occupied. Such excitations of electronic states can be observed in arc-heated and radio frequency-heated gases, and the excited state distribution may contain a significant portion of the total energy in the gas. Measurements made in such a nonequilibrium environment must be interpreted carefully, since the usual classically derived analysis techniques for excited state distribution functions may be invalid.

The carefully choreographed sequence of excitation followed by a rapid, severe reduction in collision frequency resulting in nonequilibrium behavior occurs often in aerospace applications, particularly when low densities are involved, as in reentry phenomena and shock tubes. However, nonequilibrium phenomena generally represent a little-understood and largely unexplored aspect of the physics of high enthalpy gases. Because nonequilibrium phenomena do occur frequently in certain aerospace applications, yet are largely not well understood, there has been a continuing study at AEDC of the fundamental mechanisms by which nonequilibrium excited state distribution functions are established. Because the study does represent an extension of the state of the art, the approach has been one of careful progress, in which confidence in results was established before each new step was taken. The present document summarizes the progress of the study to date and presents recent experimental results, detailing measurements to ascertain the actual distribution of excited electronic states in a particular non-equilibrium environment.

The principal specific objective of the present work was to experimentally determine the spatially resolved population density to selected excited electronic states of monatomic argon in the plume of a freely expanding argon arcjet. This direct determination of excited state densities provides a unique opportunity to compare measured densities with calculated predictions of the excited state densities based upon the approach developed previously (Refs. 2 and 3). This comparison was a corollary objective of the work.

1.2 BACKGROUND

The principal theoretical efforts in nonequilibrium phenomena in plasmas at AEDC in recent years have been to examine the fundamental system of differential equations which describe the transient behaviour of each of the quantum states available to the plasma. This system of

equations, called the eigenstate rate equations (ERE), is mathematically similar to the chemical rate equations, though considerably more complex when applied to individual internal energy states within a single chemical specie. The fundamental validity of the numerical solution to the system of equations has been examined, and the importance of the role of low-lying metastable quantum states on the upper state distribution function for hydrogen plasmas (Ref. 2) has been assessed. In later work the hydrogenic case was extended to helium plasmas (Refs. 3 and 4), and the coupled mechanisms by which the quantum state distributions decay in time were examined. The findings of these studies suggested that the mechanisms for energy transfer among electronic states are indeed complex and subtle and truly require a coupled mathematical system of eigenstate rate equations for an adequate (mathematical) description. One aspect of note in previous work was the approximate modeling of a physical situation in which gas bulk properties were expanding toward a lower density environment. The results of that study showed that electronic state density relaxation times could become significant with respect to typical gas expansion times, necessitating inclusion of these microscopic (collisional) effects upon the macroscopic (gas dynamic) effects (Ref. 5).

Much of the previous experimental work at AEDC with the arcjet has been directed toward utilization of the device and its nonequilibrium environment for studies of high speed wind tunnel diagnostics (Ref. 6). It was recognized that with argon, as well as some other gases, large population densities of metastable states could occur and affect interpretation of spectral data obtained from such environments (Refs. 7 and 8).

The nonequilibrium arcjet plume environment has been used to provide fundamental knowlege of excited state collisional processes (Ref. 9). In addition to the work at AEDC, there have been numerous other experimental investigations affected by one aspect of nonequilibrium or another but generally with some major objective other than the study of nonequilibrium phenomena (for example, determination of electro-atom

9

recombination rates, Ref. 10, and identification of the physical pro-
cesses responsible for afterglow phenomena, Ref. 11. Robben, Kunkle, and
Talbot (Ref. 12) made experimental determinations of the excited specie
number densities in the free expansion of a helium arcjet plasma. Their
work showed a definite nonequilibrium character of the excited state
distribution function. However, their experimental work was confined to
emission spectroscopy; hence they report no excited state densities below
quantum level three.

In 1973 Park (Refs. 13 and 14) reported on results of calculations
and measurements made in an expanding nozzle flow with a nitrogen-hydrogen
mixture. He concluded that a nonequilibrium distribution of the elec-
tronic state population density is to be expected in a supersonic expan-
sion of an ionized gas and that the observed excitation temperature of
the distribution is markedly higher than the free electron temperature.
Park's work included measurement and prediction of excited state densi-
ties in an atomic nitrogen and hydrogen mixture in a recombining nozzle
flow. The results show adequate confirmation of the theoretical pre-
dictions. However, the technique used to predict excited state densities
(Ref. 15) is based upon a quasi-steady state approximation in which the
time derivative of excited state densities is assumed to be zero and
thus does not include transient coupling between the specie and the
flow field conditions. Furthermore, the experimental situation was such
that quasi-steady state conditions would be expected to prevail. Other
works published recently (Refs. 16 and 17) have also attacked the
problem of the determination of excited state densities in plasmas.
Hogarth and McElwain (Ref. 16) examined the transient decay of a dense
hydrogen plasma from an initial nonequilibrium distribution function to
the equilibrium distribution. Hey (Ref. 17) showed that low-lying
metastable states play a very important role in the determination of
excited state densities in atomic species. The results of both these
works are in qualitative agreement with the earlier work described above
(Refs. 2 and 5). Quantitative comparisons are not possible because of the
different specific problems being solved.

In summary, it should be pointed out that, although comparisons of predicted and measured excited state distributions in nonequilibrium environments have been accomplished in the past, quasi-steady state conditions have been assumed theoretically and chosen experimentally. The present work is the first reported in which the distribution function is determined experimentally and theoretically in a nonequilibrium environment in which the quasi-steady state approximation is not an a priori assumption.

2.0 ANALYTIC DEVELOPMENTS

2.1 INTRODUCTION

The work reported here required analytic developments in two areas. The first area is the development of a technique to obtain excited state number densities from atomic spectral line absorption data. The absorption data obtained in the work are spatially resolved, integrated profiles across the extent of the plume, and an inversion technique to solve the radiative transport problem for the radially dependent number densities is required. The details of this inversion technique, based upon an "onion peel" model, are given in Appendix A.

The second area is an extension of the mathematical system of nonlinear coupled differential equations called the eigenstate rate equations (ERE), developed previously (Refs. 2 through 5). The system of equations is adapted for the freely expanding argon plasma and, as developed here, serves as a first approximation to a mathematical model for the description of the quantum state densities in an expanding, relaxing, ionized gas such as the freely expanding arcjet plume. The considerations for this development are described in the following sections.

2.2 EIGENSTATE RATE EQUATIONS COUPLED WITH GAS DYNAMICS

As a partially ionized monatomic gas expands from an arcjet nozzle into a vacuum environment, the atoms in a particular excited state are subject to two physical processes affecting the density at any point in space. One process is the change in density caused by radiation and inelastic collisions with the flow constituents (electrons, atoms, and ions), and the second process is the change in density caused by the gas dynamic expansion. The second of these effects can be thought of as being position dependent (expansion), whereas the first process depends ultimately upon the number and type of particles interacting and the probability of an atomic state transition during a collision. The mathematical description of these processes is best attacked through the one-dimensional, total time derivative of the density of some excited state at some position, X, in the stream; thus,

$$\frac{dn(p)}{dt} = \frac{\partial n(p)}{\partial t} + \frac{\partial n(p)}{\partial X} \frac{\partial X}{\partial t} \tag{1}$$

In Eq. (1) n is the population density in some p^{th} excited state, t is time, and X is the position coordinate. There is no loss of generality in Eq. (1) when X is referenced to some constant dimension such as a nozzle diameter. Implicit in Eq. (1) is the assumption that the position can be written as a function of time.

The first term of Eq. (1) is taken to mean the change in the density of state p because of the instantaneous particle interactions. The physical processes comprising this term have been described in depth elsewhere (Ref. 3) and will only be summarized here. Briefly, each of the mechanisms causing a change in the population density of a particular eigenstate can be characterized by a rate coefficient. The instantaneous rate by which the level is being populated or depopulated by a given mechanism is the product of the rate coefficient and the number density of the reaction partners. The mechanisms included in this study can be listed as follows:

1. Inelastic and superelastic electron-atom collisions characterized by the rate coefficient, $K(p;q)$.

2. Electron-ion radiative recombination characterized by the rate coefficient, $\beta(p)$.

3. Three-body electron-electron-ion recombination characterized by the rate coefficient, $K(c;p)$.

4. Electron-atom collisional ionization characterized by the rate coefficient, $K(p;c)$.

5. Spontaneous radiative transitions characterized by the Einstein spontaneous transition probabilities, $A(p;q)$.

Both processes (1) and (5) can either populate or depopulate a specific level; processes (2) and (3) can only populate; and process (4) can only depopulate.

In addition to the above processes, other phenomena can contribute to the change in population density of an eigenstate. These processes are: 1) atom-atom and atom-ion collisions, 2) induced emission, and 3) molecular ion effects. At the low densities and temperatures of this study these effects are negligible with respect to the other physical processes. It should be pointed out that it was necessary to include some photon absorption considerations in this work. The absorption was handled in an approximate manner, and the technique is described in Section 2.3.2.

The time rate of change of the population density of state p because of these collisiional and radiative processes is simply the algebraic

sum of the five basic processes described above:

$$\frac{\partial n(p)}{\partial t} = - n_e n(p) \sum_q K(p;q) - n_e n(p) K(p;c) - n(p) \sum_{q<p} A(p;q)$$

$$+ n_e \sum_q n(q) K(q;p) + \sum_{q>p} n(q) A(q;p)$$

$$+ n_e^2 n^+ K(c;p) + n_e n^+ \beta(p) \tag{2}$$

In Eq. (2), p and q symbolically represent the quantum numbers necessary to identify a particular state, ne is the free electron density, $n(p)$ is the density of the pth state, and the rate coefficients have been defined previously. In the formulation of Eq. (2) all $K(p;p)$ values are zero, and any $A(p;q)$ value is zero if the dipole selection rules are violated.

In Eq. (2) the first three terms express the rate with which state p is depopulated because of collisional internal transitions, process (1); collisional ionization, process (4); and spontaneous radiative transitions, process (5), respectively. The remaining terms express populating rates because of collisional internal transitions, process (1); radiative transitions, process (5); three-body recombination, process (3); and radiative recombination, process (2).

There will be a similar equation for each eigenstate available to the atom. In addition, the free electron density, n_e, enters into each equation as a product with each of the other bound state densities. Hence, the resultant system of equations is a rectangular nonlinear system of infinite extent. Assuming single ionization and taking advantage of charge neutrality so that the electron and ion densities are identical, the conservation of heavy particles is expressed by the equation

$$\Sigma \; n(p) + n_e = n_s \tag{3}$$

where n_s is the heavy particle number density. Equation (3) added to the system causes the system of equations represented by Eqs. (2) and

(3) and comprising the first term of Eq. (1) to become square and, in principle, determinate.

The second term in Eq. (1) expresses the effect on the density of the pth state due to the gas dynamic expansion. The description of such processes is best attacked through the application of the principles of conservation of mass, energy, and momentum. When applied to a physical situation of the type encountered here, this usually results in a hyperbolic partial differential equation, requiring a method of characteristics numerical approach for solution but not including the additional terms introduced by Eq. (2). Rather than introduce this complication into an already complex mathematical model, one can make some simplifying assumptions. These assumptions may be listed as follows:

1. The major forces acting upon the ions are gas dynamic in nature.

2. The major forces acting upon the electrons are electrostatic in nature.

3. The gas is inviscid and non-heat-conducting.

4. Perfect gas relationships are valid.

5. The Ashkenas-Sherman model (Ref. 18) holds true for description of the Mach number on the centerline of the arcjet plume.

The first two of these assumptions merely express the fact that the electron is approximately five orders of magnitude less massive than the singly ionized argon ion and that there is no charge separation. Thus the elastic collisional interactions between heavy bodies will

15

dominate the gas flow processes, and the gas dynamical processes will
determine the spatial position of the ions, whereas the much lighter
electrons will be constrained by electrostatic forces to follow the
density variations of the ions.

Assumptions (3) and (4) make possible simple evaluations of bulk
gas properties. In particular, assumptions (3) and (4) will be used
to apply the isentropic relations to determine the static gas properties
and sonic velocity at a point in space. The use of these relations is
perhaps inconsistent with the underlying motivation of this work since
equilibrium relations are implied. A more correct description is beyond
the current state of the art. At the current stage of development these
simplifying relations are necessary for estimation of the bulk properties.

Finally, assumption (5) is used to provide a simple expression of
the Mach number on the centerline of the arcjet plume. The use of the
Ashkenas-Sherman model (Ref. 18) has been documented previously for
application to arcjet plumes (Refs. 19 and 20) and is at least partially
a result of assumptions (3) and (4). With these assumptions, the second
term in Eq. (1) can be expressed as follows:

$$\frac{\partial n(p)}{\partial X} = \frac{n(p)}{n_s} \frac{\partial n_s}{\partial X} \qquad (4)$$

where n_s is the heavy particle number density. Equation (4) expresses
the conclusion that the spatial variation of a specific state density
is proportional to the spatial variation of the static density. The
static density can be determined from the isentropic relationship

$$\frac{n_s}{n_o} = \left(1 + \frac{\gamma - 1}{2} M^2 \right)^{-1/(\gamma-1)} \qquad (5)$$

where n_o is the density at some reference condition where M = 0. The
Mach number is determined from the Ashkenas-Sherman relation (Ref. 18)
as follows:

16

$$M = A\left(\frac{X}{D} - \frac{X_o}{D}\right)^{\gamma-1} - \frac{\frac{1}{2}\left(\frac{\gamma+1}{\gamma-1}\right)}{A\left(\frac{X}{D} - \frac{X_o}{D}\right)^{\gamma-1}} + \frac{C}{\left(\frac{X}{D} - \frac{X_o}{D}\right)^{3(\gamma-1)}} \qquad (6)$$

where

$$\gamma = 1.67$$
$$A = 3.26$$
$$C = 0.31$$
$$\frac{X_o}{D} = 0.075$$

In Eq. (6) X is the axial distance from the nozzle exit plane and D is the nozzle diameter. Finally, the space-dependent portion of Eq. (1) can be written

$$\frac{\partial n(p)}{\partial X} \frac{\partial X}{\partial t} = \frac{n(\rho)}{n_s} \frac{\partial n_s}{\partial M} \frac{\partial M}{\partial X} M \sqrt{\gamma RT} \qquad (7)$$

where R is the gas constant and T is the gas static temperature.

The system of equations formed by substituting Eqs. (7), (3), and (2) into Eq. (1) for each quantum state for the argon plasma forms the basis for the mathematical model of the distribution function for the excited electronic states. Although the system is infinite in extent because of the infinite number of excited states, thus making the solution impossible, it may be truncated at some finite energy level as a reasonable approximation. The considerations for this have been described previously (Ref. 3) and are not repeated here. An additional practical constraint was available computer core and computer time to effect a solution to the system of equations. Thus it was determined to truncate the system at the 5d $[7/2]_3$ quantum state. All energy levels above the truncation level were averaged together as one additional state at higher energy than the 5d $[7/2]_3$ quantum state. This and other averaging discussed below resulted in a system of 46 differential equations for the unknown quantum state population densities and the free electron density. The resultant system of equations is

17

nonlinear and coupled and provides a complete transient description
of the population density of each separate quantum state as the gas
expands and undergoes collisional-radiative transitions, within the
limits of the physical model.

Because of the size and the nonlinearly coupled nature of the
system of equations, solution was effected on a large-scale digital
computer by the application of numerical techniques. The numerical
technique used here, the Modified Euler's Method, applies straightfor-
wardly by noting that the time rate of change of the population density
of each quantum state is an explicit function of the population density
of all the other quantum states and the electron density and an
implicit function of electron temperature and time. The salient explicit
equations were developed and programmed for an IBM S370/165 digital
computer at AEDC.

2.3 FUNDAMENTAL DATA

A large amount of fundamental atomic data is required to effect
the solution to the system of equations represented by Eq. (1). Some
of these data are readily available in the literature; others must be
calculated.

2.3.1 Energy Levels

The energy levels of the argon atom were taken from Moore (Ref. 21).
Not all of the levels listed by Moore were used uniquely; practical
limitations of available computer core and computer time precluded use
of all the known levels. Rather, selected sets of quantum levels were
averaged together and considered as one quantum state. The basis for
selection of those levels to be averaged together is not clearly quanti-
fiable, being based upon a judgement formed from inspection of the
relative energies of the levels to be averaged, whether the transition

18

between the averaged levels was dipole allowed or forbidden, and whether or not quantitative knowledge of the number density of the specific energy level would be necessary for later analysis. In general, those energy levels separated by more than 400 cm^{-1} were never averaged, and a greater energy level spacing within a set of averaged levels was permitted if transitions between the levels were dipole allowed. Those specific sets of energy levels which were averaged together are listed in Table 1.

Table 1. Sets of Averaged Argon Quantum States

1. $4p\left[1/2\right]_0$, $4p^-\left[3/2\right]_1$

2. $3d\left[1/2\right]_0$, $3d\left[1/2\right]_1$, $3d\left[3/2\right]_2$

3. $3d\left[5/2\right]_2$, $5s\left[3/2\right]_2$

4. $5s\left[3/2\right]_1$, $3d\left[5/2\right]_3$

5. $3d^-\left[5/2\right]_2$, $3d^-\left[3/2\right]_2$, $3d^-\left[5/2\right]_3$, $5s^-\left[1/2\right]_0$

6. $5s^-\left[1/2\right]_1$, $3d^-\left[3/2\right]_1$, $5p\left[1/2\right]_1$, $5p\left[5/2\right]_3$

7. $5p\left[1/2\right]_0$, $5p^-\left[3/2\right]_1$, $5p^-\left[1/2\right]_1$, $5p^-\left[3/2\right]_2$, $4d\left[1/2\right]_0$, $4d\left[1/2\right]_1$

8. $4d\left[7/2\right]_3$, $4d\left[5/2\right]_2$

9. $6s\left[3/2\right]_2$, $6s\left[3/2\right]_1$

10. $4f\left[9/2\right]_5$, $4f\left[9/2\right]_4$, $4f\left[5/2\right]_3$, $4f\left[5/2\right]_2$, $4f\left[7/2\right]_4$, $4f\left[7/2\right]_3$

11. $4d^-\left[3/2\right]_2$, $4d^-\left[5/2\right]_2$

12. $4d^-\left[3/2\right]_1$, $6p\left[1/2\right]_1$, $6s^-\left[1/2\right]_0$, $6s^-\left[1/2\right]_1$, $6p\left[5/2\right]_3$, $6p\left[5/2\right]_2$, $6p\left[3/2\right]_1$, $6p\left[3/2\right]_2$, $6p\left[1/2\right]_0$, $6p\left[1/2\right]_1$

13. $4f^-\left[7/2\right]_4$, $4f^-\left[7/2\right]_3$, $4f^-\left[5/2\right]_3$, $4f^-\left[5/2\right]_2$

14. All states above $5d\left[7/2\right]_3$

The spectroscopic notation used in this work is based upon the jK coupling scheme (Ref. 22), and is explained fully in Ref. 9. Following this procedure the excited argon atom was modeled by a system of equations encompassing 46 energy levels. The last equation, describing the sum of the densities for all excited states above the $5d \, [7/2]_3$ level, acted as a reservoir to provide for radiation and collisional transitions to the other nearby upper states.

2.3.2 Einstein Spontaneous Transition Probabilities

The Einstein transition probabilities, $A(p;q)$, were taken from Wiese (Ref. 23) for those transitions which have been amenable to experiment. This provided most of the transitions among the lower excited states. For transitions among the higher excited states, which are required for completeness and correctness, the hydrogenic approximation was made and the transition probabilities were calculated using the hydrogen matrix elements listed by Green, Rush, and Chandler (Ref. 24).

The transition probabilities used for these investigations included many radiative transitions to the ground state. These transitions are highly energetic, generally having wavelengths less than 100 nm, as well as very large oscillator strengths, implying large absorption cross sections. Calculations with the ERE were performed under two assumptions concerning the optical opacity of the plasma to these resonance transition wavelengths: optically thin and optically thick. The optically thin assumption (the radiative transitions to the ground state are allowed) was useful for making comparions to certain theoretical parameters in the literature. The optically thick assumption, used for more accurate modeling of the experiment, was accomplished by simply making all transition probabilities to the ground state zero. It should be pointed out that this approach is somewhat artifical. However, correct accounting of absorption effects would introduce additional complications beyond the scope of the present work.

2.3.3 Two-Body Collisional Rate Coefficients

The two-body collisional rate coefficients, K(p;q), are in fact
the result of integrating the cross section for the transition over the
energy distribution function of the free electrons; the procedure has
been described in greater detail prevously (Ref. 3). The free electron
energy distribution in this work is assumed to be Maxwell-Boltzmann, and
the energy-dependent cross sections are assumed to be expressed by the
Gryzinski formulation (Refs. 25, 26, and 27).

The application of the Gryzinski formulation for determining
excitation cross sections for helium transitions was examined closely
in Ref. 3. The computations were facilitated because the helium wave
functions are quite well known and the description of collisional
processes in helium has been attacked on a broad front, both theoretically
and experimentally. The situation for argon is not so simple. The
argon atom, although a noble gas atom like helium, is considerably more
complex and is difficult to treat theoretically. Detailed experimental
measurements and quantum mechanical calculations of excitation cross
sections from the ground state to excited states are relatively scarce,
and experimental cross section data describing transitions between
excited states are not found in the literature. Comparisons of the
ground state to excited state cross sections for argon calculated by
the Gryzinski formulation to measurements found in the literature (Ref.
28) are listed in Table 2. The tabulation compares only the maximum
values obtained by calculation and experiment. These transitions,
for excitations from the ground state, are all dipole-forbidden transi-
tions, the least probable transitions, and as is seen from Table 2, the
calculations underestimate the experiments by typically a factor of
three.

Table 2. Comparison of Excitation Cross Sections for Argon
by Calculation and Experiment*

Initial State	Final State	$\dfrac{Q_{max}\ \text{Calc}}{Q_{max}\ \text{Exp}}$	Dipole Allowed or Forbidden
$3p^6$ 1S	$4p\,[1/2]_1$	0.21	Forbidden
	$4p\,[5/2]_3$	0.38	
	$4p\,[5/2]_2$	0.32	
	$4p\,[3/2]_1$	0.63	
	$4p\,[3/2]_2$	0.37	
	$4p\,[1/2]_0$	0.98	
	$4p^{\prime}\,[3/2]_1$	0.51	
	$4p^{\prime}\,[3/2]_2$	0.57	
	$4p^{\prime}\,[1/2]_1$	0.82	
	$4p^{\prime}\,[1/2]_0$	0.39	

*Ref. 28

Figure 1 shows a comparison of the Gryzinski calculations to
quantum mechanical cross section calculations (Ref. 29) for the
electron collisional excitation of the $4s^{\prime}\,[1/2]_1$ state from the
argon ground state. In Fig. 1 the ordinate is the cross section
(cm^2), and the abscissa is the ratio of the kinetic energy of the
colliding electron to the threshold energy for the excitation. This
transition is dipole allowed. As is seen, in this case the
Gryzinski formulation overestimates the quantum mechanical calcu-
lation by typically a factor of two. Thus, assuming that this
agreement is typical for the other dipole-allowed transitions, one
would expect the calculations reported here to show a much higher
collisional efficiency and approach an equilibrium configuration
more rapidly than is the actual physical case.
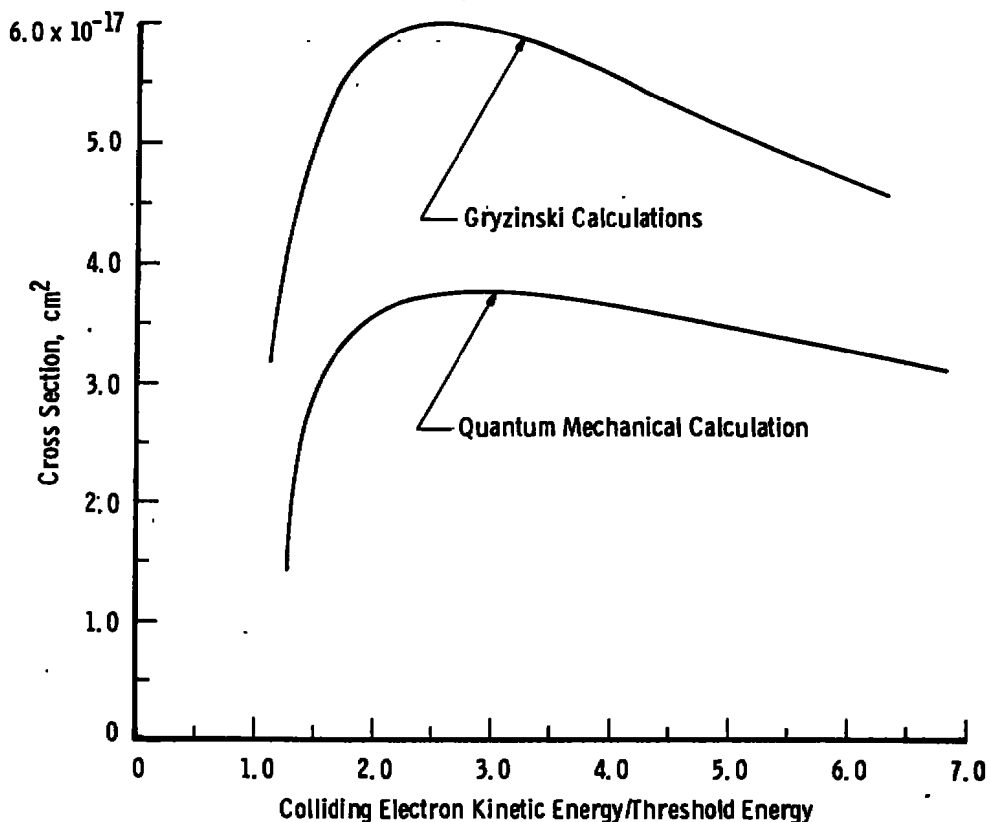
Figure 1. Argon 4s states electron-atom excitation cross section.

The preceding discussion has been concerned only with inelastic excitation between bound states of the atom. The inverse process, a collision resulting in de-excitation of the atom, with the excess energy in the reaction being carried away as kinetic energy of the electron, is also included in this study. The rate coefficients for these processes come quite easily from equilibrium considerations (Ref. 3).

2.3.4 Collisional Ionization and Three-Body Recombination Coefficients

The collisional ionization cross section is very readily obtained from the two-body internal transition cross section. Figure 2 shows the results of the Gryzinski calculations for the ionization cross

section of the ground state argon atom and the results of Born approximation calculations reported by Wallace, Berg, and Green (Ref. 30). In Fig. 2 the ordinate is the cross section (cm^2) and the abscissa is the ratio of the kinetic energy of the electron to the ionization energy of the ground state of the argon atom. As is seen in Fig. 2, the Gryzinski cross sections underestimate the more satisfying quantum mechanical calculations by typically a factor of two. The quantum mechanical calculations showed more favorable comparison to experiment.
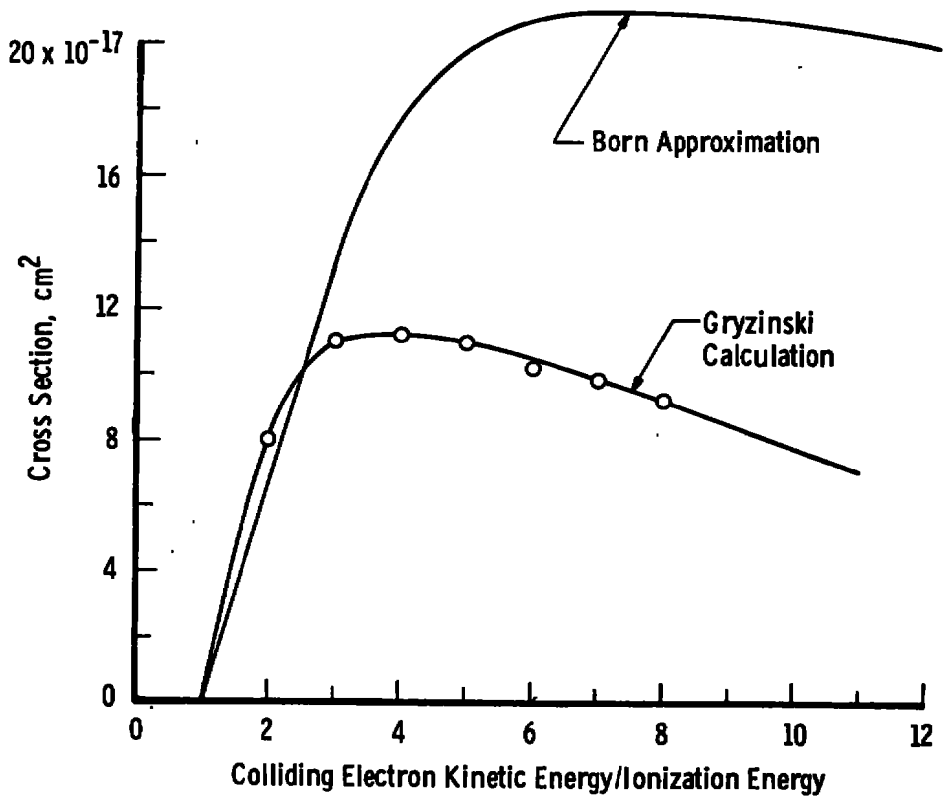

Figure 2. Argon ground state electron-atom collisional ionization cross sections.

The inverse of collisional ionization, three-body recombination, is described by the rate coefficient $K(c;p)$ and is obtained from equilibrium considerations in a manner similar to that for $K(q;p)$ (Ref. 3).

2.3.5 Radiative Recombination Rate Coefficients

The radiative recombination rate coefficient describes the filling
of state p because of two-body encounters between electrons and ions
in which the ion captures the electron into energy state p with the
attendant emission of radiation. It is obtained in much the same way
as the other rate coefficients although there is some difference in the
analytical procedure. The cross sections are based upon a hydrogenic
approximation (Ref. 31) and, because of this approximation, one
would expect the calculations to give their worst results for the
lower quantum levels and to converge to correct values for the upper
levels. Comparison of the photoionization cross section with pub-
lished results (Ref. 32) shows that, for the ground state, the hydro-
genic approximation underestimates the cross section by typically a
factor of five. The hydrogenic approximation is expected to provide
much better cross sections for the higher excited states, since the
physical model will be more correct for these states.

2.3.6 Collisional-Radiative Recombination Coefficients

The analytic work being reported here is unique; there are no
standards with which it can be compared for detailed evaluation. As
was shown in the preceding sections, where detailed experimental or
theoretical data are available the agreement with the expressions used
herein is not completely satisfying. Yet, in many instances the uncer-
tainty in the published data is sufficiently large that a significant
effort to improve the values used here is difficult to justify. Further,
for the mathematical model used here, the atoms in each excited state
are subjected to up to nearly 100 competing transitional processes, each
with its own rate coefficient, and each rate coefficient may be too
large or too small, depending upon the accuracy of the individual cross-
section determinations. Thus it is hoped that the statistical uncer-
tainty will tend to offset the individual inaccuracies of the cross
sections.

One means of evaluating the overall validity and consistency of
the various rate coefficients is by comparing the collisional-
radiative recombination (CRR) coefficients calculated by the ERE
model to independent calculations and experiments reported in the
literature. The CRR coefficients are based upon the plasma's being
in a so-called quasi-steady state condition in which the time rates
of change of the population densities of all excited states can be set
to zero. In this situation, which is in fact a most reasonable descrip-
tion when short time scales are not involved, the free electron density
rate of decay can be described as

$$\frac{\partial n_e}{\partial t} = -\alpha n_e^2 \qquad (8)$$

in which α is the CRR coefficient. The CRR coefficient has been
determined for argon both experimentally and by a variety of theoret-
ical calculations. With the ERE approach used here the CRR coeffi-
cient can be determined simply by allowing the calculations of the
distribution function to proceed, not including spatial and electron
temperature gradients, at a fixed electron density and temperature
until the quasi-steady state condition is established numerically. The
resultant electron density and its decay rate immediately yield the
CRR coefficient. The CRR coefficients determined by solution of the
ERE for the optically thin case at conditions of the work reported here
are shown in Table 3. Also included in Table 3 for comparison purposes
are values interpolated from results calculated by Wanless (Ref. 33) and
based upon the Gryzinski cross section. Wanless's calculated results
compared favorably with experimental results obtained by Chen (Ref. 34)
and were estimated to be accurate within a factor of two. As is seen,
agreement between the calculations is satisfactory, suggesting that,
in spite of the known inaccuracies in individual rate coefficients, these
errors appear to balance out for determination of gross properties.
The effect upon individual state properties cannot be evaluated without
detailed measurements for comparisons. These measurements have heretofore
not been made and are the subject of this work.

26

Table 3. Comparison of Argon Recombination Coefficients Determined from Quasi-Steady State Calculations and the Eigenstate Rate Equation Calculations

$T_e, °K$	N_e, cm^{-3}	$\alpha_{Wanless}, cm^3$	α_{ERE}, cm^3
7,650	1.15×10^{14}	2.8×10^{-11}	2.54×10^{-11}
7,200	1.5×10^{14}	4.6×10^{-11}	3.2×10^{-11}

Note: Quasi-steady state calculations appear in Ref. 33.

3.0 APPARATUS AND PROCEDURES

3.1 APPARATUS

3.1.1 Research Cell R-2E-1

The experimental portion of this study was performed in Research Cell R-2E-1 in the Gas Kinetics Laboratory of the AEDC Engine Test Facility (ETF). The research cell and related equipment for this work are shown schematically in Fig. 3. Research Cell R-2E-1 is a cylindrical test cell, nominally 31 cm in diameter, with its axis vertical. The cell is connected through a system of valves to two vacuum pumps capable of obtaining cell pressures below 0.08 torr.

The cell is split horizontally 97 cm and 150 cm above the floor to provide access to the apparatus and test sections of the cell. The lower section contains the arcjet, the axial positioning mechanism, and the control and instrumentation leads. The test section is nominally 53 cm in length and is removable to provide flexibility to meet requirements of specific experiments. For this work, which required optical viewing across the extent of the plume, the test section was constructed of four rectangular quartz plates, 23 cm wide and 25 cm high, mounted and sealed into top and bottom flanges of

mild carbon steel to provide mating to the other research cell section.
The quartz plates were arranged in a square centered on the cell axis.
The plates were joined together at the corners by Silastic® RTV as well
as at the mating flanges at top and bottom of the quartz plates to
provide both adhesion and sealing of the joints. Spacing and support
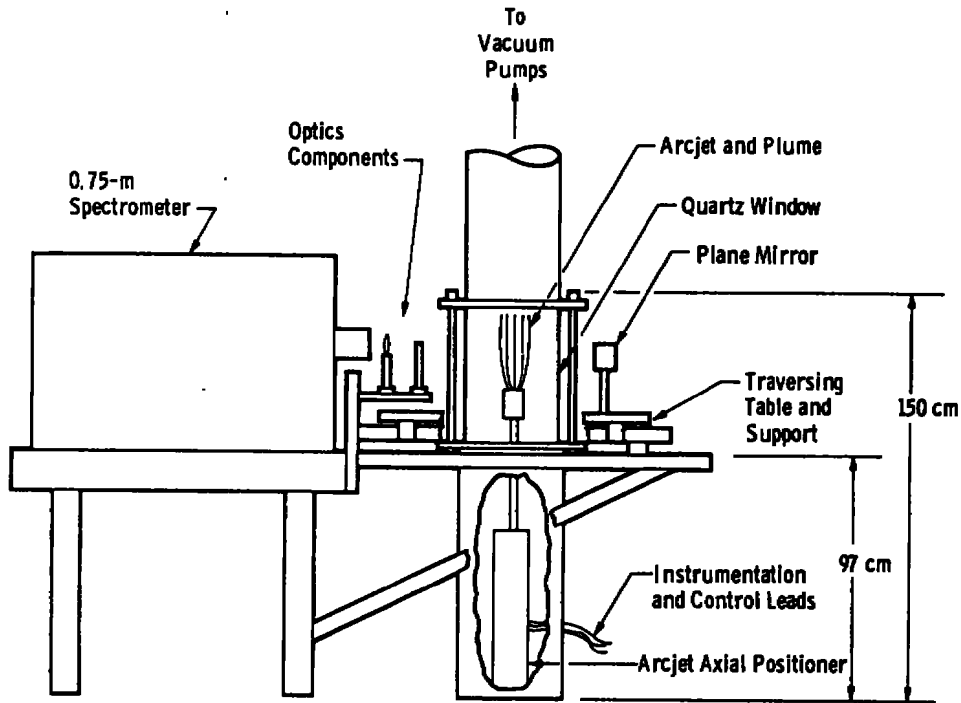of the top and bottom flanges are provided by four threaded rods.

Figure 3. Schematic of research cell and experimental apparatus.

3.1.2 Arcjet

The arcjet used in this work is of the Gerdien type and is similar
in concept to those arcjets constructed at AEDC and used in earlier
work such as that described in Ref. 35. Modifications based upon pre-
vious experience were incorporated, including a mechanism for adjusting
the electrode gap. The arcjet is constructed in three sections, each
section electrically isolated from the other, and each water cooled.
The arcjet assembly is about 15 cm in length and 7.6 cm in diameter.

The base section provides the cathode support as well as the mounting hardware to the apparatus for axial positioning of the arcjet. For this work a new arcjet head was designed and fabricated to provide better cooling of the copper nozzle. A cutaway view of this arcjet and gap adjuster presented in Fig. 4 shows the construction details. The nozzle provides a water seal at both top and bottom of the arcjet head and may be removed for repair or replacement. For the work reported here the nozzle was constructed of copper and had a diameter of 0.635 cm.
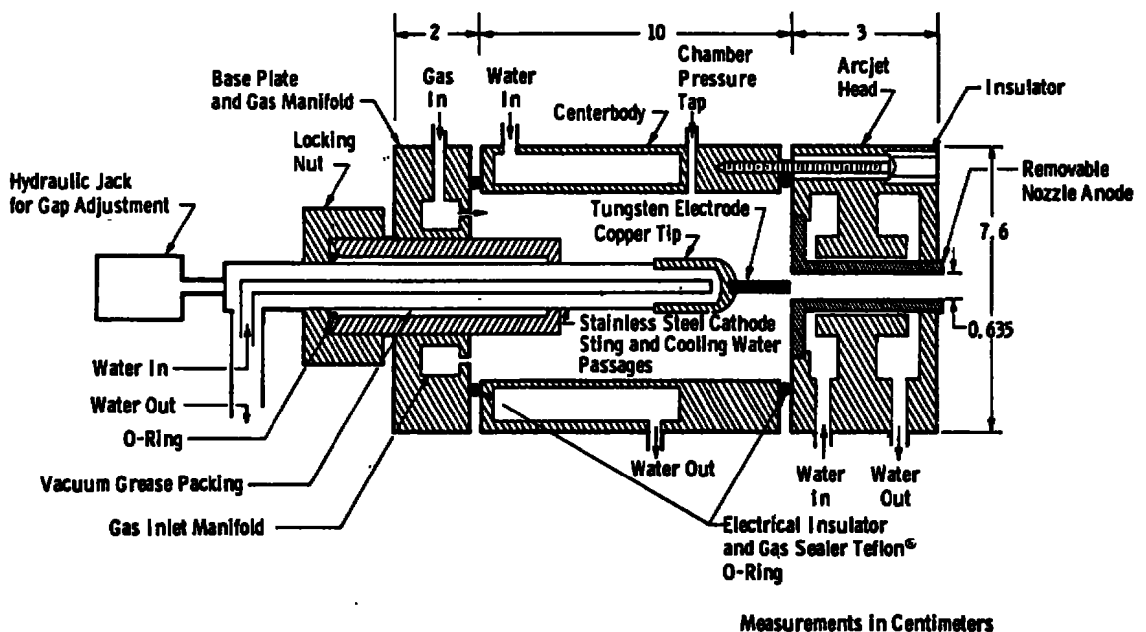
Figure 4. Arcjet and gap adjuster assembly schematic.

The cathode was a 0.3175-cm-diam, 2-percent thoriated tungsten welding rod, approximately 2.54 cm long and silver soldered into a copper heat sink which in turn was silver soldered to a hollow stainless steel sting passing through the base plate of the arcjet assembly. The hollow sting provided passages for water cooling of the cathode heat sink. This assembly was mounted to a small hydraulic jack that provided for adjustment of the arcjet electrode gap from 0.15 to 1.36 cm. Readout of the gap position was accomplished

with a hydraulic cylinder attached mechanically to the gap positioner.
The cylinder outlet was attached to an external scale by a 0.635-cm-OD
tygon tube. A multiplication factor of approximately 12 between the
hydraulic cylinder and the external scale made positioning of the
cathode within a tolerance of 0.01 cm possible.

Power to the arcjet was provided by a Miller® model SR-1000-B1
d-c power unit with a capability of providing 500 amp at 80 v DC.
The amperage of the argon arcjet was continuously variable from a
minimum of approximately 50 amp to a maximum in excess of 300 amp.

Positioning of the arcjet along the cell axis was accomplished
by a hydraulic jack with a nominal length of travel of 30 cm. The
position of the arcjet was determined by visually observing the
location of the jet nozzle exit plane on scales mounted on the cell
windows. Two identical scales on opposing windows of the cell were
used to prevent parallax.

The measurements taken to monitor the arcjet conditions were
the voltage, amperage, mass flow, chamber pressure, and test section
ambient pressure. The voltage and amperage were indicated by meters
for continuous measurement of power supplied to the arcjet. The
amperage was measured by the voltage drop across a calibrated resistor
shunt in the arcjet power supply line.

The argon mass flow rate through the arcjet was measured by use
of a calibrated Hastings® mass flowmeter. The Hastings flowmeter
had both visual meter readout and a signal proportional to the flow
which was recorded on a strip chart for continuous measurement. The
arcjet chamber pressure was measured by use of a calibrated pressure
transducer connected to a pressure tap through the centerbody as shown
in Fig. 4. The pressure transducer output signal was displayed on a
strip chart for continous measurement.

Two measurement systems were utilized for obtaining the pressure in the test cell. One of these, an Alphatron® gage, was unsuitable for quantitative work since the instrument was calibrated for air and used with an unknown mixture of argon and air. However, it was useful as a monitoring device to ensure that the cell pressure had no time-dependent variations. Quantitative cell pressure data were obtained from a calibrated McLeod® gauge.

The measurement instruments described above were used mainly to set repeatable conditions; the variables play no appreciable role in the excited state population determination. Therefore, no great attention to measurement error in these parameters is included in the present report.

3.1.3 Spectrometer and Light Source

The spectrometer used for the spectral radiance and spectral absorption measurements was a 0.75-m Spex® grating spectrometer having a 1,180-groove/mm grating blazed for maximum reflection at 750.0 nm. The entrance and exit slits had straight jaws and were set at 200 and 300 μ, respectively. The entrance slit height was set at 2 mm. The exit slit was set wider than the entrance slit to minimize errors caused by misalignment and drift of the grating drive mechanism while the wavelength was set on a particular spectral line. An RCA 1P28 and an Amperex 150 CVP photomultiplier tube were both used at separate times as detectors for the spectrometer. The RCA 1P28 photomultiplier tube, operated at 800 v, was used for the measurements of the radiant energy emission from the arcjet at wavelengths from 415.8 to 604.3 nm. The Amperex 150 CVP tube, operated at 1,100 v, was used for the measurement of the spectral absorption of the arcjet at wavelengths from 738.4 to 922.4 nm. To reduce the dark current, the Amperex 150 CVP photomultiplier tube was cooled by the boiloff from a liquid nitrogen dewar. A thermistor in the photomultiplier tube holder and cooler provided for monitoring the temperature of the

photomultiplier tube. The rate of boiloff of liquid nitrogen from the dewar was controlled by an immersible heater and variac arrangement.

The light source for the absorption measurements was provided by an argon discharge tube. The discharge tube was of standard design and has been described previously (Ref. 36). A schematic of the specific discharge tube used here, which was built specifically for this work, is shown in Fig. 5. Only argon gas was used in the discharge tube, and the supply was provided from a K-bottle through a gas regulator and needle valve to control the flow rate. The gas regulator was set to provide a pressure to the discharge supply line of approximately 760 torr. The needle valve was adjusted to maintain a constant pressure of 29.8 torr at the entrance to the discharge tube. The excitation voltage was supplied by a regulated high voltage power supply set at 3,000 v. A radiometer designed to monitor the 430.0-nm argon spectral radiation was used as a monitor for the discharge tube to assure that there were no transient variations throughout the data acquisition time.
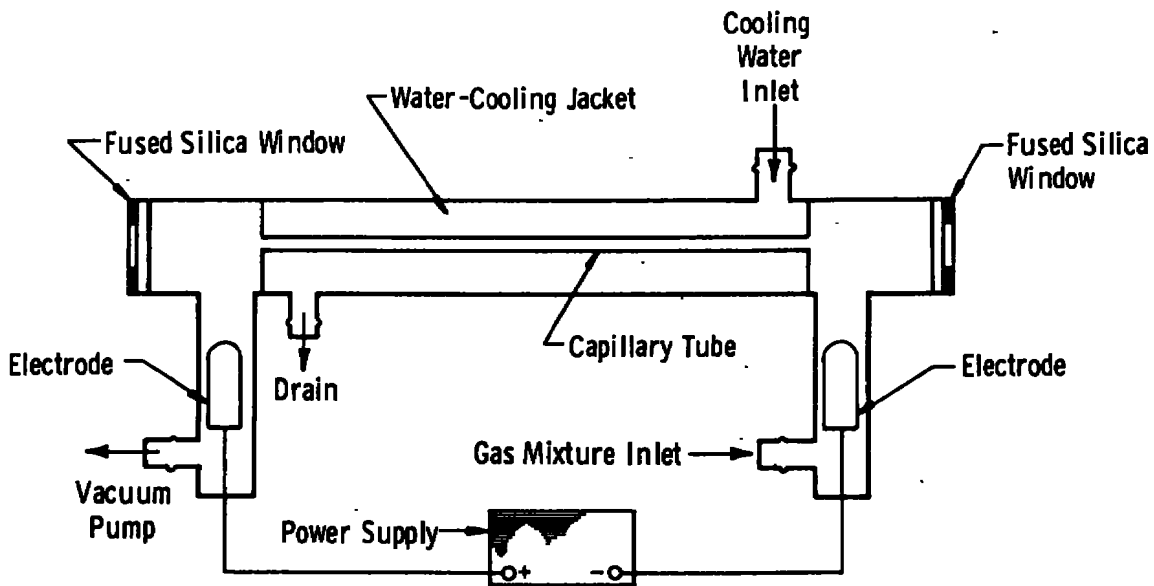

Figure 5. Diagram of resonance lamp used to produce narrow-line radiation.

3.1.4 Optical Apparatus and Traversing Table

The optical, mechanical, and instrumentation equipment used for
the experiment is shown in Fig. 6. The spectrometer field of view is
defined by a fused silica converging lens with a 14-cm focal length
and an adjustable iris set at a diameter of 0.16 cm. The lens and iris
were set so that only parallel light in a 0.16-cm-diam beam was focused
on the spectrometer entrance slit. The lens and iris were mounted on a
fixed optical bench attached to an aluminum support and alignment plate.
The support and alignment plate provided a reference surface and support
mount for the fixed optical benches, spectrometer, and traversing table
support rods. The optical path for the spectrometer field of view was
turned 90 degrees in the horizontal plane by a front surface plane mirror
mounted on a movable traversing table. Similarly, another front surface
mirror on the opposite side of the arcjet turned the optical path another
90 degrees in the horizontal plane, and the parallel beam spectrometer
field of view was focused into the discharge tube used as the light source
for the absorption measurements. The focusing was accomplished by a
14-cm focal length fused silica converging lens mounted on a fixed optical
bench attached to the support and alignment plate. The discharge tube
was similarly attached to the support and alignment plate. Optical
scanning of the arcjet plume was thus accomplished by moving the tra-
versing table and mirrors in the horizontal plane.

The traversing table rode on Thompson linear bearings on two
1.9-cm case-hardened steel rods attached to the mounting plate. The
drive mechanism was a 9.4 turn/cm threaded screw and a universal joint.
The drive motor, also attached to the mounting plate, was a 10-rpm
reversible synchronous motor geared to 50 rpm. The traversing table
could be moved at a rate of 5.3 cm/min in a plane perpendicular to the
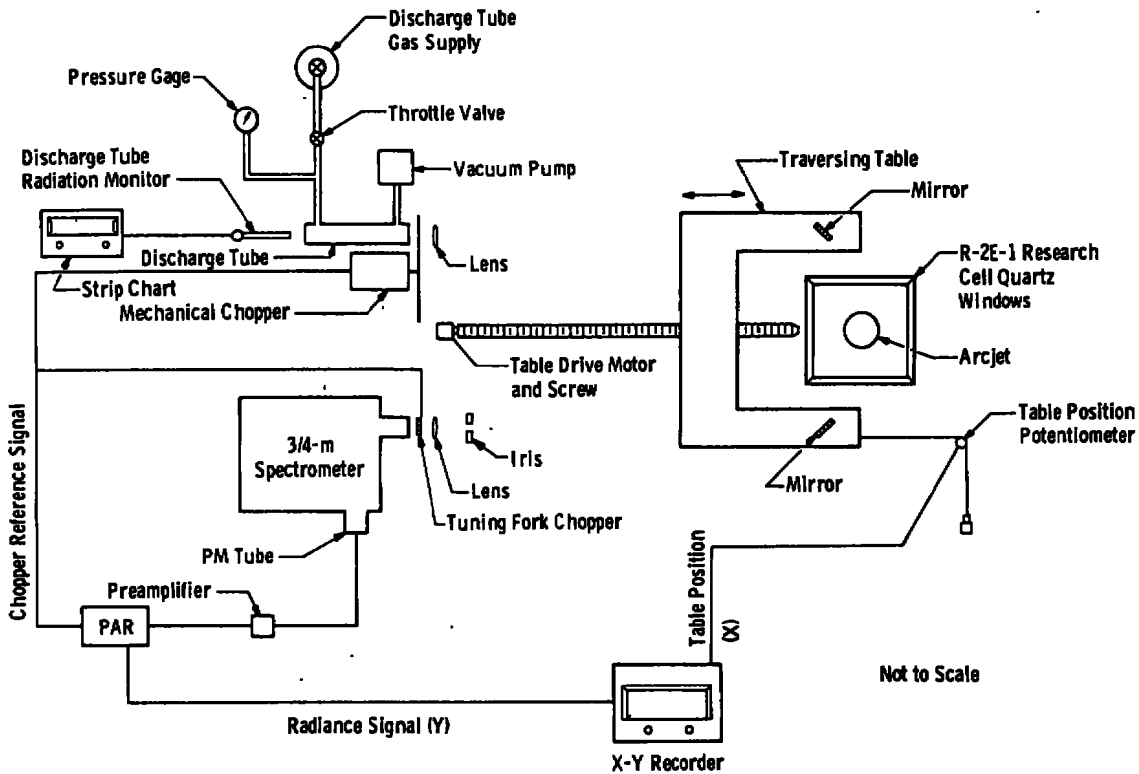plume axis.

Figure 6. Optical, mechanical, and instrument components schematic.

The relative position of the table was indicated by the voltage drop across the terminals of a 10-turn, 20,000-Ω potentiometer. The shaft of the potentiometer was turned by a nylon chain attached to the table. This position-dependent voltage was used to drive the X-axis of an X-Y recorder. The absorption and radiance data were the input to the Y-axis of the X-Y recorder.

A mechanical chopper, operating at 150 Hz, was used at the discharge tube to provide for distinguishing the discharge tube light from that of the arcjet. The reference signal from the chopper and the preamplified photomultiplier tube output signal were input to a PAR® synchronous amplifier for discrimination and amplification of the discharge tube light signal. Similarly, a 150-Hz tuning fork chopper was used at the spectrometer entrance slit in order to use the same electronics system for amplification of the arcjet radiance data. The two choppers were not used concurrently.

3.2 PROCEDURE

After all instrumentation and other equipment had been turned on
and stabilized, absorption reference data were obtained before the arcjet
was ignited. This was accomplished by spatially scanning across the
expected extent of the arcjet plume with the discharge tube light source;
the spectrometer peaked at each of the wavelengths corresponding to
selected spectral lines for which absorption data were to be obtained.
In this manner, the response of the entire optical system as a function
of position was obtained using the Amperex 150 CVP photomultiplier.
Then, with the arcjet operating, stabilized, and positioned with the field
of view two nozzle diameters downstream of the nozzle exit (X/D = 2), an
absorption traverse was made for each of the spectral lines being used.
After the absorption measurements at this arcjet position were completed,
the arcjet was moved so that the field of view was located four nozzle
diameters downstream of the nozzle exit (X/D = 4), and absorption traverses
were made for each spectral line at this axial position.

Subsequent to completing the absorption traverses at X/D = 4, the
photomultiplier tubes were interchanged and emission traverses were made
with the spectrometer peaked in turn on each of the lines used in
emission. After completing the emission traverses at X/D = 4, the jet
was moved back to X/D = 2, and the emission traverses were repeated at
this position.

The optical system was calibrated for determining the absolute
radiance of the emission data in situ by using a tertiary standard
tungsten strip filament lamp. The lamp was placed inside the R-2E-1
research cell with the filament in the field of view. The filament
dimensions are larger than the beam defining the field of view, so
that an implicit assumption with this approach is that the emissivity
of the lamp filament is constant over the extent of the filament. A

slow spectral scan of the calibration lamp emission over the wave-
length range used in the emission traverses, with all optical com-
ponents in place, provided the means of relating the measurement of
of arcjet emission to an absolute radiance measurement at each wavelength
of interest. The equivalent slit width, which was necessary to complete
the determination of the absolute radiance, was obtained by making a
very slow spectral scan of the 425.9- and 426.6-nm spectral lines of
argon, using the discharge tube as the light source.

3.3 UNCERTAINTIES

The various monitoring instruments described in Section 3.1 were
used to set repeatable experimental conditions, and the variables play
no other role in establishing the population densities of excited states.
Therefore, the values reported herein for chamber pressure, mass flow,
cell pressure, voltage, amperage, and electrode gap are to be taken as
typical values. No effort has been made to provide uncertainty estimates
for these parameters.

Estimates of uncertainty were made, however, on the data used to
obtain spectral radiance and absorptances. For the radiance uncertainty,
calibration of the equipment and optical systems was performed in situ
using a tertiary standard calibration lamp having a specified uncertainty
of ±5 percent. The data are reported with uncertainties obtained from
the calibration and the observed propagated experimental uncertainties
through the data analysis procedures. The uncertainty in the absorp-
tance measurement can be obtained from observations in the slight drift
of the intensities of the spectral lines from the discharge tube source
and for the observed electrical noise on the recorder. However, since a
propagation of errors analysis has not been accomplished for the analysis
scheme used to reduce these data, the uncertainties are not reported on
the data. The observed experimental uncertainty was observed to be
typically ±5 percent of the maximum transmission signal.

4.0 RESULTS

4.1 EXPERIMENTAL CONDITIONS

4.1.1 Arcjet Operating Conditions

The argon arcjet in Research Cell R-2E-1 was operated continously at stable conditions for the measurements reported below. Typical experimental conditions are listed in Table 4, and a schematic of the arcjet plume with measurement positions is shown in Fig. 7.

Table 4. Arcjet Operating Conditions

Cell Pressure	0.3 torr
Electrode Gap	0.46 cm
Chamber Pressure	86.2 torr
Voltage	20 v
Amperage	150 amp
Mass Flow	0.167 g/sec
Discharge Tube Pressure	29.8 torr
Discharge Tube Temperature	297°K
Discharge Tube Voltage	3,000 v

During operation the arcjet plume was approximately 8.5 cm in diameter at its widest point and symmetric in appearance. The size and shape of the plume were very stable visually, with no apparent variations during a run period. As is typical with the operation of d-c arcjets of this type, there was a white central core, interpreted as a diffuse arc, protruding from the nozzle exit. This central core was of short spatial extent, protruding less than one nozzle diameter downstream of the nozzle.
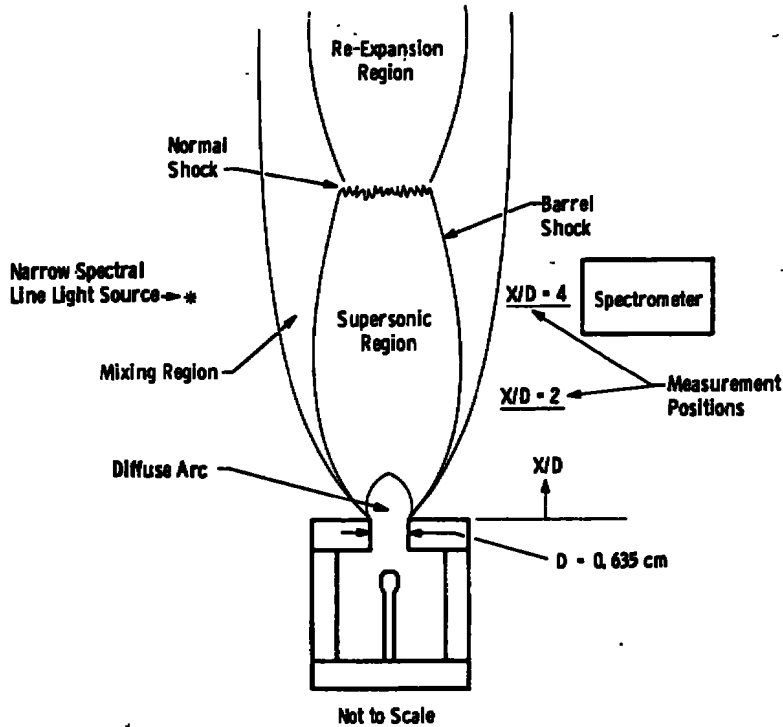
Figure 7. Arcjet plume schematic showing measurement positions.

4.1.2 Spectral Measurements

Spectral line absorption and emission measurements were made for several transitions originating from different electronic quantum states in argon. Each absorption line chosen had as its lower state one of the first four excited states. Each emission line chosen had as its upper state a relatively high quantum state which was believed to exhibit equilibrium with the free electron density. A partial energy level diagram for argon is given in Fig. 8, showing schematically the energy states and the corresponding transitions used in this study. As can be seen, the absorption data become redundant in the determination of the density of the second, third, and fourth excited states. This redundancy is important to show self consistency of the results since

these four excited states are not expected to fit any specific equilibrium distribution relationship. The emission lines originate from several different excited states. Redundancy of emission data is not necessary since the densities of these excited states are expected to satisfy the law of mass action and correspond to an equilibrium distribution. A Boltzmann plot of these densities should thus be linear, and the data will be amenable to least squaring techniques. The spectral lines used, the type of measurement, and the energy level which gives rise to the spectral lines are listed in Table 5.
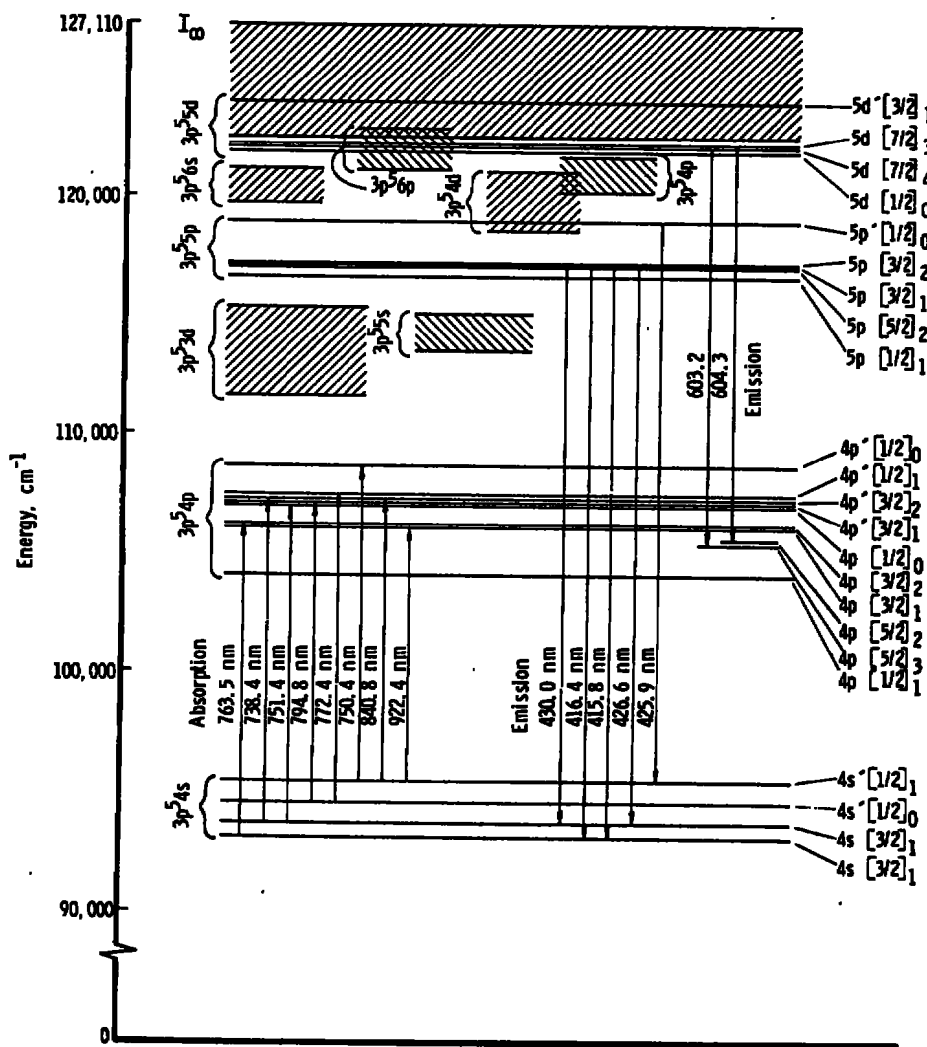
Figure 8. Partial argon energy level diagram.

Table 5. Argon Spectral Lines used in Experiment

Wavelength, nm	Energy Level	Type Measurement
763.5	$4s[3/2]_2$	Absorption
738.4	$4s[3/2]_1$	
751.4		
772.4	$4s'[1/2]_0$	
794.8		
750.3		
840.8	$4s'[1/2]_0$	
922.4		
430.0	$5p[5/2]_2$	Emission
416.4	$5p[3/2]_1$	
415.8	$5p[3/2]_1$	
426.6		
425.9	$5p'[1/2]_0$	
603.2	$5d[7/2]_4$	
604.3	$5d[7/2]_3$	

4.1.3 Isentropic Plume Calculations

The radial profiles of static temperature at X/D = 2 and 4, which are required for the analysis of the absorption data, were determined analytically by method of characteristics (MOC, Ref. 37) calculations of the plume gas dynamic properties. The MOC calculations require the stagnation conditions at the nozzle exit as initial conditions. The stagnation conditions at the exit of the arcjet nozzle were determined by the Rayleigh Heating Analysis approach reported by Bryson (Ref. 20) and are listed in Table 6.

Table 6. Arcjet Nozzle Exit Stagnation Conditions for Isentropic Plume Calculations

Total Temperature . . . . 4462°K

Total Pressure . . . . 50 torr

The MOC calculations used a straight sonic starting line at the nozzle exit plane. No boundary-layer corrections were made, since estimates of the boundary-layer buildup suggest that the thickness at the nozzle exit is virtually negligible (personal communication, R. J. Bryson, ARO, Inc.).

The calculated isentropic static temperature profiles are shown in Fig. 9 for axial stations X/D = 2 and 4. The barrel shock and free boundary location from the calculation are also shown in Fig. 9.
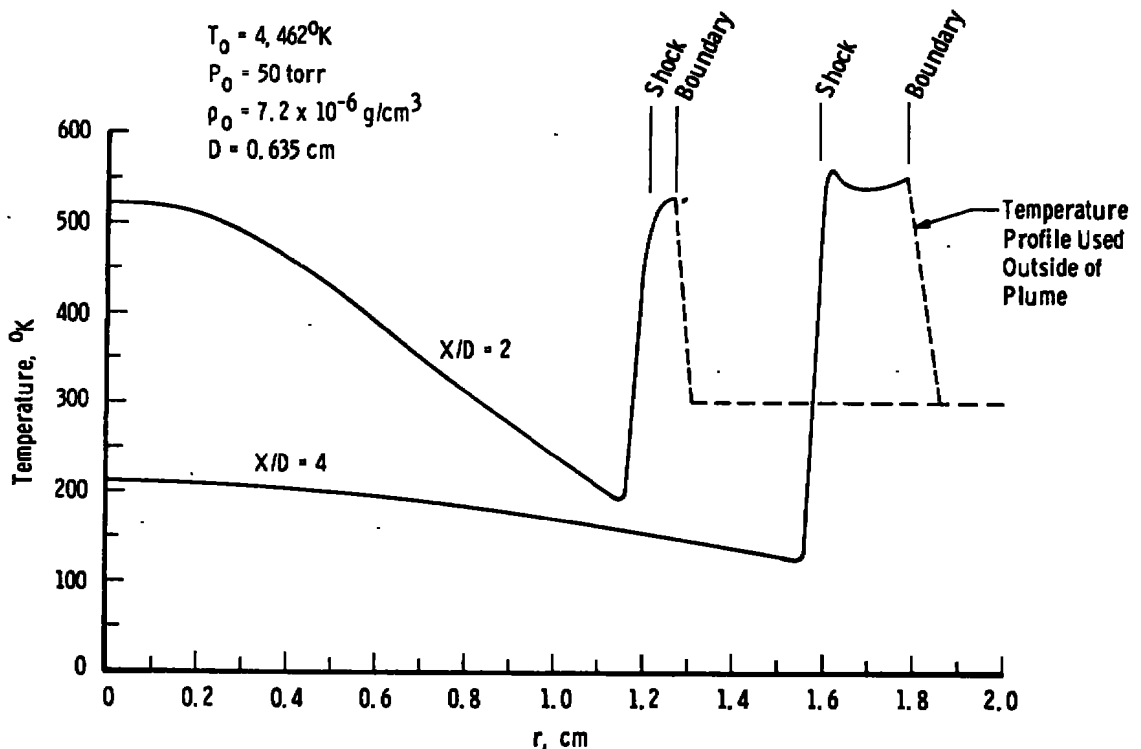
Figure 9. Radial static temperature profiles for argon arcjet plume from method of characteristics solution.

The indicated shock and boundary locations must be considered approximate since the MOC calculation did not include an accounting of the mixing with ambient gases at the jet boundary, and the characteristic network used was quite coarse at the outer edge of the jet. However, the shock location is useful primarily for qualitative comparisons, so no effort was made to obtain accurate estimates. The static temperature profile beyond the indicated jet boundary required in the absorption inversions was set to 300°K.

4.2 EXPERIMENTAL RESULTS

4.2.1 Radiance Data

The results of the spectral emission profile measurements are presented in Appendix B, Figs B-1 through B-14. Figures B1 through B7 show the results of measurements at $X/D = 2$, and Figs. B-8 through B-14 show the results of measurements at $X/D = 4$. These data are presented in absolute units of radiance $(w/cm^2\text{-}sr)$ for the ordinate and displacement from the centerline (cm) for the abcissa. The symbols shown represent actual (calibrated) data points as recorded on the X-Y recorder, and the smooth line represents the results of determining the series of polynomials best fitting the data in the least squares sense according to a numerical least squares spline fit technique. Typical error bars for the raw data are included in the plot and represent a 2 σ uncertainty bound in the experimental data. The Abel inversion used to reduce these radiance data to emission coefficients requires the assumption that the radiating source is cylindrically symmetric. Thus the data presented in Figs. B-1 through B-14 is from both sides of the observed plume centerline. As can be seen, the experimental symmetry is indeed good, with the major asymmetries observed occurring near the outer periphery of the plume.

4.2.2 Absorption Data

The results of the spectral absorption profile measurements are presented in Figs. B-15 through B-30. Figures B-15 through B-22 show the results of measurements at X/D = 2, and Figs. B-23 through B-30 show the results of measurements at X/D = 4. The results are presented as transmittance on the ordinate versus displacement from the observed plume centerline (cm) on the abcissa. As with the emission measurements, data taken from both sides of the plume centerline are shown by the symbols so that the degree of symmetry in the plume may be judged. As can be seen here, the plume does appear to be satisfactorily symmetric.

The plume at each axial position was chosen to have a radius of 3 and 3.64 cm at X/D = 2 and 4, respectively, as indicated on each of plots B-15 through B-30. It is to be noted that these radii are different from the apparent plume radii indicated from the emission data, Fig. B-1 through B-14. Indeed, the plume radius one would observe from emission data is notably smaller than the plume radius observed from the absorption data. This is readily explained by studying the energy levels from which the data being observed arise. Referring to Fig. 8, one can see that each of the spectral lines used in the emission measurements has, as its initial state, one of the highly excited states, all of which have many collisional-radiative transitions which will contribute to a decrease in the density of that state. By contrast, the initial states of the absorption data are each one of the first four excited states, two of which are metastable and two of which have resonance transitions to the ground state.

At the ambient conditions of the test cell, the absorption coefficient for resonance transitions is of order 10^6 cm^{-1}, so that the gas can be assumed to be optically thick to resonance radiation. Thus the only low-lying physical mechanisms contributing to a decrease in the densities of these excited states are collisions of the second kind

43

between the heavy body specie, electron-atom collisions resulting in a decay of the atom to the ground state, and collisions between the excited specie and the experiment enclosure. None of these de-excitation mechanisms is a dominant feature for the four lowest excited states in the arcjet plume. Hence, in a loose manner of speaking, one can say that atoms in highly excited states will decay quite rapidly, whereas once an atom decays to one of the first four excited states it stays there for a relatively long time. Thus the research cell environment, which fills with the effluent gases from the arcjet, would be expected to show a relatively high density of atoms in the first four excited states and a low density of atoms in the highly excited states. Because of entrainment and mixing of the test cell gases into the outer periphery of the plume, one would expect the plume to have an apparently larger size in absorption than in emission. The existence of the metastable atoms in the arcjet plume has been noted and used previously in other experimental investigations (Ref. 8). Further, the presence of metastable atoms outside the plume has been noticed previously (personal communication, J. D. Few, ARO, Inc.). However, the present work appears to be the first evidence published of the metastable, enriched environment of the research cell.

Thus, finally, although the arbitrarily assigned value for the plume radius at each axial position is large for the emission data, and perhaps small for the absorption data, it has little real effect. This is true because, in emission, the result of the number density determination beyond the assigned plume radius includes the contribution of the test cell environment, which can be included in the outer zone definition and effectively removed from the considerations.

4.3 ANALYSIS OF EXPERIMENTAL DATA

4.3.1 Emission Coefficients

The results of performing the Abel inversion on the emission data are shown in Appendix B, Figs. B-31 through B-44. Figures B-31 through

B-37 show the results at X/D = 2, and Figs. B-38 through B-44 show the results at X/D = 4. The ordinate in these plots is the emission coefficient, or the power radiated per unit volume of the plasma at the wavelength of the spectral line, and the abscissa is radial position in the plume. The uncertainties bars on the plot are the results of propagating the experimental data uncertainties through the numerical analytic technique required to effect the data smoothing and subsequent Abel inversion. In effect, the bars on the plots are the square roots of the principal diagonal elements of the variance-covariance matrix of the emission coefficients as determined from the diagonal variance-covariance matrix for the raw data, plotted in Figs. B-1 through B-14. The error bars in Figs. B-31 through B-44 thus represent a 2σ uncertainty bound on the emission coefficients. The necessary description of the equations to perform the series of linear transformations on the data variance-convariance matrix to transform it to the emission coefficient data matrix is presented in Ref. 40. It is encouraging to note that, for a 2σ raw data uncertainty of typically 5 percent, one finds a typical 2σ emission coefficient uncertainty of 10 percent.

In order to assess the self consistency of the spectral emission profiles and thus confirm that the plasma had the same geometrical shape regardless of the upper energy level for the spectral lines and that the data reduction procedures did not degrade the data quality, it is informative to examine the integrand of the emission coefficient. From the Abel inversion, the emission coefficient is

$$\epsilon(r) = -\frac{1}{\pi} \int_{r}^{R_o} \frac{(dI/dZ)\, dZ}{\left(Z^2 - r^2\right)^{1/2}} \tag{9}$$

where dI/dZ is the local slope of the radiance and R_o is the outer radius of the plume. Examining the integrand,

$$\frac{dI/dZ}{\left(Z^2 - r^2\right)^{1/2}}$$

which is dependent only upon geometry and the local data slope, one
would expect that, on a normalized basis and for a given value of r,
this profile should assume the same quantitative shape for each spectral
line. The integrands for each spectral line are shown in Figs. 10 and
11 for r = 0 at axial positions of X/D = 2 and 4, respectively. In
these figures, the ordinate is the integrand at each position of X
normalized by the maximum value at that wavelength. As can be seen, the
profiles are quite similar, the variations among the profiles being
within typical expected experimental uncertainies. The region of largest
deviation among the various profiles is near the outer edge of the
plume, where the data quality suffers because of a low signal to noise
ratio. The plots shown are for the emission coefficient on the centerline.
As additional comment, note that the position of maximum integrand was
the same at each wavelength, suggesting further the similarity of the
radial profiles at each wavelength.

$$\varepsilon = -\frac{1}{\pi} \int_r^{R_0} \frac{(dI/dZ)\, dZ}{(Z^2 - r^2)^{1/2}}$$
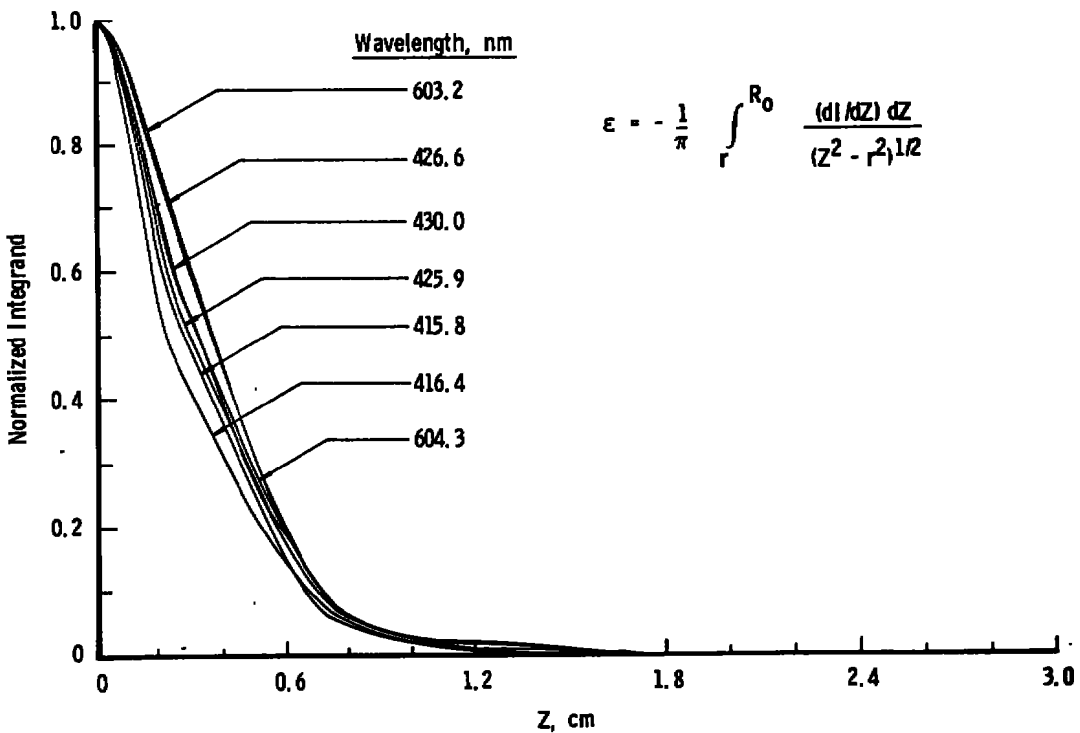
Figure 10. Normalized emission coefficient integrands for centerline at X/D = 2.

$$\epsilon = -\frac{1}{\pi} \int_{r}^{R_0} \frac{(dI/dZ)\,dZ}{(Z^2 - r^2)^{1/2}}$$
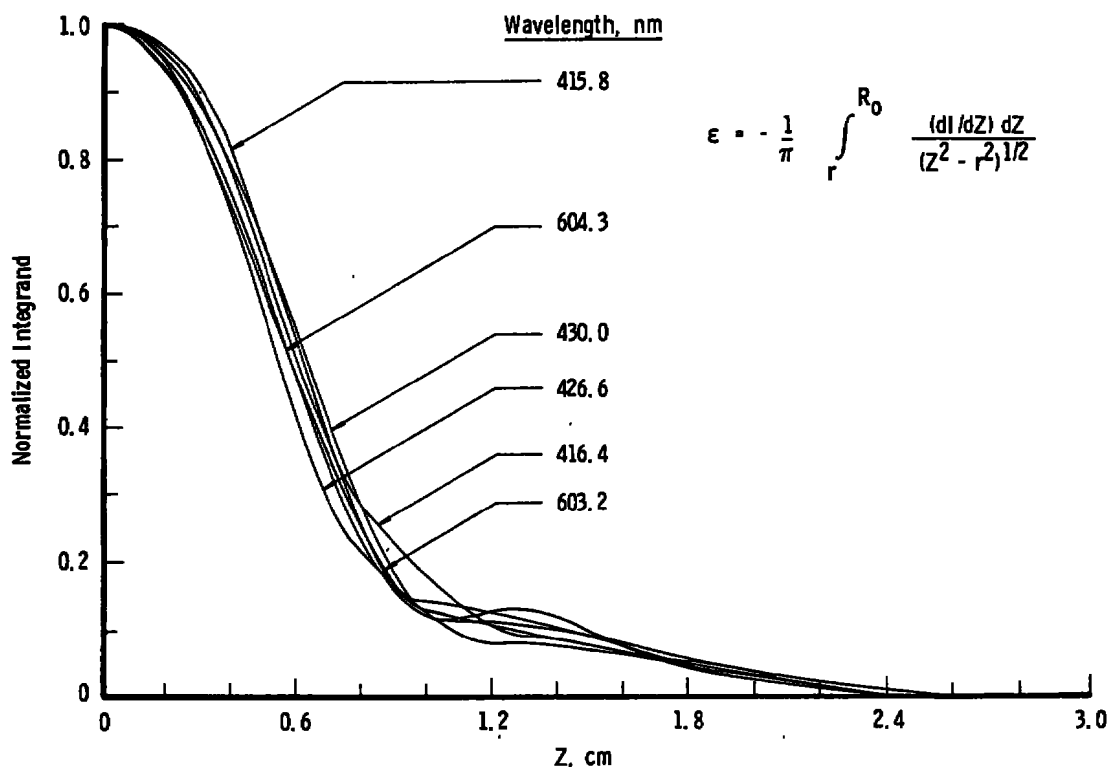
Figure 11. Normalized emission coefficient integrands for centerline at X/D = 4.

An additional geometrical interpretation may be provided by noting that the emission coefficient at each wavelength is directly proportional to the area under the normalized curves. In the ideal case, the profiles should be colinear, and thus the areas should be equal. Although this is not the case in the real sense, the variations in the areas under the curves are relatively small and provide additional favorable evidence of the quality of the experimental data and the data reduction procedure.

4.3.2 Number Density Profiles from Absorption Data

The absorption data were radially inverted according to the scheme described in Appendix A to yield the radial profiles of number density of the excited specie. A required parameter in the inversion process is the static temperature of the absorbing specie which enters through the Doppler line shape. These temperatures were not available from the

experimental data; rather, they were obtained from the method of charac-
teristics expansion for a free jet into vacuum (Ref. 37). The static
temperature profiles used for the determinations were shown in Fig. 9.
It is interesting to note, in light of the discussion of the difference
in apparent plume size in Section 4.2, that the plume boundary computed
from the MOC calculation is not inconsistent with the approximate
apparent plume boundary observed from the emission data.

The number density profiles of the excited states obtained from
the absorption data and static temperature determinations are shown
in Figs. 12 through 19. Figures 12 through 15 show the results at
X/D = 2, and Figs. 16 through 19 show the results at X/D = 4. The
data for each spectral line used is presented, and the plots are for
the $4s\,[3/2]_2$, $4s\,[3/2]_1$, $4s'\,[1/2]_0$, and $4s'\,[1/2]_1$ quantum levels,
successively. Since the 763.5-nm spectral line is quite intense, this
was the only measurement obtained which was related to the first
metastable state, the $4s\,[3/2]_2$ quantum level. The consistency of the
redundant measurements for each of the other quantum levels is in
general quite good at each axial position, with the number density pro-
files for the second excited state, Figs. 13 and 17, showing remarkable
agreement. The number density of the fourth excited state, the $4s'\,[1/2]_1$
quantum level, as determined from the 840.8-nm spectral line, is markedly
below the densities determined from the 750.4- and 922.4-nm spectral
lines. The consistency of the results for the 840.8-nm spectral line at
both axial positions suggests that some unanticipated physical mechanism
or improper fundamental constant (transition probability, for example)
affects the results for this line. Consequently, the density profiles
determined from the 840.8-nm spectral line are not included in subsequent
considerations.

The barrel shock for the free-jet expansion, although not readily
apparent in the experimental transmittance data, is apparent in the
number density radial profile determinations at X/D = 4. Interpretation
of this must be approached cautiously, however, for these determinations

are based upon the method of characteristics plume expansion, and the effect of the computed barrel shock upon the static temperature is responsible for the apparent position of the shock in the radial number density plots. Independent measurements for determinations of the actual static temperature are necessary for final resolution of the true shock location.
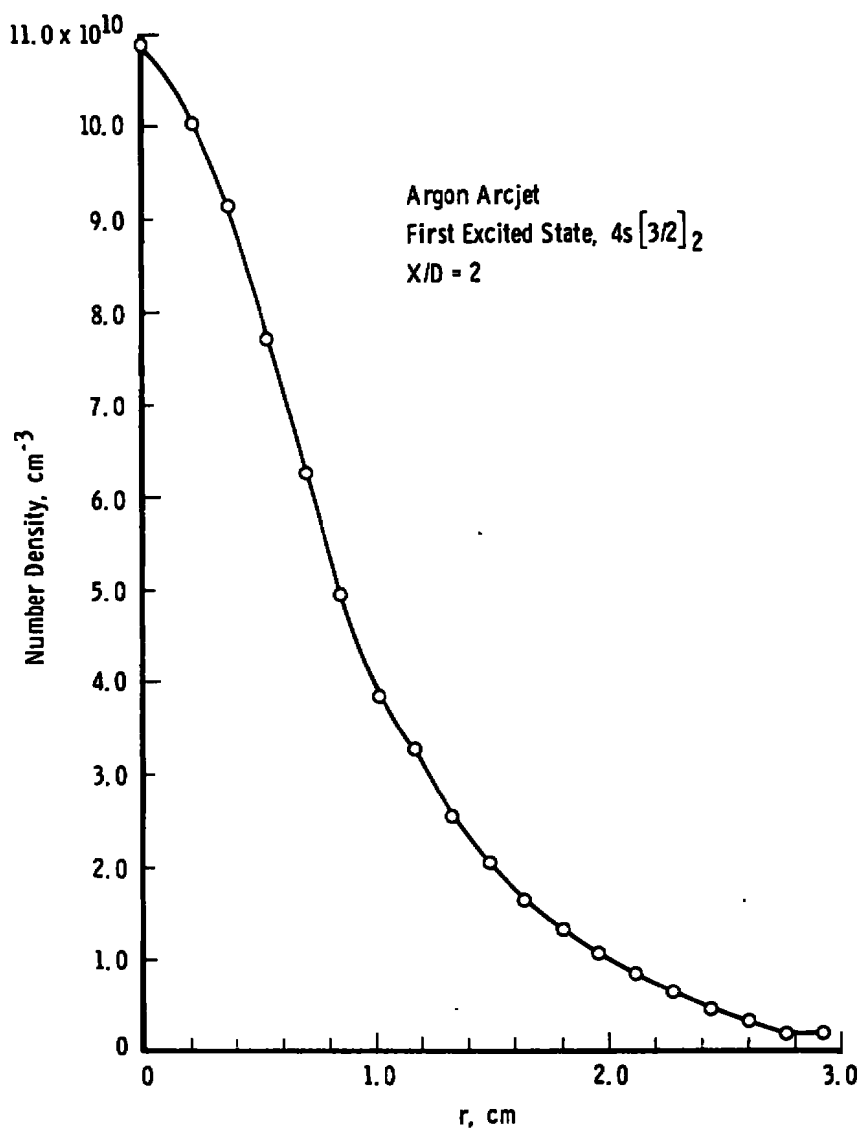
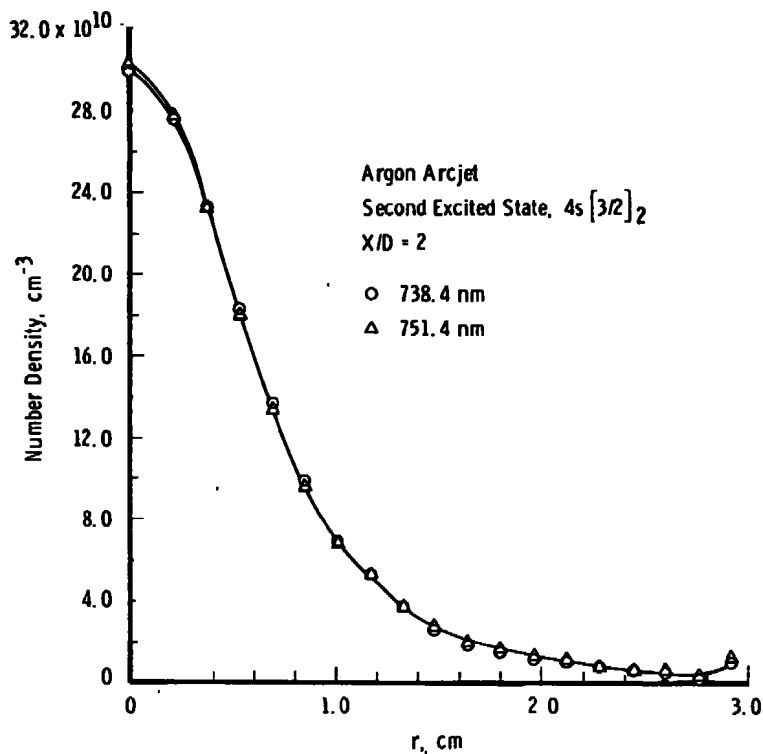Figure 12. Radial number density profile of 4s[3/2]$_2$ quantum state from absorption data, X/D = 2, 763.5-nm spectral line.

Figure 13. Radial number density profiles of 4s[3/2]$_1$ quantum state from absorption data, X/D = 2, 738.4- and 751.4-nm spectral lines.
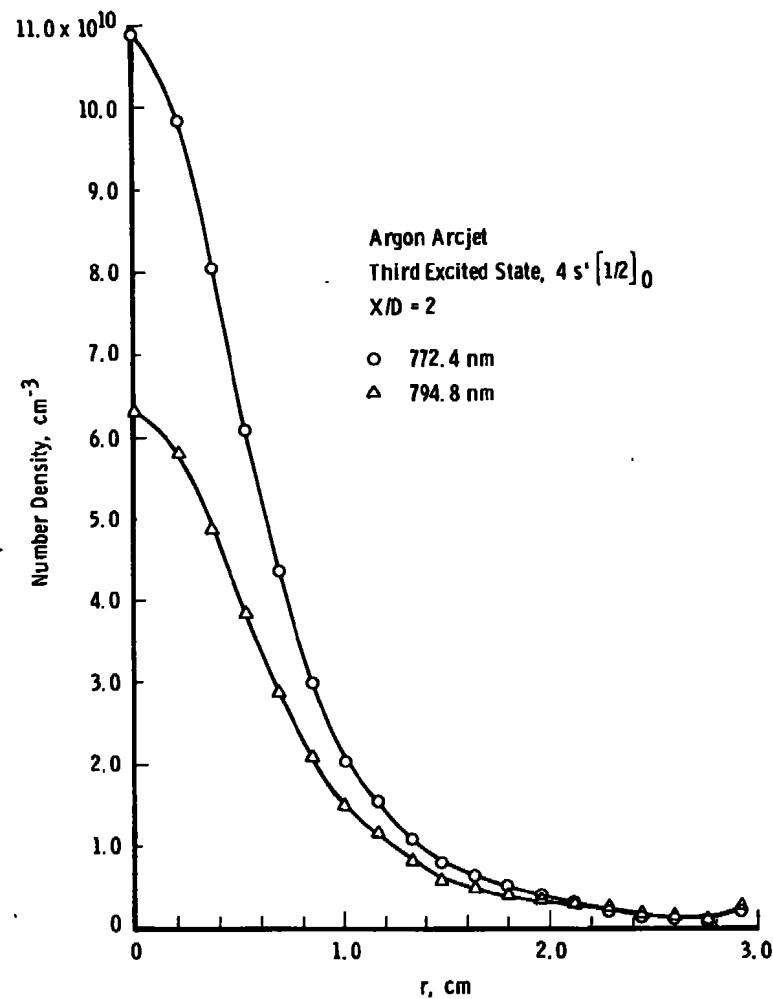
Figure 14. Radial number density profile of 4s'[1/2]$_o$ quantum state from absorption data, X/D = 2, 772.4- and 794.8-nm spectral lines.
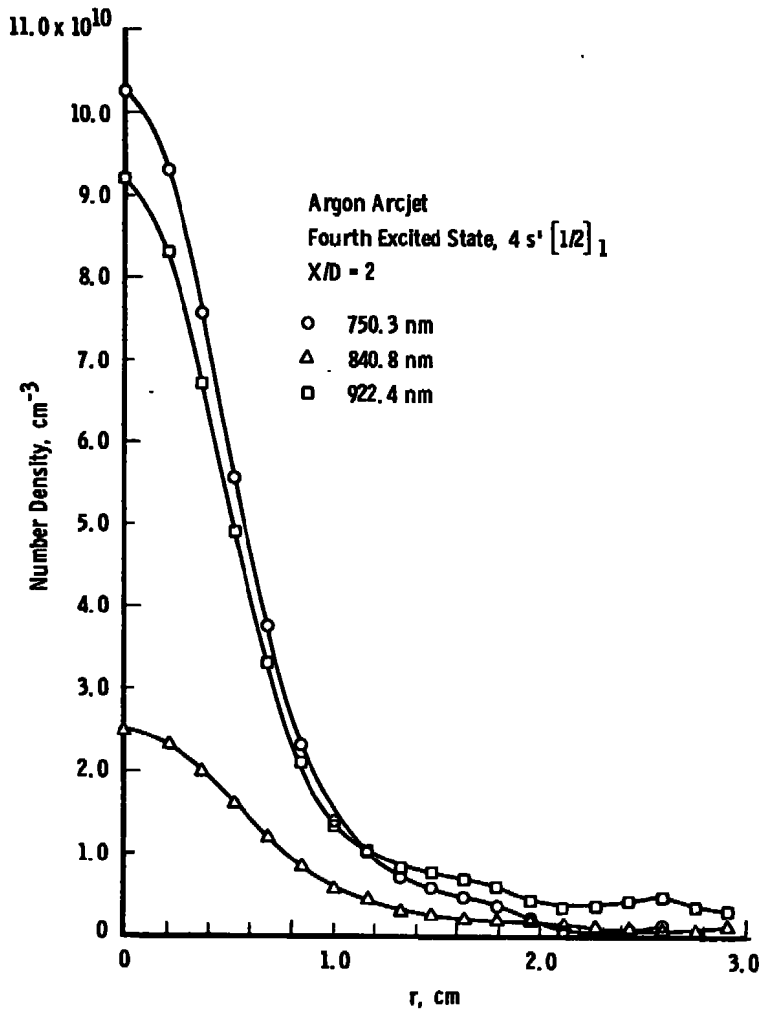
Figure 15. Radial number density profile of 4s'[1/2]₁ quantum state from absorption data, X/D = 2, 750.3-, 840.8-, and 922.4-nm spectral lines.
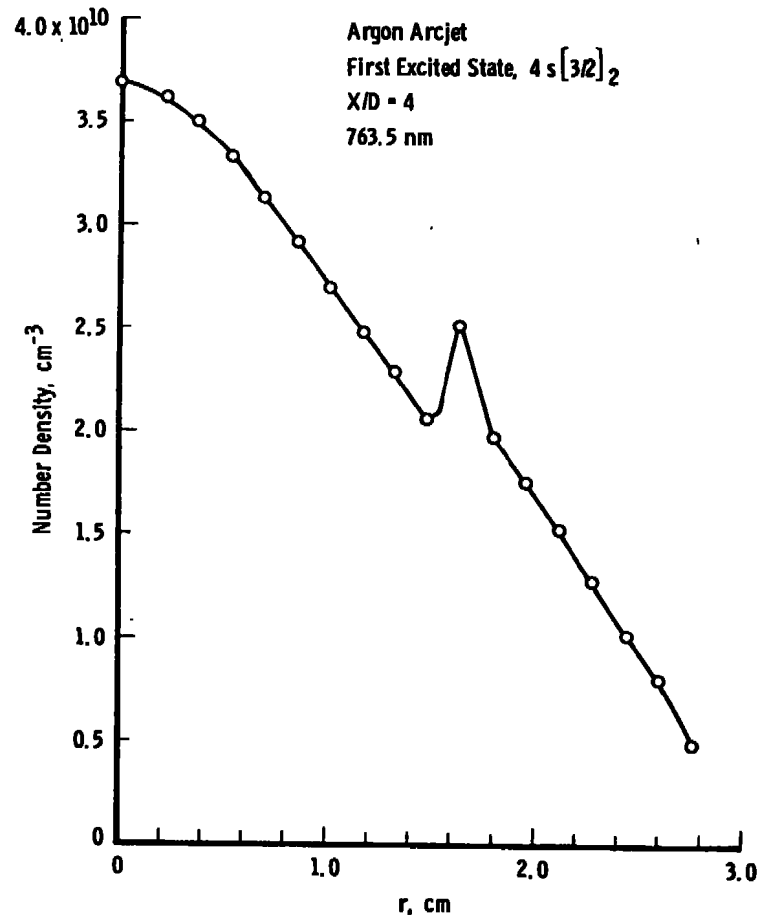
Figure 16. Radial number density profile of 4s[3/2]₂ quantum state from absorption data, X/D = 4, 763.5-nm spectral line.
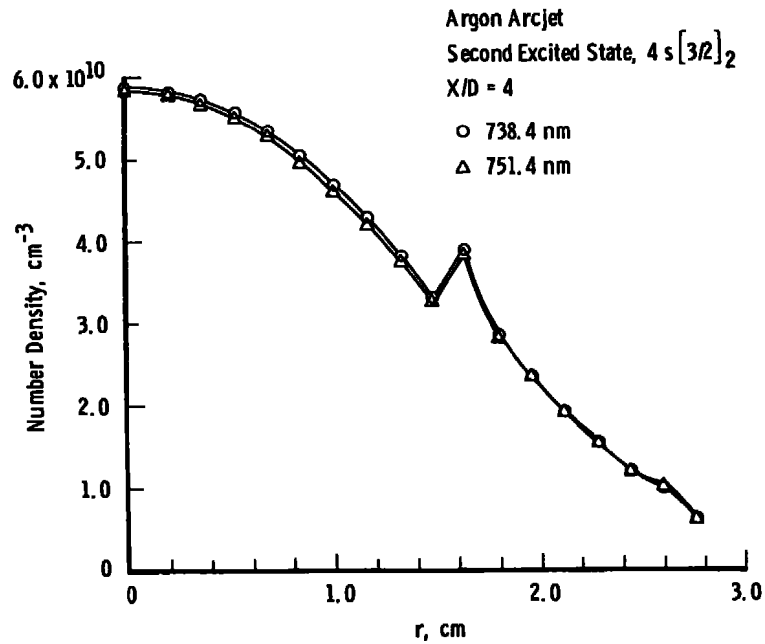
Figure 17. Radial number density profile of 4s[3/2]$_1$ quantum state from absorption data, X/D = 4, 738.4- and 751.4-nm spectral lines.
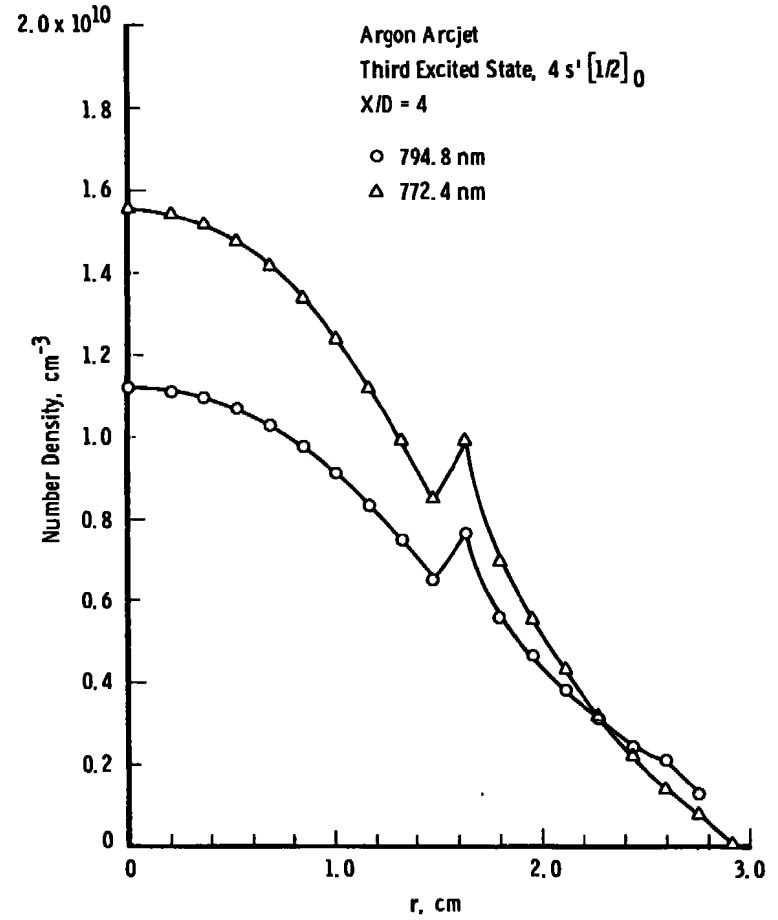
Figure 18. Radial number density profile of 4s'[1/2]$_o$ quantum state from absorption data, X/D = 4, 772.4- and 794.8-nm spectral lines.
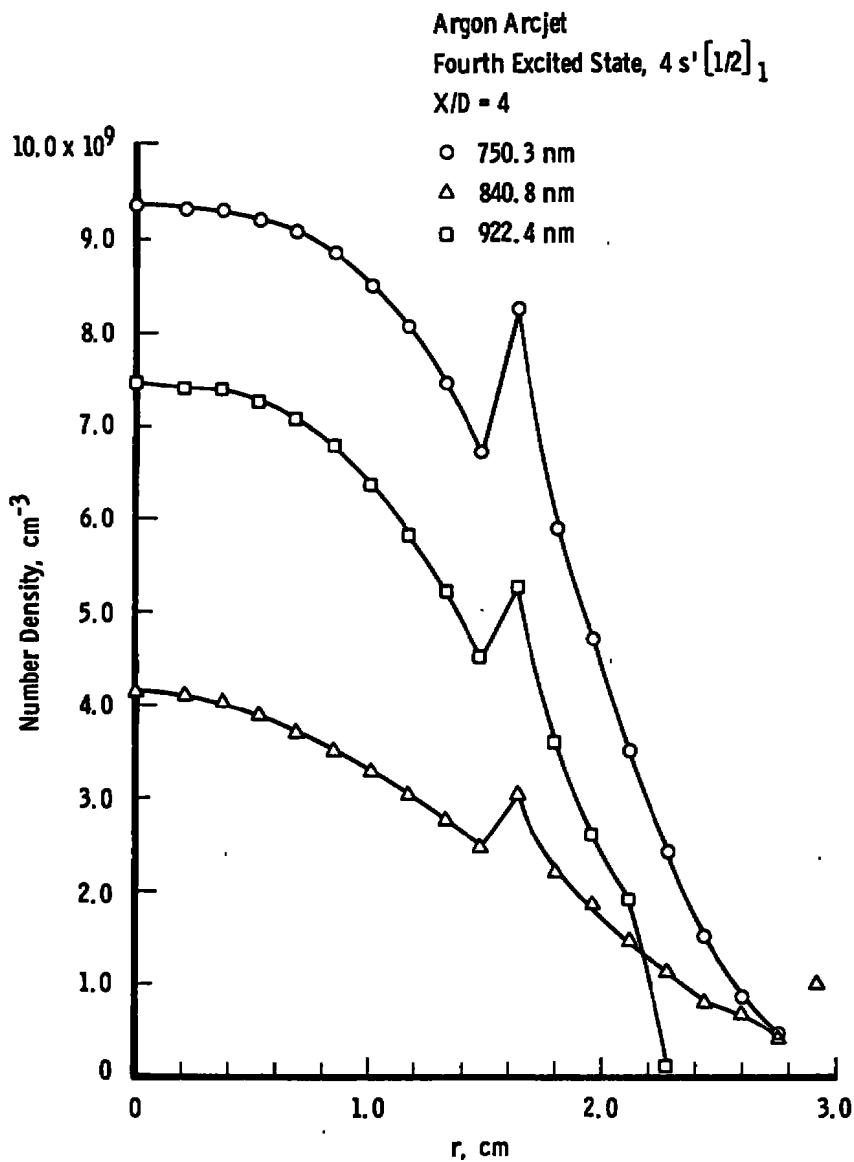
Figure 19. Radial number density profile of $4s'[1/2]_1$ quantum state from absorption data, X/D = 4, 750.3-, 840.8-, and 922.4-nm spectral lines.

4.3.3 Electron Temperature and Density

The emission coefficient is related to the number density of the excited state by the equation

$$\epsilon\,(r) \;=\; \frac{h\nu}{4\pi}\; A\; n(r) \tag{10}$$

where h is Planck's constant, ν is the frequency of the radiation, A is the Einstein spontaneous transition probability, and n is the number density of atoms in the excited state. It is thus seen that the number density profiles are directly proportional to the emission coefficient profiles. If an excited state is in collisional equilibrium with the free electrons, it will satisfy the law of mass action, expressed by the Modified Saha Equation:

$$\frac{n(p)}{n^+ n_e} = \left(\frac{h^2}{2\pi m_e k T_e} \right)^{3/2} \frac{g_p}{g^+ g_e} \exp\left(I_p / k T_e \right) \tag{11}$$

where $n(p)$ is the number density of atoms in the pth excited state, n^+ and n_e are number densities of the singly ionized ions and free electrons, respectively, h and k are Planck's and Boltzmann's constants, respectively, m_e and T_e are the free electron mass and temperature, g is the statistical weight of the appropriate specie, and I_p is the ionization potential of the excited state. In the form of the Modified Saha Equation, it is seen that if the density of some other excited state, q, is also in equilibrium with the same free electron distribution, then one can write

$$\frac{n(p)}{n(q)} = \frac{g_p}{g_q} \exp\left[\left(I_p - I_q \right) / k T_e \right]$$

This is the familiar form of the Boltzmann expression for the density of states in equilibrium. Thus on a Boltzmann plot of the natural logarithm of $n(p)/g_p$ versus energy, the $n(p)$ values will all fall on the same straight line, provided the upper excited states are all in equilibrium with the free electron density. These results for the plasma centerline are shown in Figs. 20 and 21 for the measurements at X/D = 2 and 4, respectively. The ordinate of each plot is the natural logarithm of $n(p)/g_p$, and the abscissa is the excitation energy of the upper state p. The symbols represent the results obtained for each of the spectral lines used in these determinations, and the straight line represents the best least squares fit to the data in the semilog plane. As can be seen, these data at each axial position do fit a

least squares straight line quite adequately, as is required if the excited state is in equilibrium with the free electron density. The centerline electron temperature and number density determined from these data are listed in Table 7. Included is the 2σ uncertainty bound determined from the propagated 2σ experimental bound.
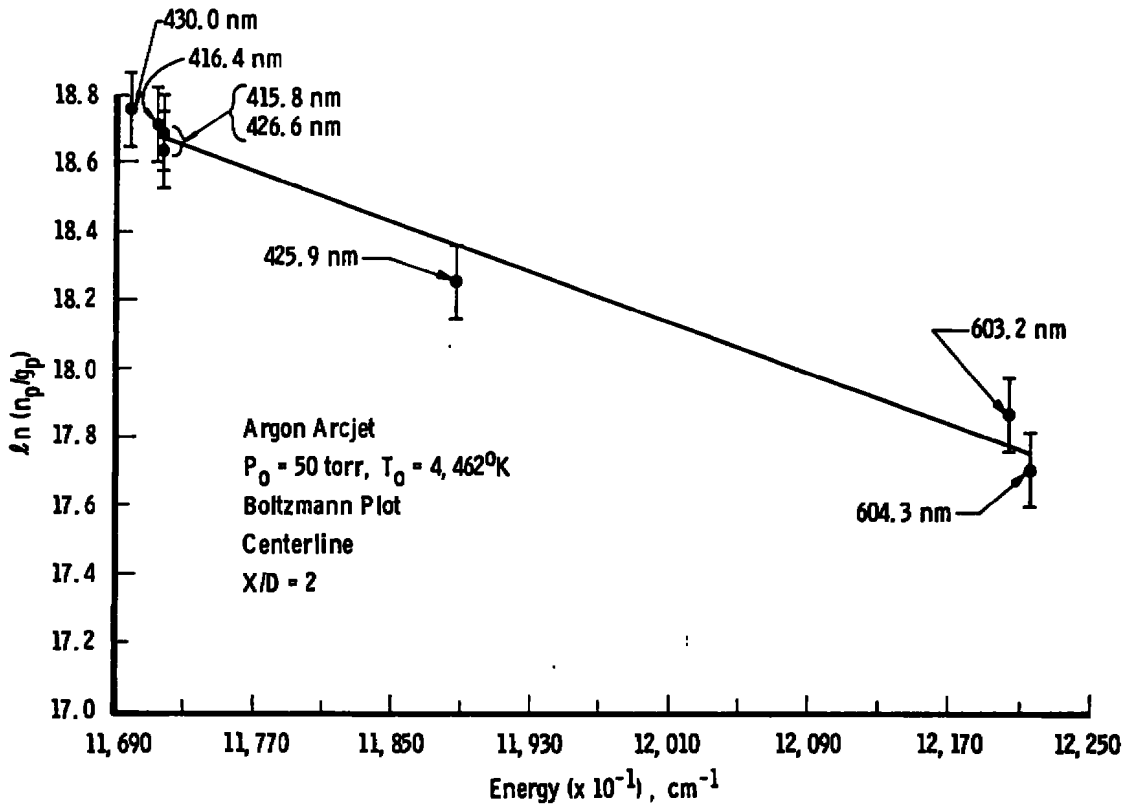

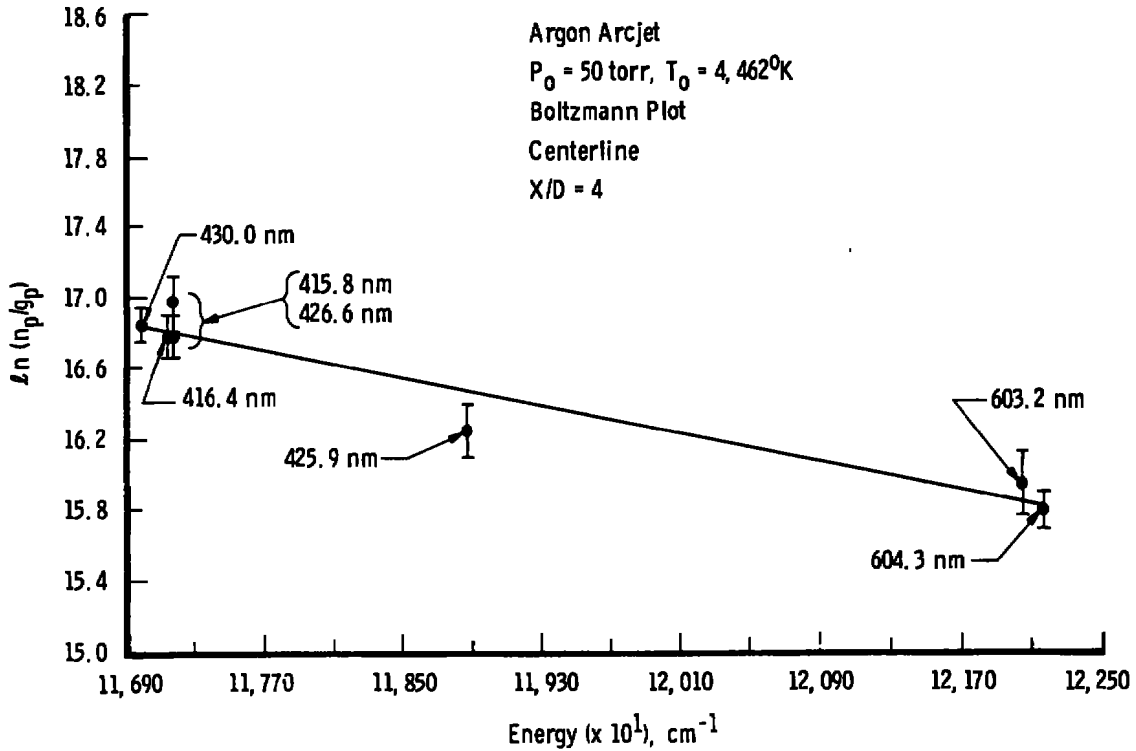Figure 20. Boltzmann plot on argon arcjet centerline, X/D = 2.

Figure 21. Boltzmann plot on argon arcjet centerline, X/D = 4.

Table 7. Centerline Electron Temperature and Number Density at
X/D = 2 and 4

	$T_e, {}^\circ K$	n_e, cm^{-3}
X/D = 2	7,760 ± 763	$(6.34 \pm 0.45) \times 10^{14}$
X/D = 4	7,200 ± 843	$(2.19 \pm 0.32) \times 10^{14}$

The electron temperature and density radial profiles were also
determined from the radially dependent emission coefficients by per-
forming analysis similar to that described above. The resultant profiles
are shown in Figs. 22 and 23. Figure 22 shows the electron temperature
versus radius, and Fig. 23 shows the electron density versus radius.
The electron density profiles are about as expected, showing a general
gradual falloff from the centerline value with some structure apparent
at a radial position of 0.9 cm for the data from X/D = 2 and a definite

increase at a radial position of about 1.1 cm for the data at X/D = 4
The electron temperature profile was somewhat of a surprise, however.
There is a marked tendency for the electron cloud to be cooler on the
centerline of the jet than on the outer periphery. The increase in
temperature at the far periphery of the plume (for r > 1.3 cm, for
instance) is not to be taken seriously, as the radiance data from this
portion of the plume are extremely weak. The nature of the electron
temperature and density profiles at r = 0.9 cm for X/D = 2 and r = 1.2
cm for X/D = 4 makes it especially tempting to ascribe the structure to
the physical presence of the barrel shock. This could provide a source
for electron heating, and upstream diffusion of these more energetic
electrons could be responsibile for the shape of the electron temperature
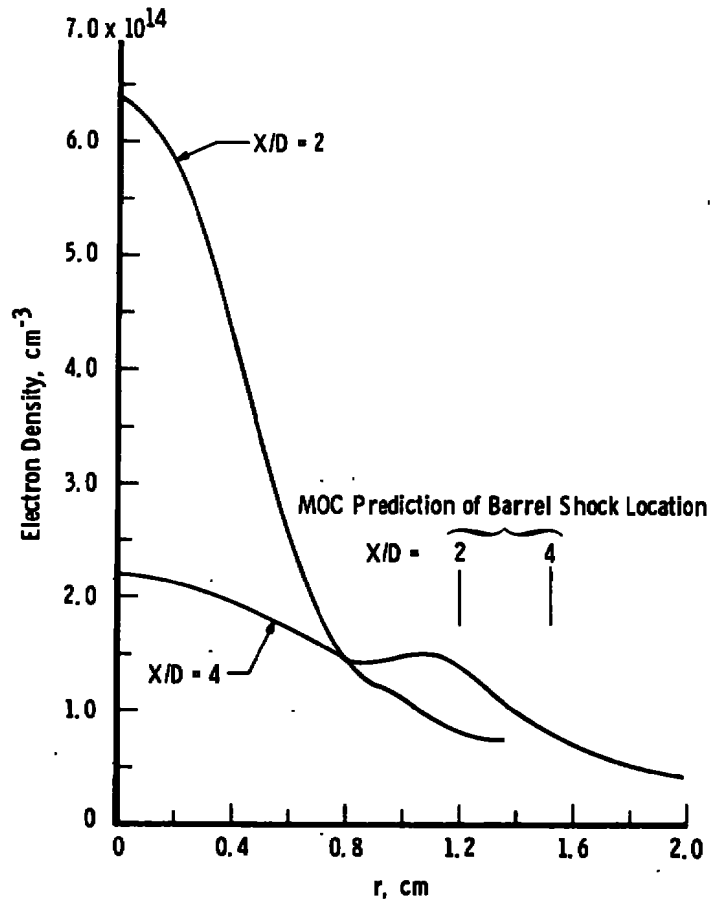
Figure 22. Radial electron number density profile.
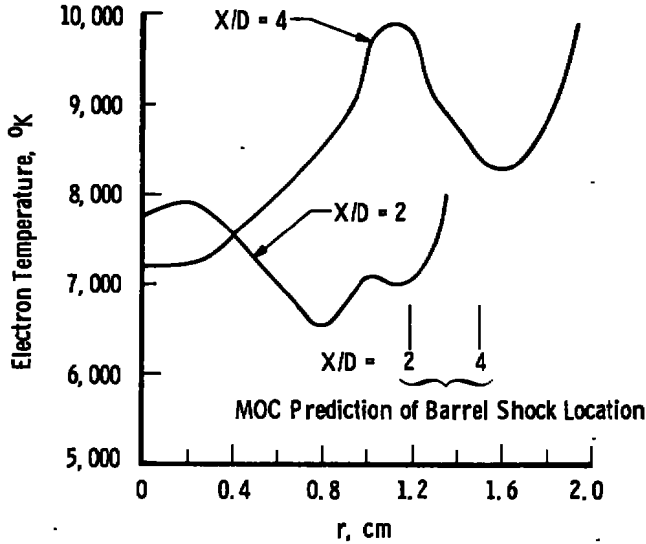
Figure 23. Radial electron temperature profile.

profile. Further investigation will be required to establish the validity of the conjecture.

Plotted on each of the figures are shock location predictions from the method of characteristics solution for this plume expansion. It is significant to note that the location of the barrel shock derived from MOC calculations is only slightly larger than the location shown in the data, typically one half of a nozzle diameter.

4.3.4 Comparison of Observed Number Densities with Equilibrium Configurations

As discussed earlier, those excited state densities which are in equilibrium with the free electron density will all fall on the same straight line on a Boltzmann plot. As was shown in connection with the centerline data, the number densities of the upper excited states do fit, in the least squares sense, such a straight line, and thus do establish an equilibrium configuration. It is informative to compare, in the same manner, the number densities of the first four excited states, obtained from the absorption data, to the equilibrium condition determined by the upper excited state. This comparison is shown

in Fig. 24. The ordinate in this case is the common logarithm of the ratio $n(p)/g_p$ rather than the natural logarithm. The two are related by a constant, however, so that the accuracy of comparisons is not impaired. The results at both X/D = 2 and X/D = 4 are shown. The
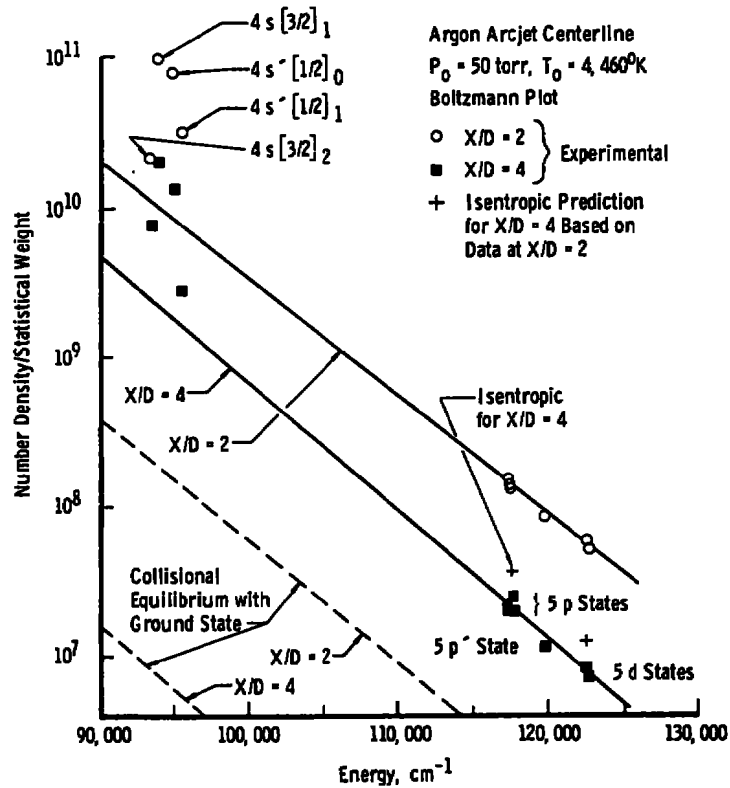
Figure 24. Boltzmann plot of experimentally determined centerline population densities.

straight line at each axial position reflects the results of the least squares straight line that defines the condition for equilibrium with the free electron density and thus shows that the four lowest excited states are demonstrably nonequilibrium and lie markedly above the equilibrium value. To further illustrate the nonequilibrium characteristics of the entire excited state distribution, the dashed lines in Fig. 24 illustrate the distribution function that excited state densities would follow if they were in collisional equilibrium with the ground state density determined from the MOC at the observed electron temperature. It

is notable that at X/D = 2 this condition is below the observed excited
state distribution function by a factor of approximately 75, and, for
X/D = 4, by a factor of approximately 280. Equilibrium theory based upon
the static temperature of the gas predicts that all atoms will be in the
ground state and that none will be in any excited state.

The departure of the densities of the lower excited states from
the equilibrium distribution predicted by the upper excited states is
illustrated further in Fig. 25. In this figure, the abscissa is the
excitation energy of the excited state, and the ordinate is the ratio
of the observed density to the density predicted from calculations based
upon equilibrium with the free electron density. In a plot of this type,
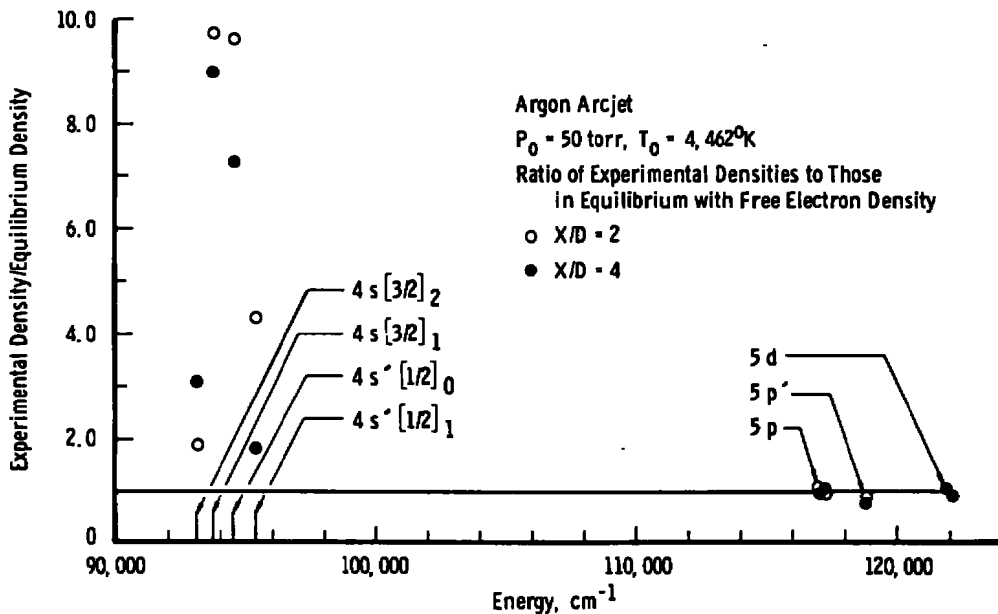
Figure 25. Ratio of measured to equilibrium number densities.

those states whose densities are in equilibrium with the free electron
density have an ordinate of 1.0, as illustrated by those states plotted
in Fig. 25 with excitation energy greater than 116,000 cm^{-1}. Furthermore,
if two states are individually out of equilibrium with the free electron
density but satisfy a collisional equilibrium condition with each other,

they will plot with the same ordinate. These results show that, on the average, the first and fourth excited states are nearest the equilibrium configuration at X/D = 2, being overpopulated by factors of two and four, respectively. The second and third excited states are very strongly out of equilibrium, being nearly an order of magnitude above the equilibrium value. It is interesting to note that these second and third excited state densities have nearly the same ordinate; this condition suggests that, at X/D = 2, some type of collisional equilibrium between these two states may be established.

The data for X/D = 4, plotted in Fig. 25 with the closed symbols, show not only that the numerical values of density of the excited states have changed, but also that the relationship of those densities with respect to the equilibrium configuration has changed. This is particularly notable for the number density of the first excited state, which, at X/D = 4, has decayed to approximately 1/3 its value at X/D = 2 (Fig. 24); however, this density is nearly three times the value demanded by equilibrium (Fig. 25). The other excited states have made progress toward the equilibrium configuration, but the distribution among the states is decidedly nonequilibrium.

4.4 COMPARISON OF EXPERIMENTAL RESULTS WITH ERE CALCULATIONS

One of the objectives of this work was to make comparisons of the nonequilibrium distributions measured for the arcjet plume with calculations performed using the Eigenstate Rate Equation computer program. This system of equations, described in Section 2.2, has the potential of providing a priori predictions of the detailed electronic distribution function in virtually any transient or steady state environment. It is an initial value problem, and some of the underlying assumptions for the ERE in their present form, as well as detailed description of some of the physical processes involved in the arc and nozzle region, preclude computations starting in the cold gas ahead of the arc region of the jets.

However, the distribution function at one point on the axis can provide the initial conditions for prediction of a distribution function at all other downstream axial positions. Thus, as was done here, the distribution function, electron temperature, and electron number density observed at X/D = 2 provide the initial conditions for modeling the plume expansion and predicting the distribution function at X/D = 4.

Some additional compromises are necessary also. The present mathematical model does not include within its framework complete accounting of the mechanisms by which the electrons lose energy, nor does it allow for the possibility of the more energetic electrons diffusing from the plume more rapidly. Consequently, the observed electron temperature at X/D = 2 and 4 was used to provide a position-dependent gradient for the electron temperature. A linear variation between the two axial positions was assumed.

Additionally, the complete excited state distribution function at X/D = 2 is required for the initial conditions, and this was not determined in its entirety. Referring to Fig. 8, one can see that beginning with the $3p^5 4p$ states, the higher excited states are all relatively close together, with the largest separation between adjacent states being less than 3,000 cm^{-1}. It would thus be expected that collisional communication between these excited states and the free electrons would be excellent and that the densities would be maintained in an equilibrium configuration. Hence the initial population density for those states for which direct measurement was not made was chosen to be that density in equilibrium with the free electron density; that is, on a Boltzmann plot similar to Fig. 24, the densities of all excited states above the fourth excited state fall on the straight line at X/D = 2.

The results of the computer calculations are presented in Figs. 26 and 27. Figure 26 is a Boltzmann plot for the calculations similar to Fig. 24, and Fig. 27 provides direct comparison between measurement and
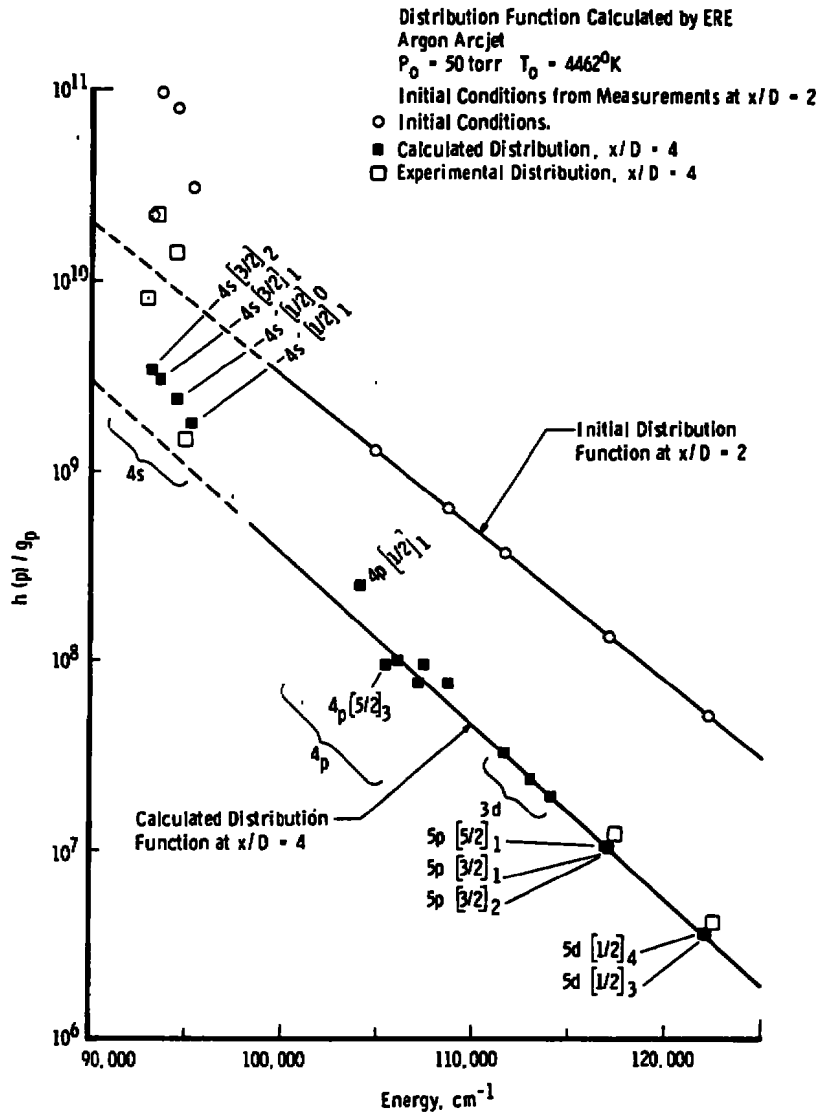
Figure 26. Boltzmann plot of initial conditions and final distribution
function calculated with ERE.

calculations. The initial conditions at X/D = 2 used for the calculations
are included in Fig. 26 and are shown by the open symbols. Those quantum
states not shown explicitly for X/D = 2 were assumed to have densities
on the straight line. The density of states selected from the calculated
distribution function at X/D = 4 are shown by the filled symbols. Those
states not shown fall on the straight line plotted at X/D = 4.
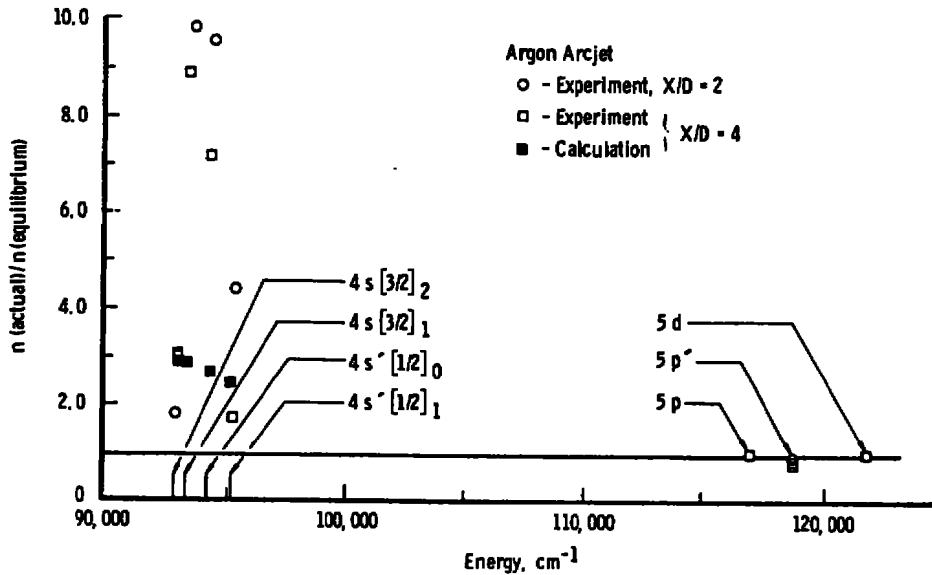
Figure 27. Ratio of calculated and experimental densities to modified Saha equilibrium.

Examining the distribution calculated at X/D = 4, one notes several prominent features. The 4s states appear to have equilibrated toward a Boltzmann type of distribution independent of the other quantum states. This suggests that the calculations include strong collisional coupling between these 4s states which is not evident in the data (Fig. 25). The 4p states at X/D = 4 are calculated with noticeable deviations from their equilibrium value. This could reflect nonequilibrium effects that were not suspected in establishing the initial conditions. All states above the 4p states appear to satisfy the equilibrium relationship, however.

Comparison of the calculated distribution function at X/D = 4 in Fig. 27 to the measured distribution function shown in Fig. 24 suggests some differences between the calculations and measurements. One difference is illustrated in Fig. 27 in a manner similar to that of Fig. 25. The ordinate is the ratio of calculated state density to the equilibrium density for that state. Included for comparison are the experimental data at X/D = 4 from Fig. 25. As is seen, the calculated distribution (closed symbols) is much nearer the equilibrium configuration

than is the physical distribution. This suggests very strongly that the collisional coupling between the states is, in reality, not nearly as strong as predicted from the calculations. In other words, the detailed cross sections computed by the Gryzinski method are too large.

As a final comment upon comparisons of the experiment, Table 8 lists the electron density determined from the measurements and calculated at X/D = 4. As is seen, the calculated electron density is approximately 35 percent less than the density obtained from the experimental measurements. This implies that the rate of recombination is in reality less than calculated and thus supports the idea of the Gryzinski cross sections' being too large. The lower electron density has the effect of reducing the level of the entire distribution, as one may see by comparing Figs. 26 and 24.

Table 8. Calculated and Measured Electron Density at X/D = 4

Determined from Measurement	Calculated
2.19×10^{14}, cm^{-3}	1.54×10^{14}, cm^{-3}

4.5 ENERGY CONTENT CONSIDERATIONS

It is of interest to examine the excited state energy content of the gas that would be expected from classical concepts compared to that based upon the actual observed excited state density distribution. Although there are several modes into which the total energy can be partitioned (for example, kinetic energy of random translational motion, ionization, internal energy, electron heating, etc.), the specific mode of interest here is the energy content of the excited quantum states. The energy content of all the modes is in fact coupled, and nonequilibrium effects in one will influence the others to a greater or lesser degree. However, the data obtained and analyzed in the work here are relevant only to the internal energy mode and do not yield meaningful information concerning the other modes.

The energy content of the excited states can be estimated classically by using the Boltzmann factors and the electron temperature to determine the number density of each excited state. Also of interest for these comparisons is the energy content of the gas due to the random motion of the atoms, characterized by the static temperature. The excited state energy content, along with the static number density, electron density, electron temperature, and static temperature on the centerline at X/D = 2 and 4, is presented in Table 9.

Table 9. Gas Properties and Energy Content of Observed States at X/D = 2 and 4

	X/D = 2	X/D = 4
Static Number Density	4.31×10^{15} cm^{-3}	1.07×10^{15} cm^{-3}
Static Temperature	421°K	204°K
Electron Density	6.3×10^{14} cm^{-3}	2.19×10^{14} cm^{-3}
Electron Temperature	7,760°K	7,200°K
Energy Content of Excited State, Observed	10.8 erg/cm^3	2.2 erg/cm^3
Energy Content of Excited State, Classical	0.027 erg/cm^3	0.0017 erg/cm^3
Energy Content, Random Motion	464 erg/cm^3	45.2 erg/cm^3
Ratio of Observed Excited State Energy Content to Energy of Random Motion	2.33^{-2}	4.87^{-2}
Ratio of Observed Excited State Energy Content to Classical Excited State Energy Content	400	1,300

The comparisons of the excited state energy content predicted classically with that which was actually observed are notable. It is significant that the relative energy content of the internal states is more than two orders of magnitude greater than classical predictions and becomes greater at the larger X/D values. This behavior with X/D occurs because the gas dynamic expansion reduces the collisional and radiative process and produces a partially frozen flow in the characteristic internal electronic energy states. Estimates and predictions of the internal energy

content which rely upon the excited state distribution function or its energy content and do not include the transient coupling, or are based upon classical concepts, can be in error.

5.0 SUMMARY

The work and results reported herein have been accomplished as part of a research program at AEDC to examine the basic processes in nonequilibrium phenomena. The specific work summarized here had as its objective the determination of detailed excited quantum state number densities of argon in the nonequilibrium environment of a freely expanding arcjet plume. As a corollary study, a calculational technique for predicting the transient development of all the detailed quantum state population densities in a monatomic plasma was modified and extended to provide a first approximation to a true modeling of the actual physical experiment being conducted. This analytic study also is unique, and attempts to perform critical experimental and analytical evaluations of the approach have heretofore not been reported in the literature.

In order to accomplish the experimental portion of the study, radiance and absorption profiles of selected spectral lines were taken by traversing a spectrometer field of view across the arcjet plume. The wavelengths of the spectral lines chosen for the radiance profile lay between 415.8 and 604.3 nm, and each had as its upper quantum state one of the upper excited states of the argon atom. The absolute radiance measurements were reduced to the absolute number density radial profile of each of the appropriate excited quantum states by the use of the Abel inversion. The Abel inversion, together with an errors propagation analysis (Ref. 38), yielded number density determinations with typically ±10-percent uncertainties. The number densities of these upper excited states appeared to satisfy quite well the requirements of Saha Equilibrium with the free electron density so that the electron temperature and number density profiles were immediately determinable.

The wavelengths of the spectral lines chosen for the absorption profiles lay between 763.5 and 922.4 nm, and each had for its initial state one of the first four excited states of the argon atom. Absorption data of this type had heretofore not been obtained from arcjet plumes, and it was necessary to develop new analytic techniques to perform radial inversions of measured absorptances to obtain radial profiles of the number density of each of the first four excited states. The radial inversion technique consisted of solving the radiative transfer problem for individual, Doppler-broadened spectral lines through multiple homogeneous zones formed by concentric circles and then conducting the "onion peel" type of radial inversion. Since these states were not expected to fit any specific distribution function, data for several spectral lines were taken as a check on the experimental procedure. The results showed higher population densities than required for equilibrium with the free electron density.

The analytic prediction of the excited state distribution function was accomplished by modifying for argon the system of eigenstate rate equations (ERE) which had been developed previously for helium (Ref. 3) and adding terms to account for the effects of the gas dynamic expansion of the plume from the arcjet. The gas dynamic properties were predicted by use of the Ashkenas-Sherman model for the plume centerline Mach Number and the Rayleigh heating analysis for determining stagnation pressure and temperature at the nozzle exit from measured arc chamber properties. This ERE system of equations requires a large number of fundamental collision parameters, and a simplified approach for their determination based upon the Gryzinski formulation of the collision cross sections was used here. Comparison of the bulk electron-ion recombination coefficient determined from the ERE system of equations with values reported in the literature for argon gave satisfactory agreement.

Results of the experimental and calculational studies may be summarized as follows:

1. The energy within the various available modes of the gas in the plume of an argon arcjet is very definitely distributed in a nonequilibrium manner characterized by a non-Maxwell-Boltzmann population of the distribution of excited state number densities and an electron temperature that is much greater than the static gas temperature.

2. The nonequilibrium nature of the excited state distribution function is most pronounced among the first four excited states; the densities of these resonance and metastable states are from two to ten times larger than the density required by equilibrium considerations at the free electron temperature.

3. Any patterns in the nonequilibrium distribution of the first four excited states could not be detected, and no pronounced evidence of collisional or radiative coupling between the states was found. The $4s'[1/2]_1$ and $4s[3/2]_1$ states both have a strong radiative transition to the ground state, and because of their pronounced elevation above equilibrium densities, the plasma appeared to be optically thick to this radiation, in agreement with independent calculations of the optical depth.

4. The calculation of the detailed distribution function with the ERE showed generally much stronger collisional coupling between the states and a much faster relaxation toward the equilibrium distribution function than was observed in the data. This is

attributed to the inability of the Gryzinski method to
correctly predict the detailed excitation/de-excitation
cross sections for the electron-argon atom collisions,
although on an overall basis, the inaccuracies appear to
average out, as was evidenced by a reasonable prediction of
the gross electron-ion recombination rate.

5. The radial profile of the electron temperature obtained
   from the radiance data showed unexpected structure,
   being cooler on the centerline at X/D = 4 than on the
   outer periphery of the jet. The location and nature of
   the structure are consistent with the possible location
   of the plume barrel shock, with attendent heating of
   the free electrons. The apparent location of the
   barrel shock structure from the experimental data was
   nearer the centerline than was predicted by a method of
   characteristics calculation for the plume expansion.

6. The nonequilibrium distribution function observed in
   the arcjet expansion contained two to three orders of
   magnitude more energy than is predicted from classical
   concepts. The relative amount of energy in the internal
   energy states increases as the plume expands. At four
   nozzle diameters downstream of the nozzle exit
   plane, the internal energy amounted to 5 percent of the
   energy of random translational motion.

In conclusion, these unique experiments and predictive calcula-
tions have shown that there can be a pronounced nonequilibrium distribution
of internal energy states in the rapid expansion to low densities of a
high enthalpy source such as an arcjet. The extent of nonequilibrium is
such that there is significantly more energy contained in the upper
excited states than is predicted by any classical approach. Moreover, the

distribution function can be obtained only by measurement of the densities of the excited states or by calculations which include the transient and coupled processes contributing to the rate of change of the density of each excited state. The approach taken here will be useful for such predictions with a more correct accounting of the cross sections. Continued development of the calculational approach and experimental attack can provide, ultimately, predictive and analytical techniques which will apply to any nonequilibrium flow environment.

REFERENCES

1. Lewis, J. W. L., Price, L. L., and Kinslow, M. "Rotational Relaxation of N_2 in Heated Expansion Flow Fields." Rarefied Gas Dynamics: Proceedings of the Ninth International Symposium on Rarefied Gas Dynamics, Gottingen, West Germany, July 1974.

2. Limbaugh, C. C., McGregor, W. K., and Mason, A. A. "Numerical Study of the Early Population Density Relaxation of Thermal Hydrogen Plasmas." AEDC-TR-69-156 (AD695472), October 1969.

3. Limbaugh, C. C. "The Transient Behavior of Collisional-Radiative Recombination in Atomic Helium Plasma." PhD Dissertation, The University of Tennessee Space Institute, December 1971.

4. Limbaugh, C. C. and Mason, A. A. "Validity of the Quasisteady State and Collisional-Radiative Recombination for Helium Plasmas. I. Pure Afterglows." Physical Review A, Vol. 4, No. 6, December 1971, pp. 2368-2377.

5. Limbaugh, C. C. and McGregor, W. K. The Transient Behavior of Quantum State Density Distributions in Atomic Helium Plasmas." Rarefied Gas Dynamics: Proceedings of the Eighth International Symposium on Rarefied Gas Dynamics, Stanford, California, July 1972.

6. McGregor, W. K., Dooley, M. T., and Brewer, L. E. "Diagnostics of a Plasma Flame Exhausting to Atmospheric Pressure." AEDC-TR-61-16 (AD269499), January 1962.

7. Brewer, L. E. "Plasma Radiation Resulting from an Over Population of Atoms in the Metastable State." Master's Thesis, University of Tennessee Space Institute, March 1965.

8. Brewer, L. E. and McGregor, W. K. "The Radiative Decay of Metastable Argon Atoms in a Low-Density Argon Plasma Stream." AEDC-TR-63-5 (AD294543), January 1963.

9. McGregor, W. K. "Examination of the Conservation Laws in a Particular Class of Collisions of the Second Kind." PhD Dissertation, University of Tennessee Space Institute, June 1969.

10. Drawin, H. W. "Collisional-Radiative Ionization and Recombination Coefficients for Quasi-Stationary Homogeneous Hydrogen and Hydrogenic Ion Plasmas." Z. Physik, Vol. 225, 1969, pp. 470-482.

11. Collins, C. B. and Robertson, W. W. "Helium Afterglow. I. Atomic Spectrum." Journal of Chemical Physics, Vol. 40, No. 8, 15 April 1964, pp. 2202-2208.

12. Robben, F., Kunkel, W. B., and Talbot, L. "Spectroscopic Study of Electron Recombination with Monatomic Ions in a Helium Plasma." Physical Review, Vol. 132, No. 6, 15 December 1963, pp. 2363-2371.

13. Park, C. "Comparison of Electron and Electronic Temperatures in Recombining Nozzle Flow of Ionized Nitrogen-Hydrogen Mixture. Part 1. Theory." *Journal of Plasma Physics*, Vol. 9, Part 2, April 1973, pp. 187-215.

14. Park, C. "Comparison of Electron and Electronic Temperatures in Recombining Nozzle Flow of Ionized Nitrogen-Hydrogen Mixture. Part 2. Experiment." *Journal of Plasma Physics*, Vol. 9, Part 2, April 1973, pp. 217-234.

15. Bowen, S. W. and Park, C. "Computer Study of Nonequilibrium Excitation in Recombining Nitrogen Plasma Nozzle Flows." *AIAA Journal*, Vol. 9, No. 3, March 1971, pp. 493-499.

16. Hogarth, W. L. and McElwain, D. L. S. "Internal Relaxation, Ionization and Recombination in a Dense Hydrogen Plasma. II. Population Distributions and Rate Coefficients." *Proceedings of the Royal Society of London*, A 345, 1975, pp. 265-276.

17. Hey, J. D. "Criteria for Local Thermal Equilibrium in Non-Hydrogenic Plasmas." *Journal of Quantitative Spectroscopy and Radiative Transfer*. Vol. 16, 1976, p. 69.

18. Ashkenas, H. and Sherman, F. S. "The Structure and Utilization of Supersonic Free Jets in Low Density Wind Tunnels. *Rarefied Gas Dynamics: Proceedings of the Fourth International Symposium on Rarefied Gas Dynamics*, Toronto, Canada, 1964. Supplement 3, Vol. II, Academic Press, Inc., New York, 1966, pp. 84-105.

19. Witte, A. B. Part I: "Experimental Investigation of an Arc-Heated Supersonic Free Jet." Part II: "Analysis of One-Dimensional Isentropic Flow for Partially Ionized Argon." PhD Dissertation, California Institute of Technology, Pasadena, 1967.

20. Bryson, R. J. "A Method for Determining the Bulk Properties of Arc-Heated Argon." AEDC-TR-69-125 (AD689178), June 1969.

21. Moore, C. E. Atomic Energy Levels, Vol. I. National Bureau of Standards, Washington, D.C., 1949.

22. Cowan, R. D. and Andrew, K. L. "Coupling Considerations in Two-Electron Spectra." Journal of the Optical Society of America, Vol. 55, No. 5, May 1965, pp. 502-516.

23. Wiese, W. L., Smith, M. W., and Miles, B. M. "Atomic Transition Probabilities. Volume II, Sodium Through Calcium. NSRDS-NBS 22, National Bureau of Standards, Washington, D.C., 1969.

24. Green. L. C., Rush, P. P., and Chandler, C. D. "Oscillator Strengths and Matrix Elements for the Electric Dipole Moment for Hydrogen." Abstract in Astrophysical Journal, Vol. 125, No. 3, 1957, p. 835.

25. Gryziński, M. "Two-Particle Collisions. I. General Relations for Collisions in the Laboratory System." Physical Review, Vol. 138, No. 2A, 19 April 1965, pp. A305-A321.

26. Gryziński, M. "Two-Particle Collisions. II. Coulomb Collisions in the Laboratory System of Coordinates." Physical Review, Vol. 138, No. 2A, 19 April 1965, pp. A322-A335.

27. Gryziński, M. "Classical Theory of Atomic Collisions. I. Theory of Inelastic Collisions." Physical Review, Vol. 138, No. 2A, 19 April 1965, pp. A336-A358.

28. Zapesochnyi, I. P. and Feltsan, P. V. "On the Excitation Cross Sections of 2p Levels of Argon, Krypton, and Xenon." Optics and Spectroscopy, Vol. 20, 1966, p. 291.

29. Ganas, P. S. and Green, A. E. S. "Electron Impact Excitation
    of the Rare Gases." Physical Review A, Vol. 4, No. 1, July
    1971, pp. 182-193.

30. Wallace, S. J., Berg, R. A., and Green, A. E. S. "Electron-
    Impact Ionization of Ne and Ar in the Eikonal and Born
    Approximations." Physical Review A, Vol. 7, No. 5, May
    1973, pp. 1616-1629.

31. Seaton, J. J. "Radiative Recombination of Hydrogenic Ions."
    Monthly Notices of the Royal Astronomical Society, Vol. 119,
    No. 2, 1959, pp. 81-89.

32. Kelly, H. P. and Simons, R. L. "Photoabsorption by Neutral
    Argon Calculated by Many-Body Perturbation Theory." Physical
    Review Letters, Vol. 30, No. 12, 19 March 1973, pp. 529-532.

33. Wanless, D. "Electron-Ion Recombination in Argon." Journal
    of Physics B, Vol. 4, 1971, pp. 522-527.

34. Chen, C. J. "Collisional-Radiative Electron-Ion Recombination
    Rate in Rare-Gas Plasmas." The Journal of Chemical Physics,
    Vol. 50, No. 4, 15 February 1969, pp. 1560-1566.

35. Sprouse, J. A. and Few, J. D. "Electron Density Profile
    Measurements." AEDC-TR-74-40 (AD781064), June 1974.

36. McGregor, W. K., Few, J. D., and Litton, C. D. "Resonance Line
    Absorption Method for Determination of Nitric Oxide
    Concentration." AEDC-TR-73-182 (AD771642), December 1973.

37. Fox, J. H. "An Axially Symmetric, Inviscid, Real Gas, Non-Isoenergetic Solution by the Method of Characteristics." Master's Thesis, The University of Tennessee Space Institute, 1968.

38. Shelby, R. T. and Limbaugh, C. C., "Smoothing Technique and Variance Propagation for Abel Inversion of Scattered Data. AEDC-TR-76-123, to be published.

APPENDIX A
TECHNIQUE FOR RADIAL INVERSION OF NARROW
SPECTRAL LINE ABSORPTION DATA

One of the objectives of the experimental work reported here was to determine the number densities of lower excited states on the center-line of the argon arcjet pume. The radiative transitions from these lower excited states are generally of very short wavelength in the vacuum ultraviolet and are experimentally inaccessible. Others of these lower excited states are metastable and have no allowed radiative transitions to a lower state. Hence, emission spectroscopy will not yield convenient data which can be interpreted in terms of number densities. However, each of the first four excited states is the lower excited state of a very strong spectral line emitted in the 700- to 930-nm wavelength range. This wavelength range is readily accessible experimentally, and resonance absorption measurements can, by use of a proper radiative transfer model, be related to the number density of atoms in each of the first four excited states.

The development of an inversion procedure for determining local number densities from measured absorptions is based upon radiative transport theory and requires knowledge of the spectral line broadening (Ref. A-1). There are four types of physical processes which can contribute to the finite width of a spectral emission or absorption line. These processes may be listed as follows:

1. Natural broadening caused by the finite lifetime of the excited state.

2. Doppler broadening caused by the random motion of the atoms

3. Pressure or collision broadening caused by collisions of the emitting or absorbing atom with other atoms.

4. Stark broadening caused by the collisions with ions and electrons.

The experimental conditions to be encountered in this work are all at low static pressures (p < 0.3 torr), and pressure broadening (process 3) may be ignored (Ref. A-1). The natural line width is inversely proportional to the oscillator strength for the transition, and the spectral lines used for this work are all very strong. Therefore, natural broadening (process 1) is negligible here. An estimate of Stark broadening can be made using Table 4-5 in Griem (Ref. A-2). Griem gives, for the 772.4-nm spectral line at 10,000°K, a half width of 7.05×10^{-3} nm at an electron density of 10^{16} cm^3. At the conditions of the experiment conducted here, the electron density is of order 10^{14}, and the consequent half width due to Stark broadening is 7.05×10^{-5} nm. This is to be compared to the Doppler-broadened half width of 1.2×10^{-3} nm at a heavy body temperature of 200°K (characteristic of static temperature in the arcjet plume) and a wavelength of 772.4 nm. Thus, the only broadening mechanism to be considered important is the Doppler broadening (process 2).

The transmittance, τ, of an absorbing medium may be expressed

$$\tau = \frac{I_\nu}{I_{\nu_0}^o} = \frac{\int I_{\nu_0} \exp\left(-\int k_\nu d\ell\right)_{d\nu}}{\int I_{\nu_0} \, d\nu} \tag{A-1}$$

where the frequency limits of integration are over the entire width of the line of interest and the symbols are defined as follows. I_{ν_0} is the frequency-dependent intensity of the source line, which is assumed to be Doppler broadened:

$$I_{\nu_0} = I_{\nu_0}^o \exp\left\{-\left[\frac{2(\nu-\nu_0)\sqrt{\ell n2}}{(\Delta_s \nu)_D}\right]^2\right\} \tag{A-2}$$

The Doppler half-widths of the source lines are given by

$$(\Delta_s \nu)_D = 2 \nu_0 \left(\frac{2 \ln 2 k T_s}{M_s c^2} \right)^{\frac{1}{2}} \qquad \text{(A-3)}$$

where $(\Delta_s \nu)_D$ is the width at half maximum intensity, ν_0 is the central frequency of the source spectral line, k is Boltzmann's constant, T_s is the temperature of the source molecules, M_s is the molecular mass of the emitting specie, c is the speed of light, and $I_{\nu_0}^0$ is the intensity of the line peak. With the absorber assumed to be Doppler broadened, the absorption coefficient, k_ν, is given by

$$k_\nu = k_\nu^0 \exp \left\{ - \left[\frac{2\sqrt{\ln 2} \, (\nu - \nu_0)}{(\Delta_a \nu)_D} \right]^2 \right\} \qquad \text{(A-4)}$$

where the absorber Doppler half-width is given by .

$$(\Delta_a \nu)_D = 2 \nu_0 \left(\frac{2 \ln 2 k T_a}{M_a c^2} \right)^{\frac{1}{2}} \qquad \text{(A-5)}$$

where $(\Delta_a \nu)_D$ is the absorber line width at half the maximum absorption coefficient, T_a is the static temperature of the absorber molecule, and M_a is the mass of the absorber molecule. It is shown (Ref. A-1) that

$$k_\nu^0 = \left(\frac{e^4 M_a}{m_e} \right)^{\frac{1}{2}} \left(\frac{\pi}{2 m_e c^2 k T_a} \right)^{\frac{1}{2}} \frac{N_a f}{\nu_0} \qquad \text{(A-6)}$$

where e is the charge on the electron, m_e is the electron mass, N_a is the number density of the absorbing molecule, and f is the oscillator strength of the spectral transition. As is seen in Eqs. (A-5) and (A-6), k_ν is a function of N_a and T_a and, in Eq. (A-1), is integrated over the length of the absorbing medium. If the nonhomogeneous absorbing medium is modeled by a series of small homogeneous zones of length ℓ_i, with

constant properties across the spatial extent of each zone, the spatial integration can be approximated by the summation

$$\exp\left(-\int k_\nu d\ell\right) = \exp\left\{-\left(\frac{M_a \pi e^4}{2m_e^2 c^2 k}\right)^{1/2} \frac{f}{\nu_0} \sum_i \frac{N_{a_i}}{T_{a_i}} \ell_i \exp\left[-\frac{M_a c^2 (\nu - \nu_0)^2}{2\nu_0 k T_{a_i}}\right]\right\}$$

(A-7)

where the i index runs over the spatial extent of the absorbing medium. Substituting Eqs. (A-2) thru (A-7) into Eq. (A-1) and collecting terms one can write

$$\tau = \frac{\int \exp\left[-C_0(\nu - \nu_0)^2\right] \exp\left\{-\left[C_1 \sum_i \frac{N_{a_i}}{T_{a_i}^{1/2}} \ell_i \exp\left[-\frac{C_2(\nu - \nu_0)^2}{T_{a_i}}\right]\right]\right\} d\nu}{\int \exp\left[-C_0(\nu - \nu_0)^2\right] d\nu}$$

(A-8)

where

$$C_0 = \frac{M_s c^2}{2\nu_0^2 k T_s}$$

$$C_1 = \left(\frac{\pi M_a e^4}{2m_e^2 k}\right)^{1/2} \frac{f}{\nu_0}$$

$$C_2 = \frac{M_a c^2}{2\nu_0^2 k}$$

In the specific experimental work reported here, cylindrical symmetry of the absorbing medium, the arcjet plume, is assumed. The measurements of transmission of the plume are made as a function of displacement across the plume. This situation is illustrated schematically in Fig. A-1. Each measurement corresponds to the transmission through the plume over a region defined by the spatial resolution of the instrumentation. Assuming that the plume properties are homogeneous throughout each cylindrical section defined by this spatial resolution, the local number density profile of the absorbing molecules in the
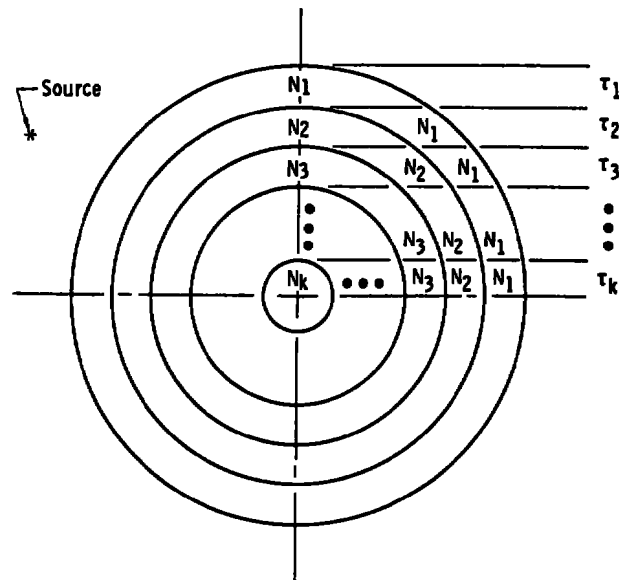
Figure A-1. Conceptual schematic of arcjet plume
cross section and measurements for
absorption inversions.

plume is available from solution of Eq. (A-8). At the outer edge of
the plume, there is only one homogeneous zone contributing to the
absorption. If the static temperature profile is specified, the number
density of this zone, N, is the only unknown in Eq. (A-8), and the
summation is over only one zone. With the number density in this zone
determined, the only unknown density contributing to the next inward
measured transmission is that of the central zone, N_2, which becomes the
only unknown in Eq. (A-8). Solution of Eq. (A-8) for N_2 provides the data
that leaves N_3 the only indeterminant density for the next inward mea-
surement, τ_3. By proceeding inward in this manner, one can determine
the complete number density profile for the absorbing specie in the
plume.

For simplicity, it is convenient to define the functions

$$F(\nu) = C_o(\nu - \nu_0)^2 + C_1 \sum_{i \neq I} \frac{N_{a_i}}{T_{a_i}} \ell_i \exp\left[-C_2(\nu - \nu_0)^2/T_{a_i}\right]$$

$$G(\nu) = \frac{C_1}{T_{aI}^{1/2}} \, \ell_I \exp\left[-C_2(\nu - \nu_0)^2/T_{aI}\right]$$

$$H(\nu) = C_0(\nu - \nu_0)^2$$

where the subscript I corresponds to the central zone for which the number density is being determined. With these definitions, Eq. (A-8) can be written

$$\tau = \frac{\int \exp\left[-F(\nu)\right] \exp\left[-G(\nu)N_{ai}\right] d\nu}{\int \exp\left[-H(\nu)\right] d\nu} \tag{A-9}$$

in which the only unknown parameter is the number density to be attributed to the central zone, N_{a_I}.

In general, the integration in Eq. (A-9) will not be analytically tractable. It must, therefore, be attacked by numerical methods. There are many methods appropriate for this calculation, and the specific method used here was the trapezoidal rule. Applying the technique to Eq. (A-9) results in an analytical description which may be written

$$\tau = \frac{\displaystyle\sum_{j=1}^{J} \left\{ \exp\left[-F(\nu_j)\right] \exp\left[-G(\nu_j)N_{a_I}\right] + \exp\left[-F(\nu_{j+1})\right] \exp\left[-G(\nu_{j+1})N_{a_I}\right] \right\}}{\displaystyle\sum_{j=1}^{J} \left\{ \exp\left[-H(\nu_j)\right] + \exp\left[-H(\nu_{j+1})\right] \right\}} \tag{A-10}$$

where

$$\Delta\nu = \text{integration stepsize}$$

$$\nu_j = \nu_0 + (j - 1)\Delta\nu$$

$$J = \frac{\nu_j - \nu_0}{\Delta\nu}$$

By equating Eq. (A-10) to the appropriate experimental measurement, one can write a single equation in the single unknown, N_{a_I}. The N_{a_I} is determined iteratively by the Newton-Raphson method.

In general, the description of the transmission must include considerations of the spectral characteristics of the measuring instrument. If the spectral lines of interest are much narrower than the equivalent slit width of the instrument (which was always true for these experiments), then the intensity of a spectral line is just proportional to the indicated peak of the spectrometer detector signal, and no special attention need be given to the instrument bandpass function. More complete details of the treatment of spectral instruments are given in Ref. A-3.

REFERENCES

A-1. Mitchell, A. C. G. and Zemansky, M. W. Resonance Radiation and Excited Atoms. Cambridge University Press, Cambridge, England, 1934.

A-2. Griem, H. R. Plasma Spectroscopy. McGraw Hill, New York, 1964.

A-3. Davis, M. G., McGregor, W. K., and Few, J. D. "Spectral Simulation of Resonance Band Transmission Profiles for Species Concentration Measurements: NO-Bands as an Example. AEDC-TR-74-124 (ADA004105), January 1975.

APPENDIX B
SPECTRAL RADIANCE PROFILES, TRANSMITTANCE PROFILES,
AND EMISSION COEFFICIENT PROFILES
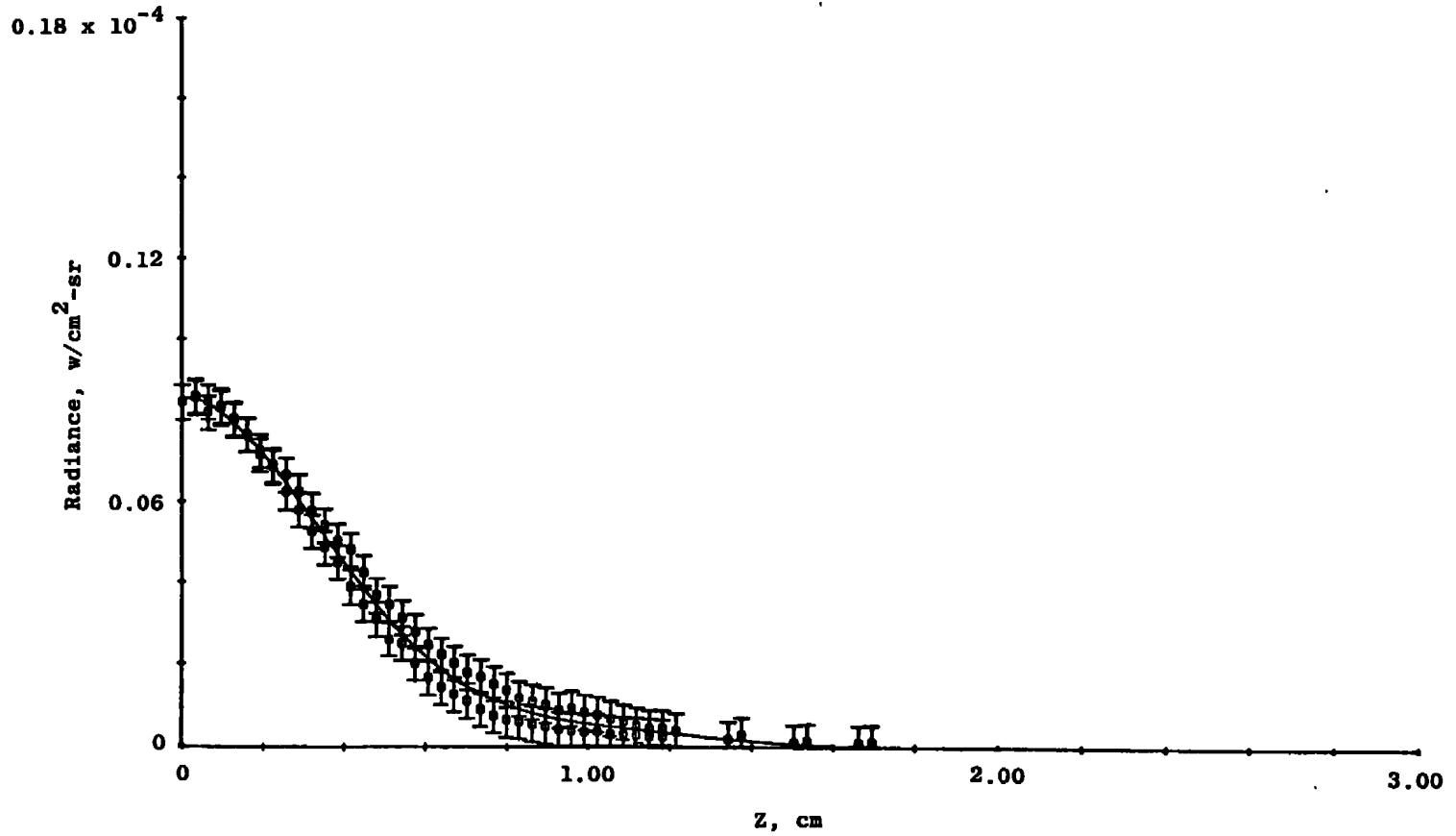
Figure B-1. Spectral radiance at 430.0 nm, X/D = 2.
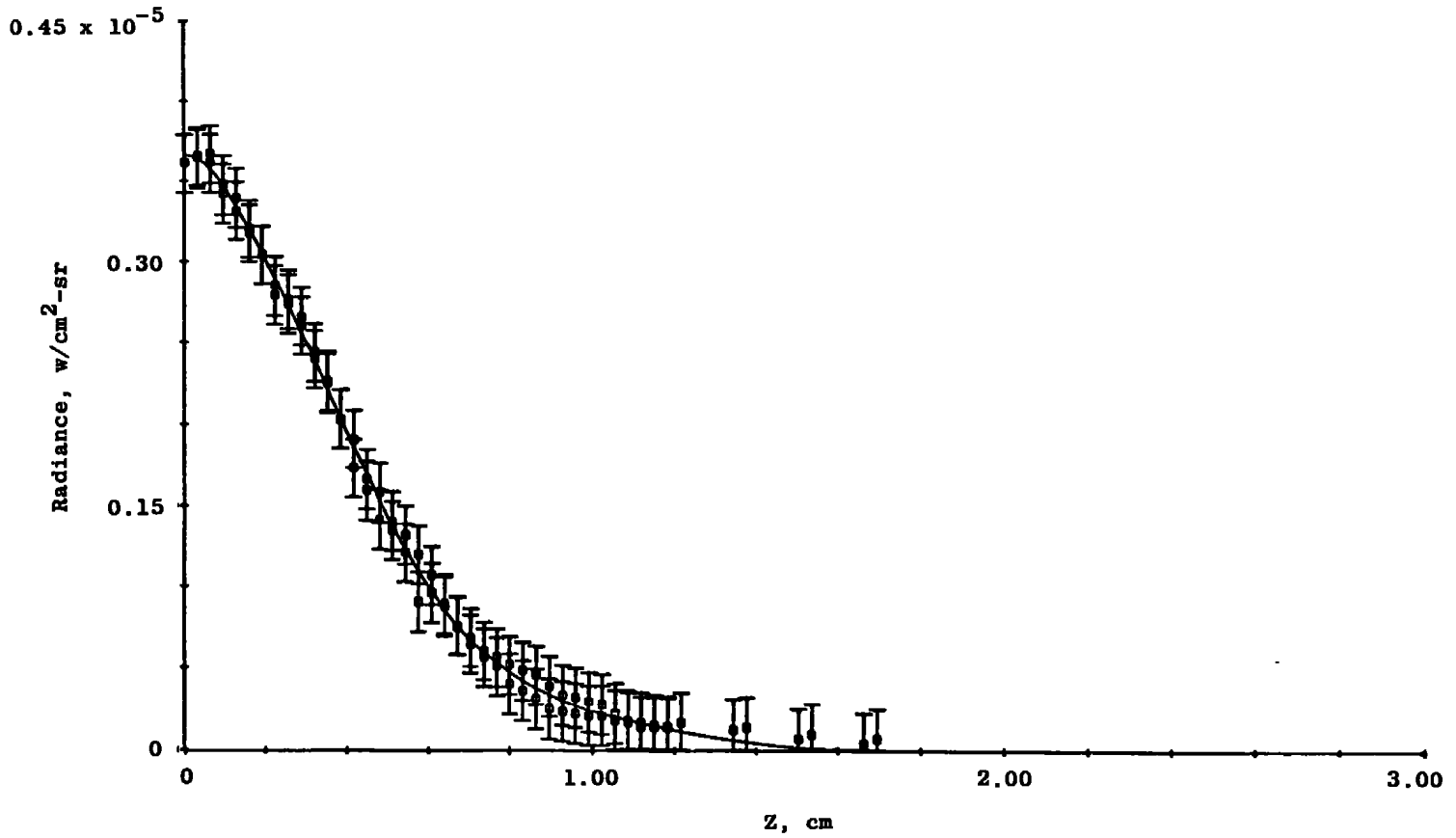
Figure B-2. Spectral radiance at 416.4 nm, X/D = 2.
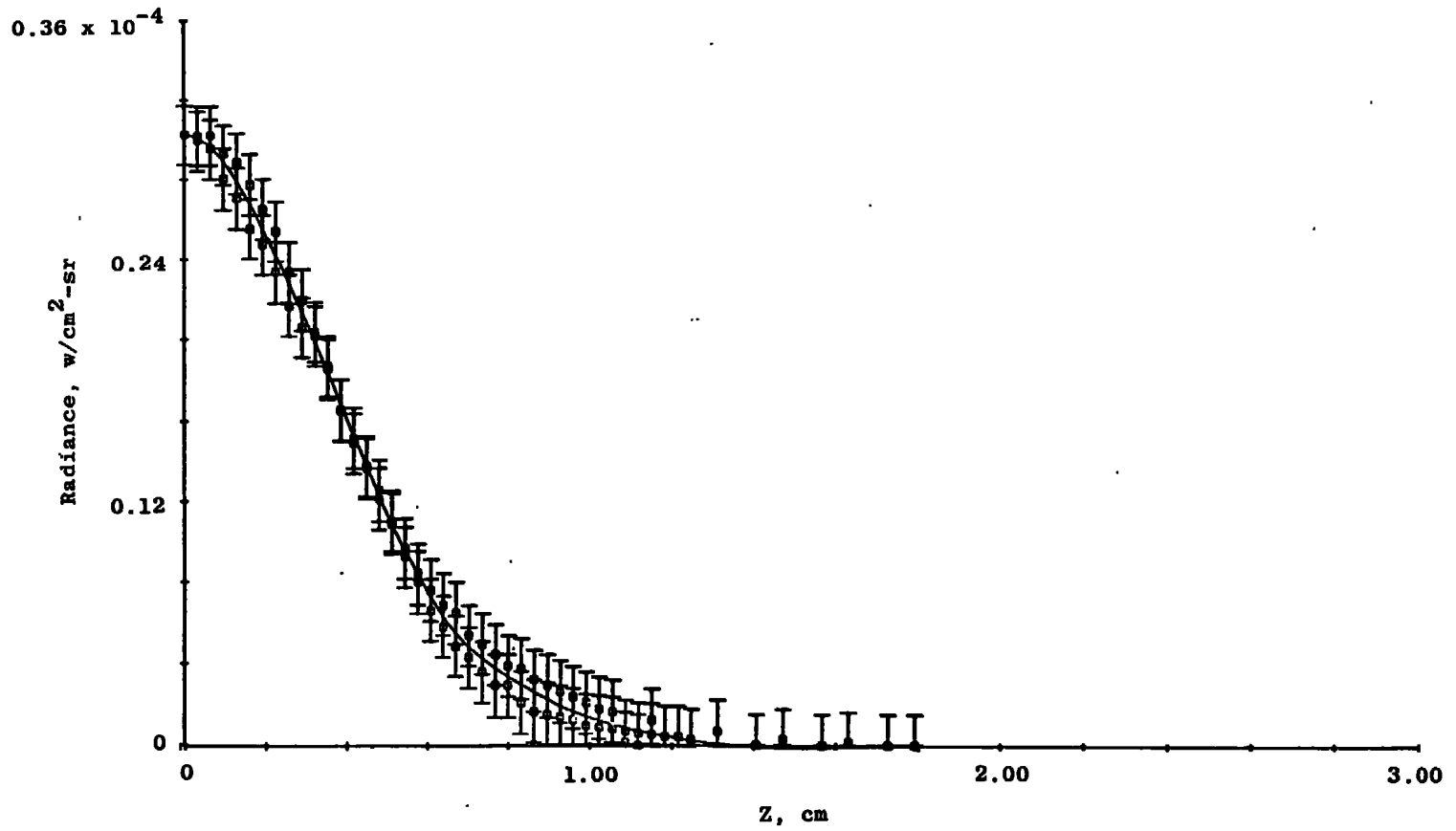
Figure B-3. Spectral radiance at 415.8 nm, X/D = 2.
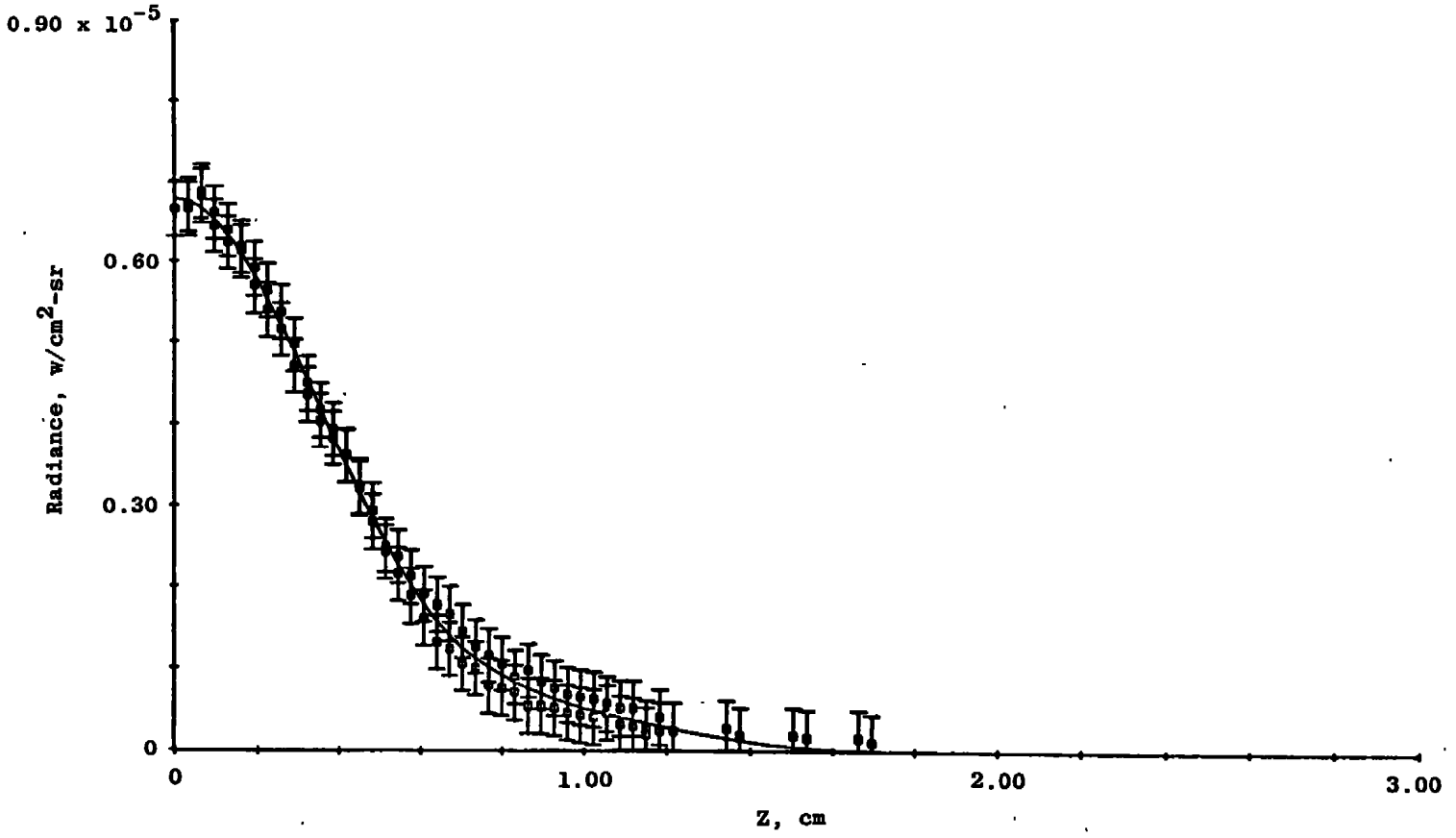
Figure B-4. Spectral radiance at 426.6 nm, X/D = 2.
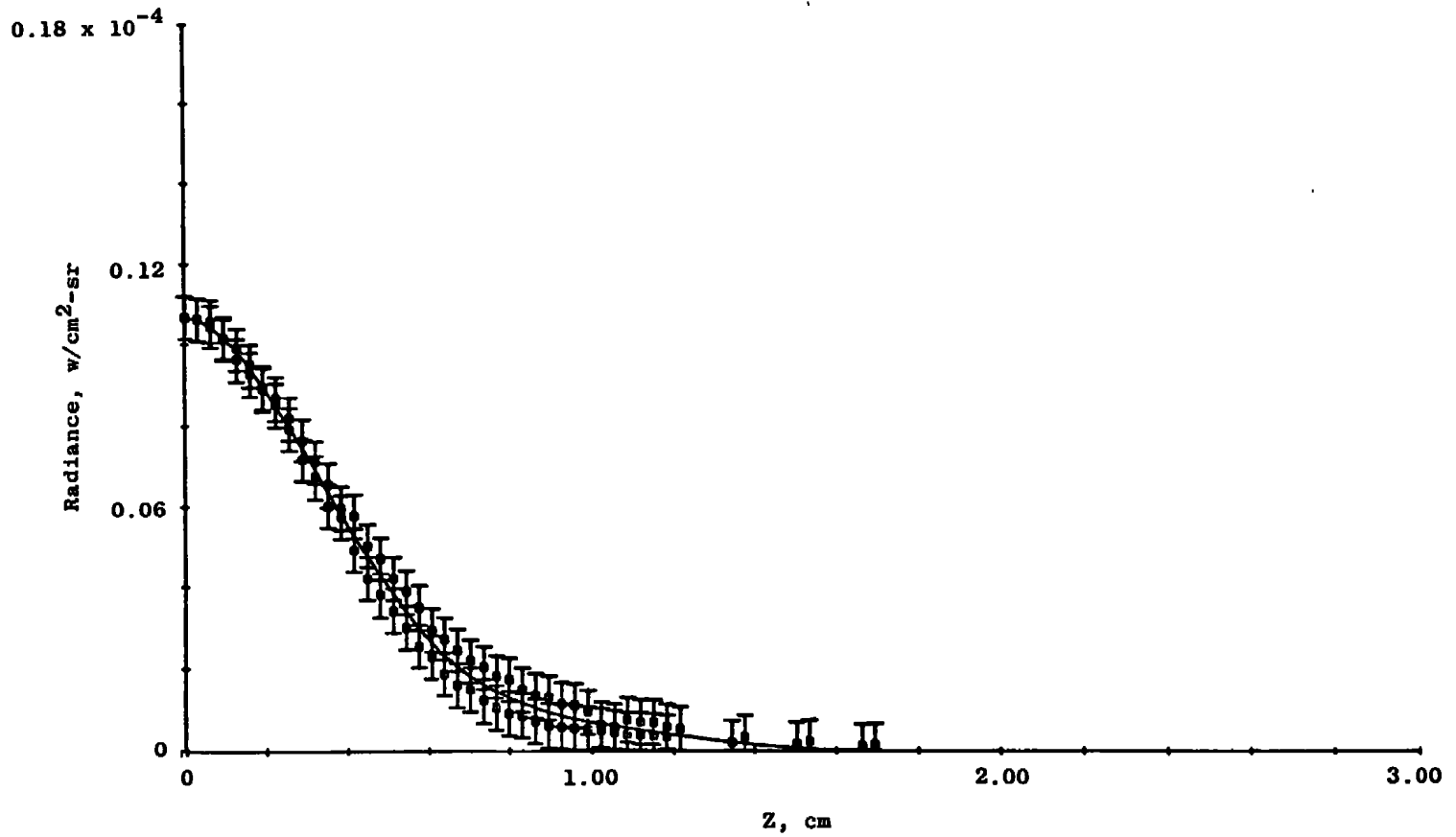
Figure B-5. Spectral radiance at 425.9 nm, X/D = 2.
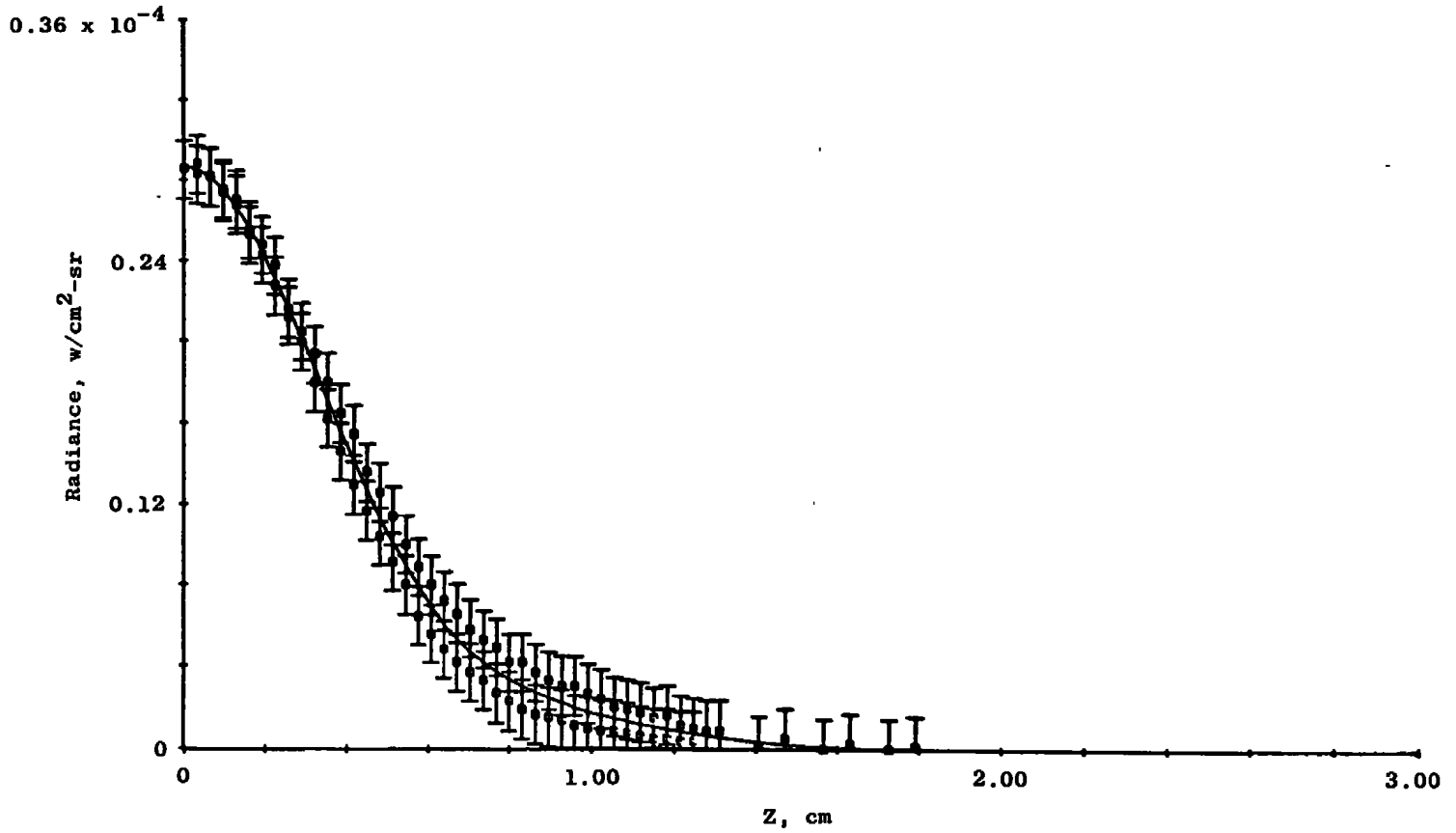
Figure B-6. Spectral radiance at 603.2 nm, X/D = 2.
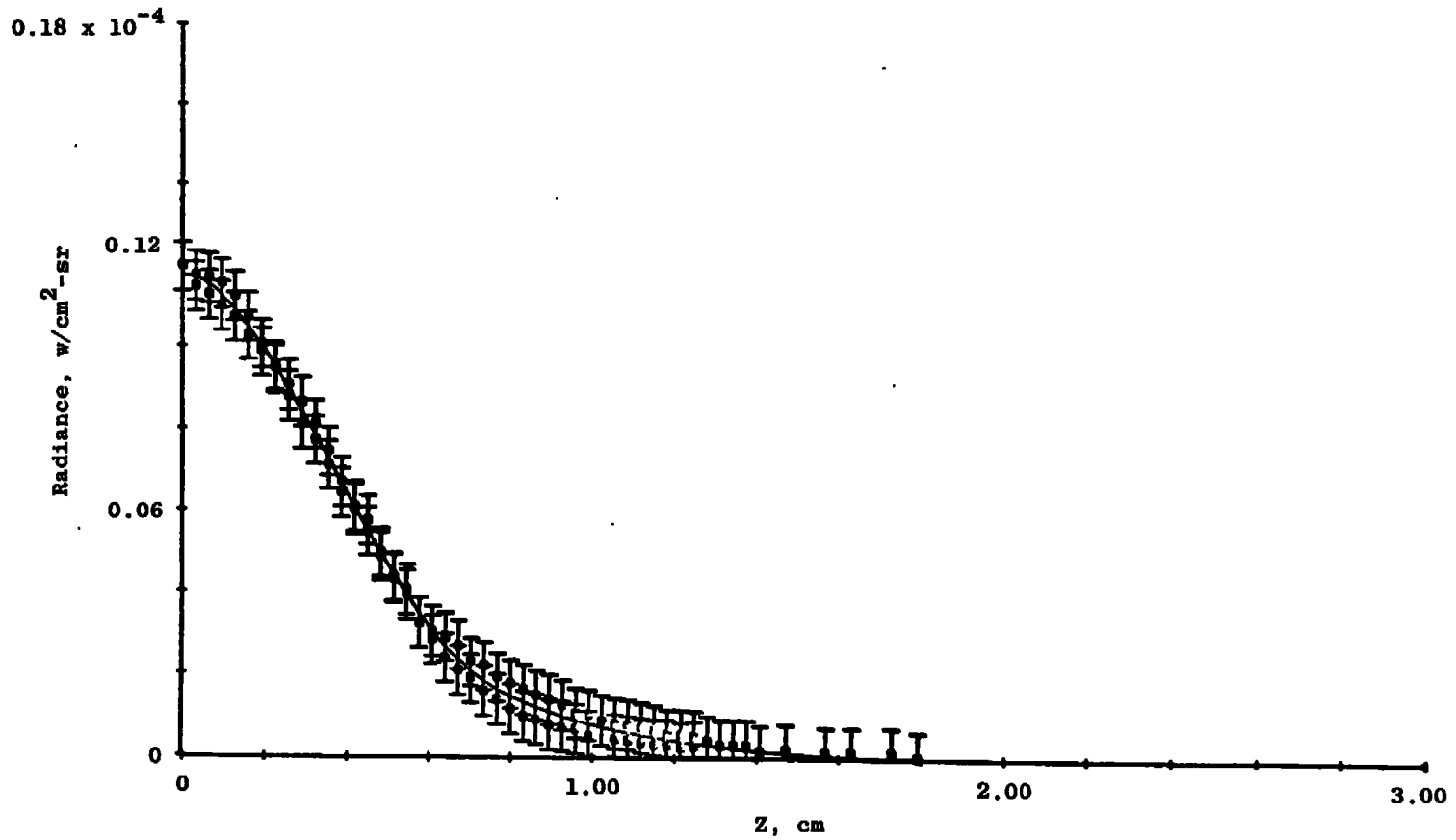
Figure B-7. Spectral radiance at 604.3 nm, X/D = 2.
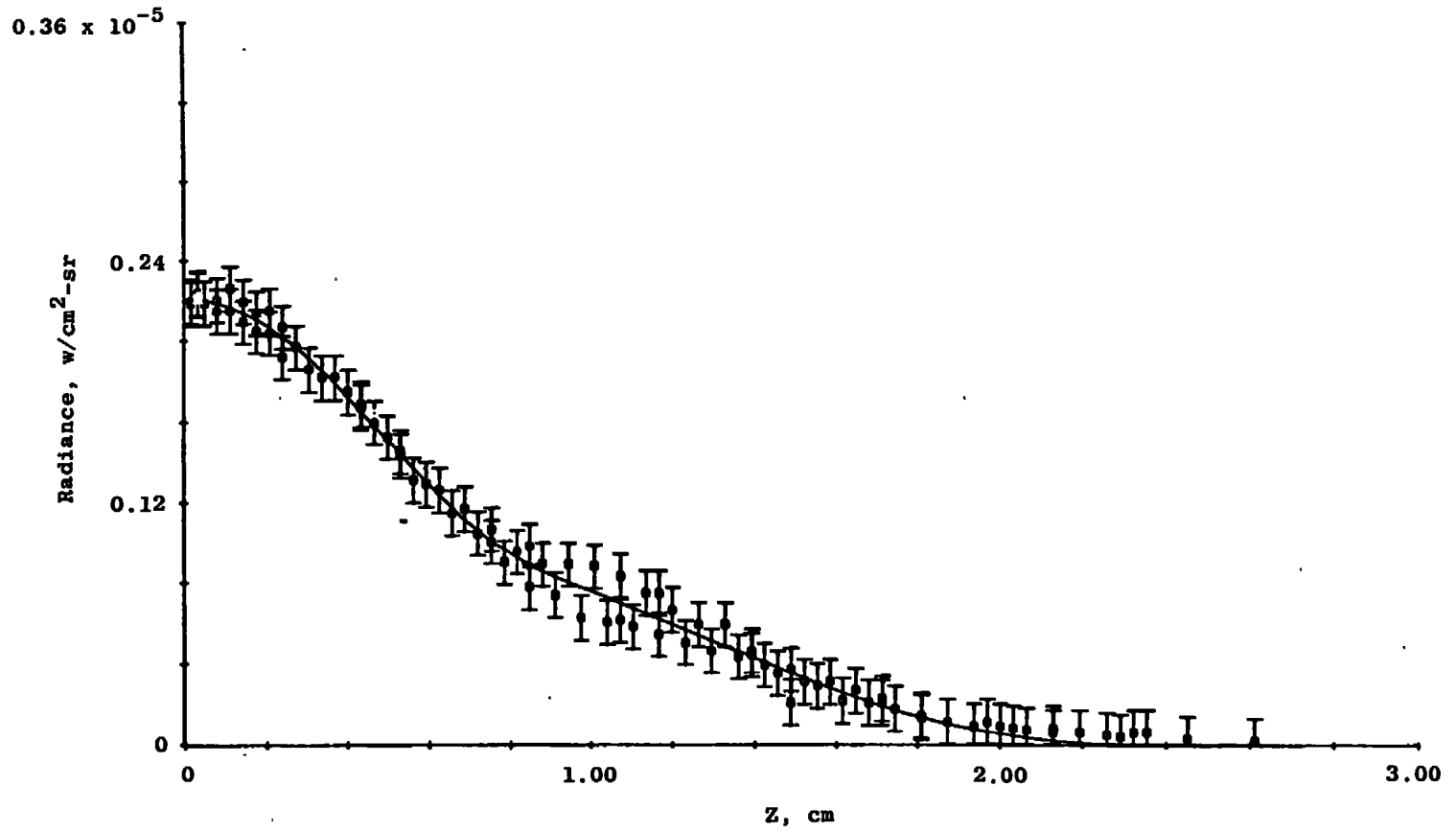
Figure B-8. Spectral radiance at 430.0 nm, X/D = 4.
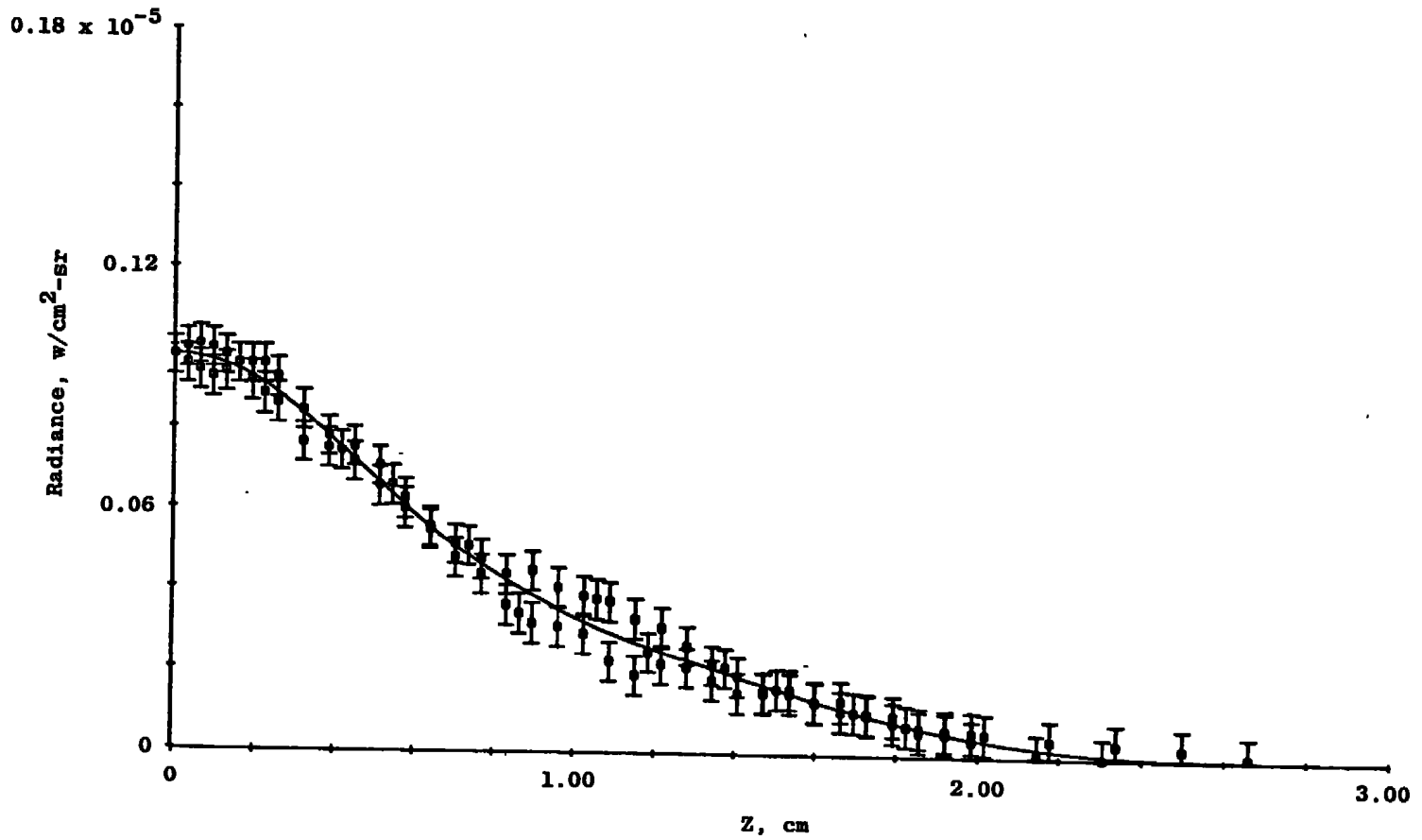
Figure B-9. Spectral radiance at 416.4 nm, X/D = 4.
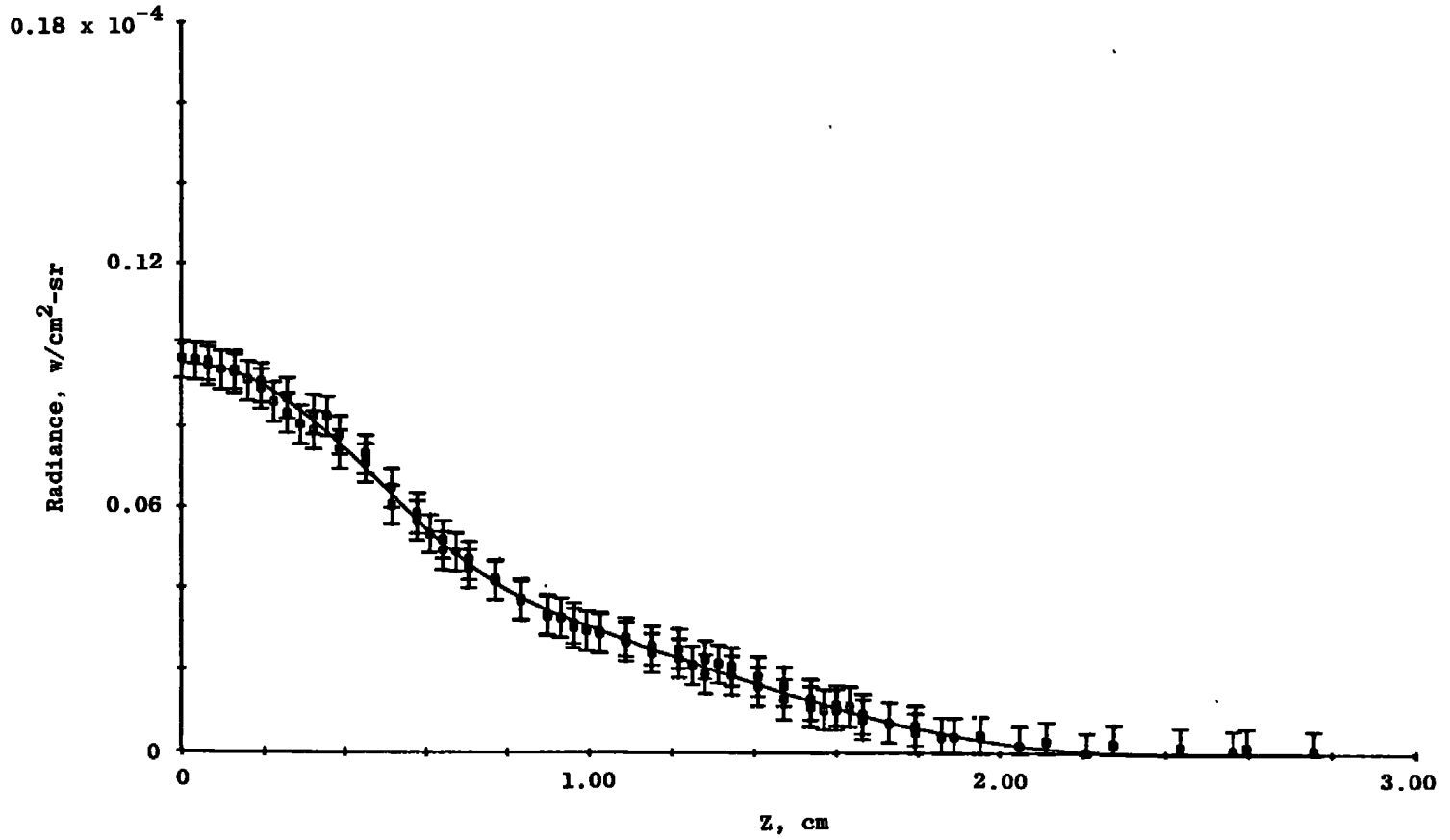
Figure B-10. Spectral radiance at 415.8 nm, X/D = 4.
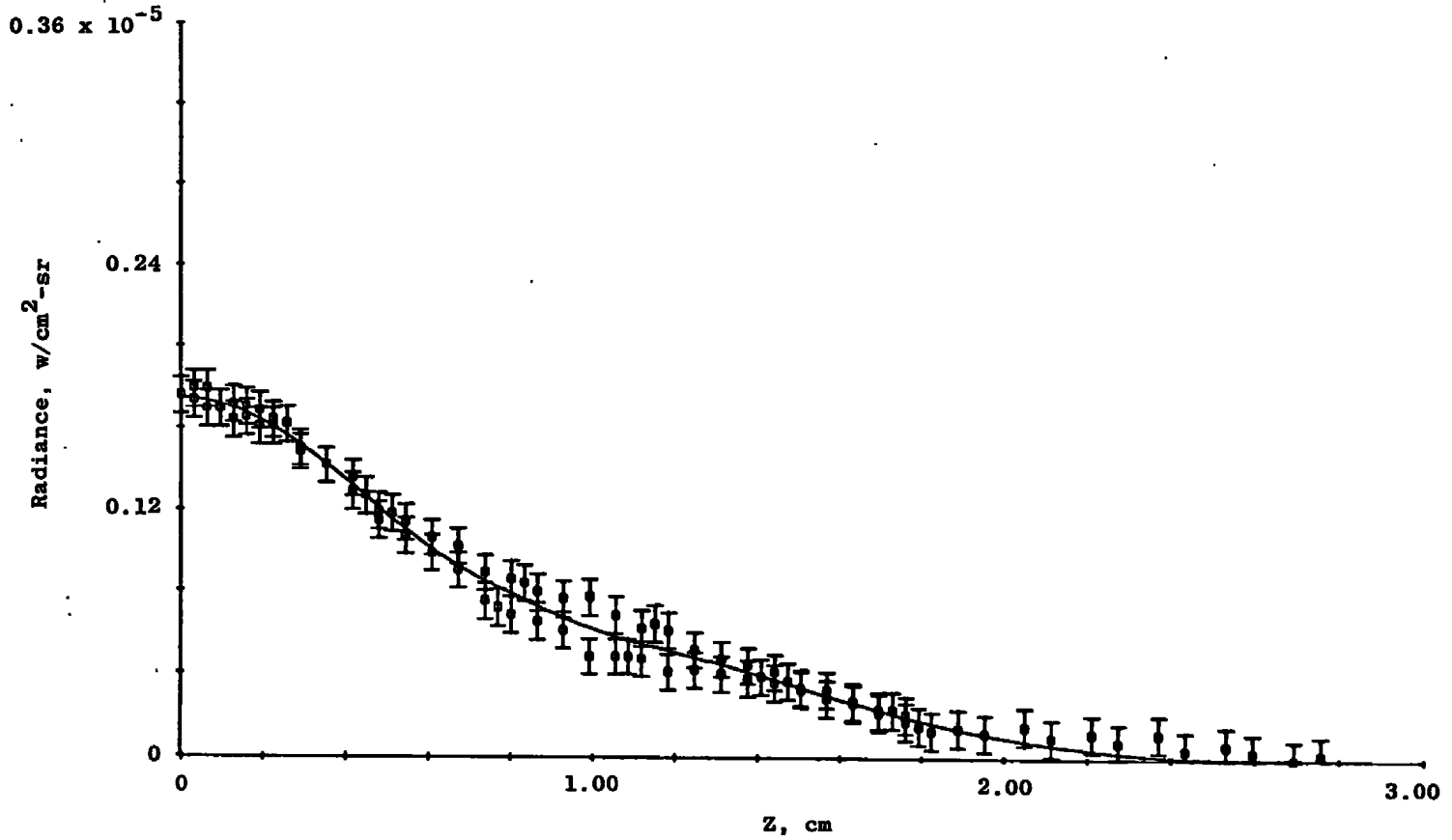
Figure B-11. Spectral radiance at 426.6 nm, X/D = 4.
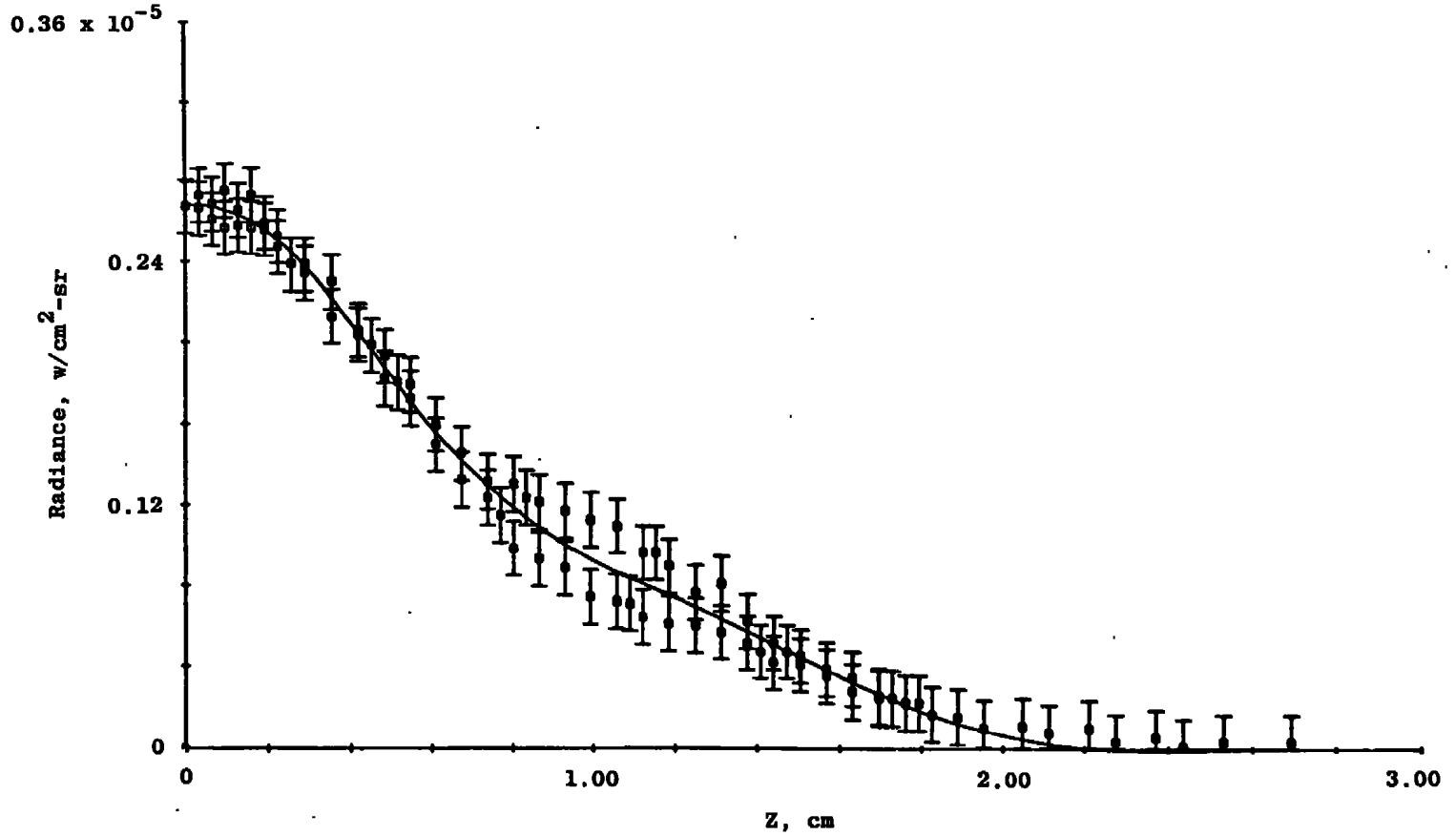
Figure B-12. Spectral radiance at 425.9 nm, X/D = 4.
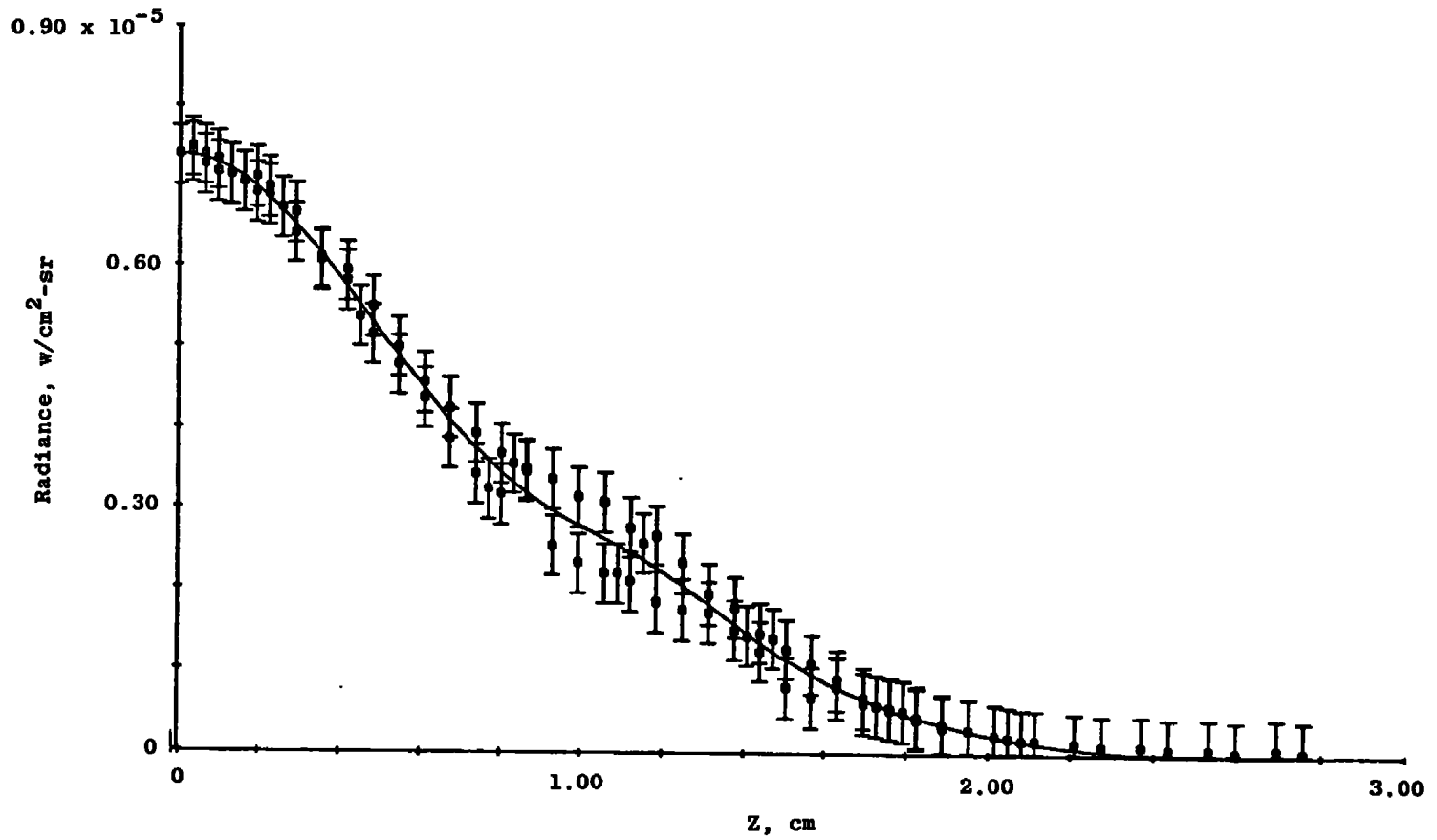
Figure B-13. Spectral radiance at 603.2 nm, X/D = 4.
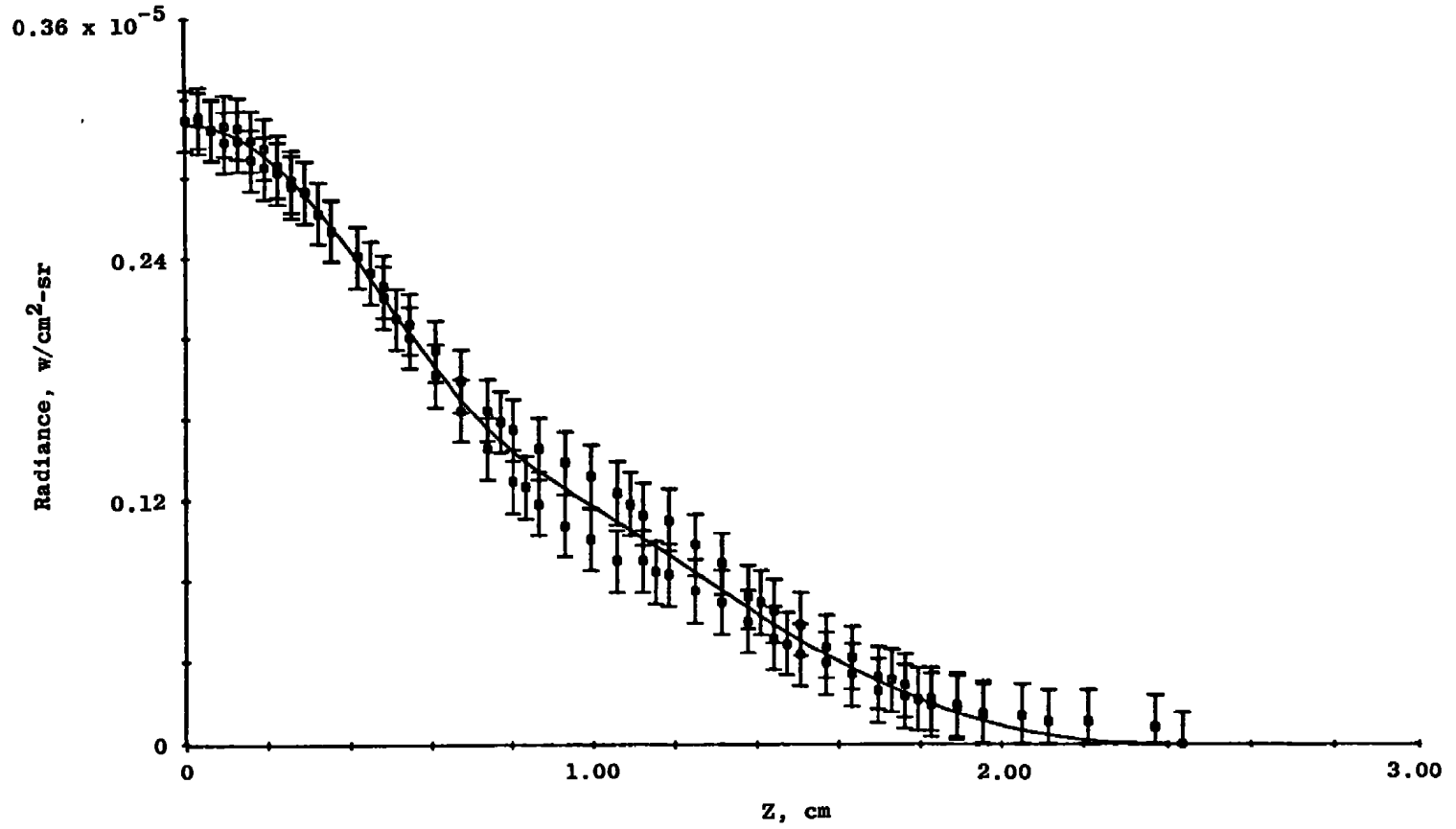
Figure B-14. Spectral radiance at 604.3 nm, X/D = 4.
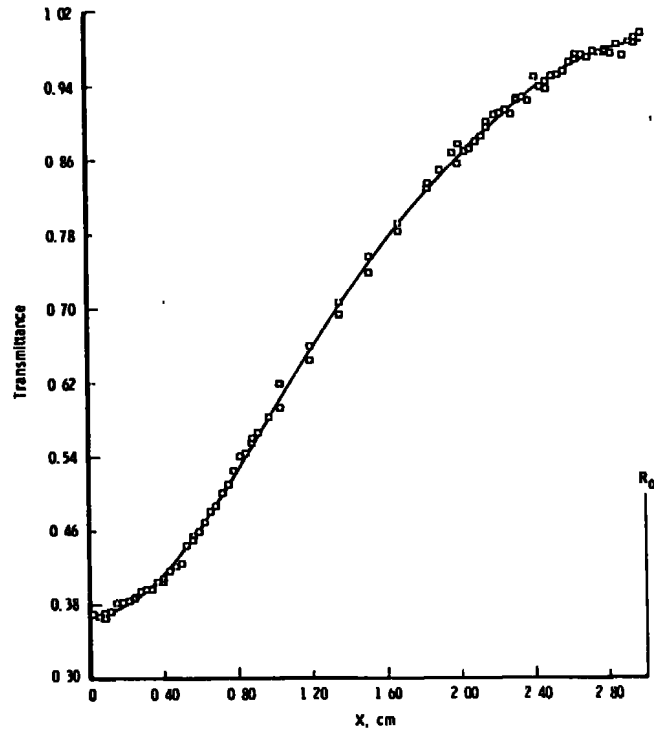
Figure B-15. Transmittance at 763.5 nm, X/D = 2.
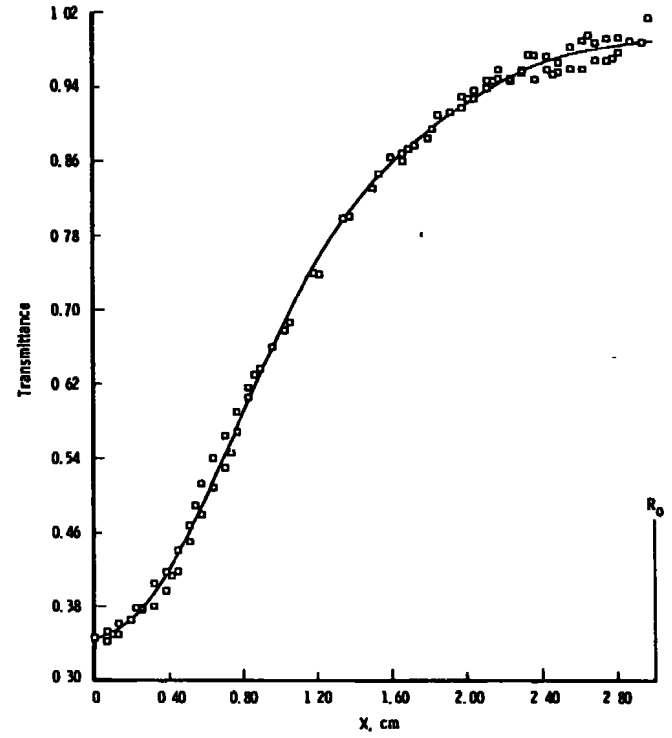
Figure B-16. Transmittance at 751.4 nm, X/D = 2.
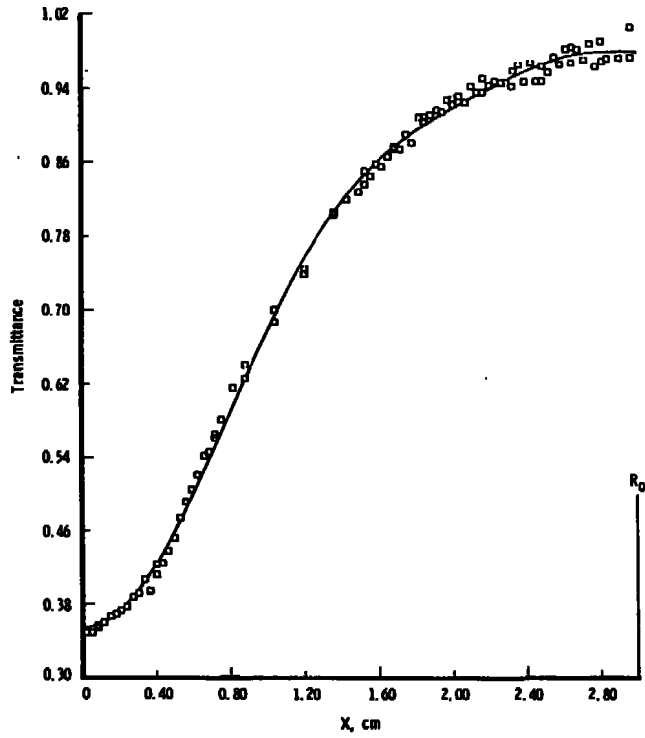
Figure B-17. Transmittance at 738.4 nm, X/D = 2.
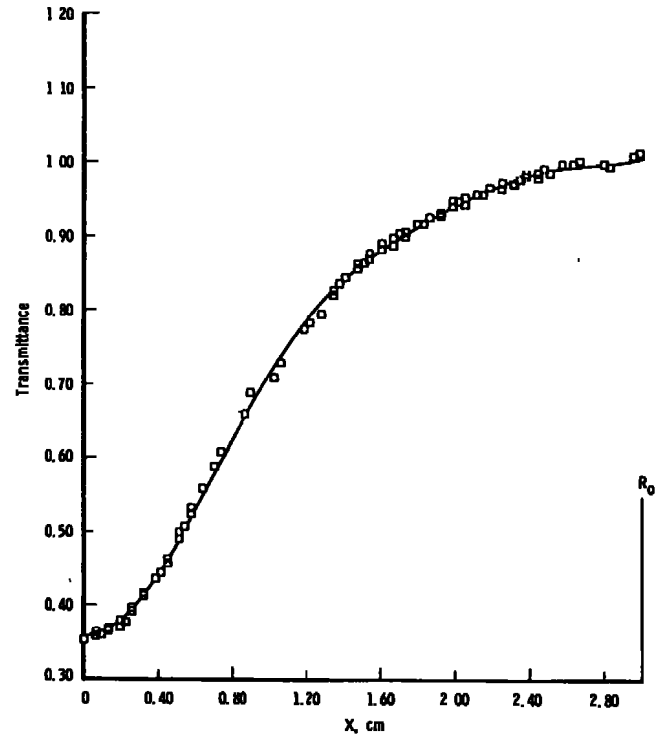
Figure B-18. Transmittance at 772.4 nm, X/D = 2.
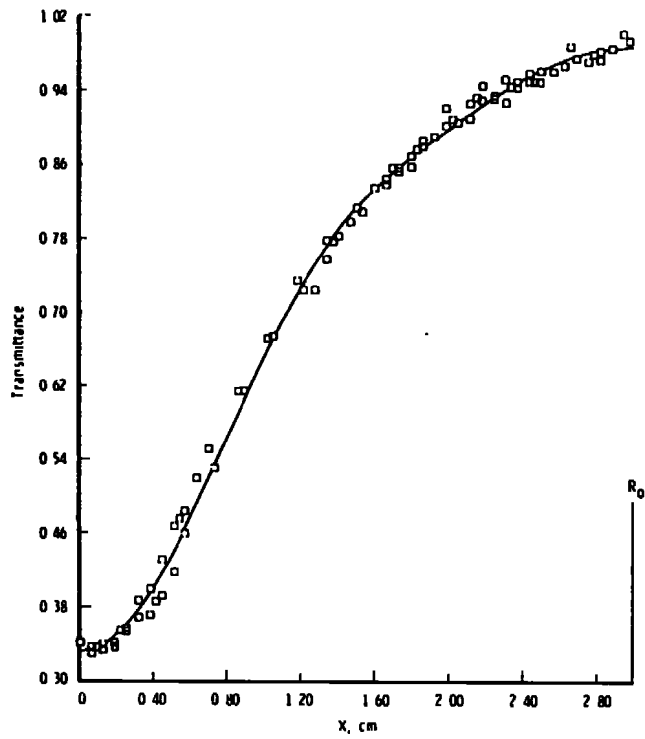
Figure B-19. Transmittance at 794.8 nm, X/D = 2.
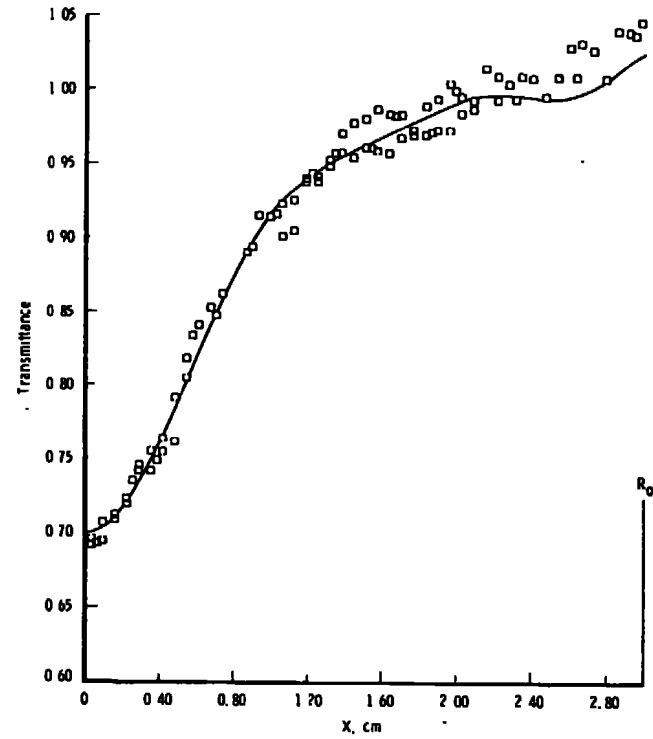
Figure B-20. Transmittance at 750.3 nm, X/D = 2.
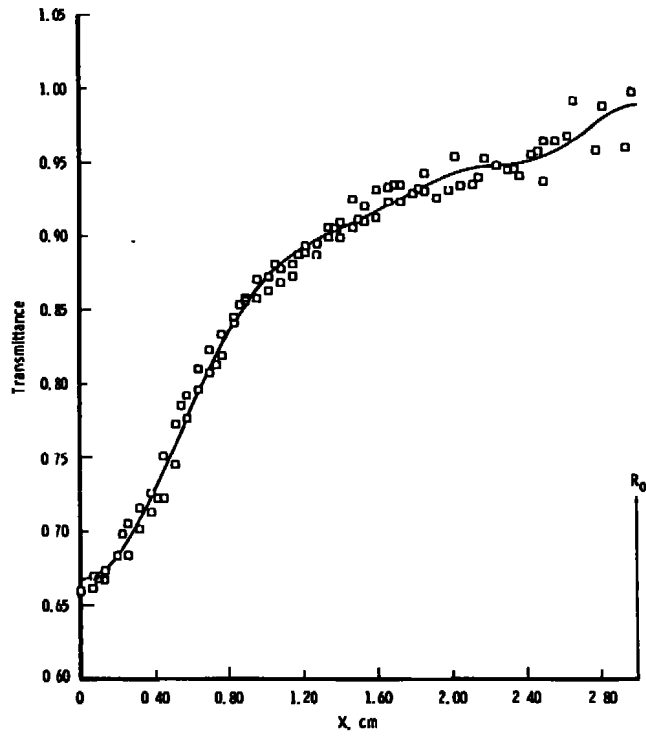
Figure B-21. Transmittance at 922.4 nm, X/D = 2.
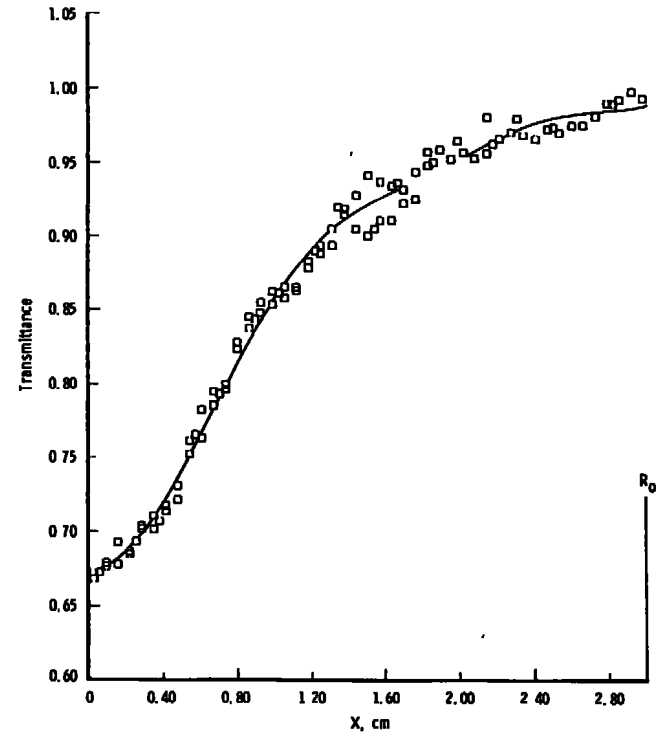
Figure B-22. Transmittance at 840.8 nm, X/D = 2.
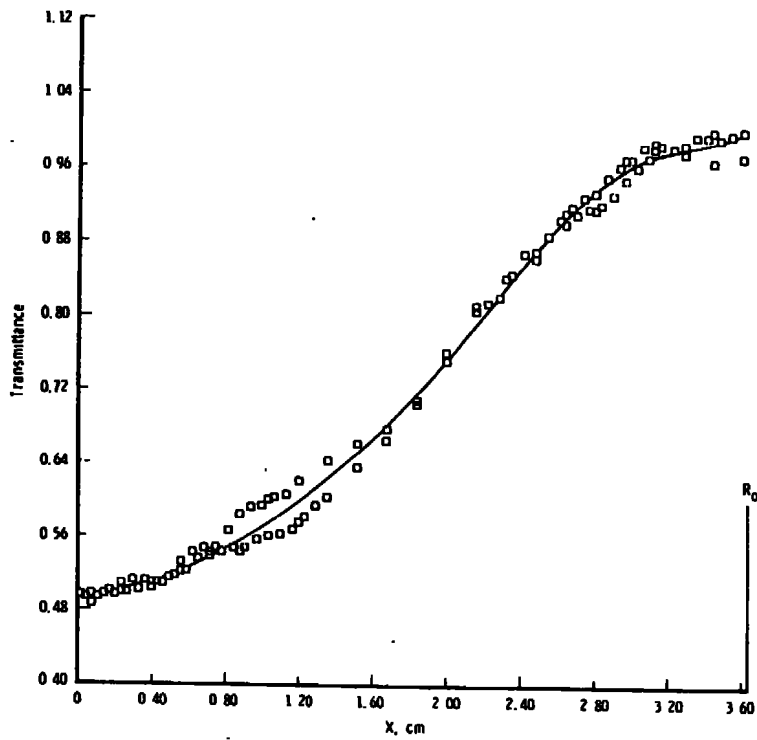
Figure B-23. Transmittance at 763.5 nm, X/D = 4.
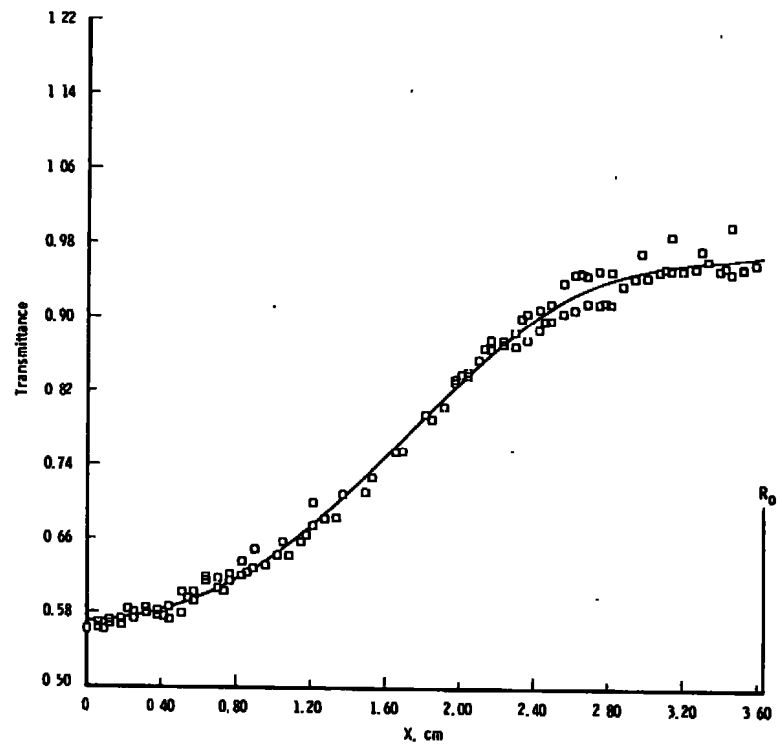
Figure B-24. Transmittance at 751.4 nm, X/D = 4.
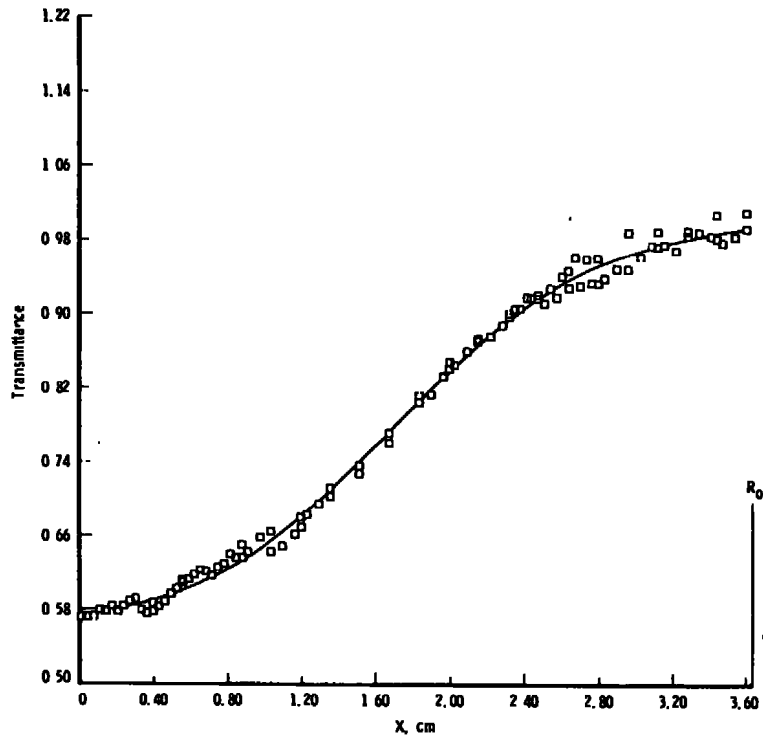
Figure B-25. Transmittance at 738.4 nm, X/D = 4.
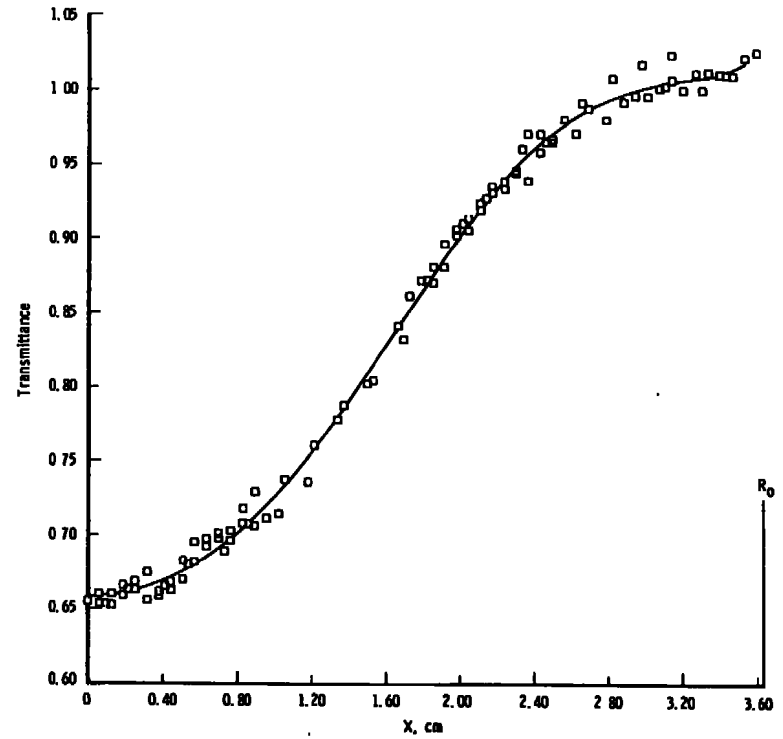
Figure B-26. Transmittance at 772.4 nm, X/D = 4.
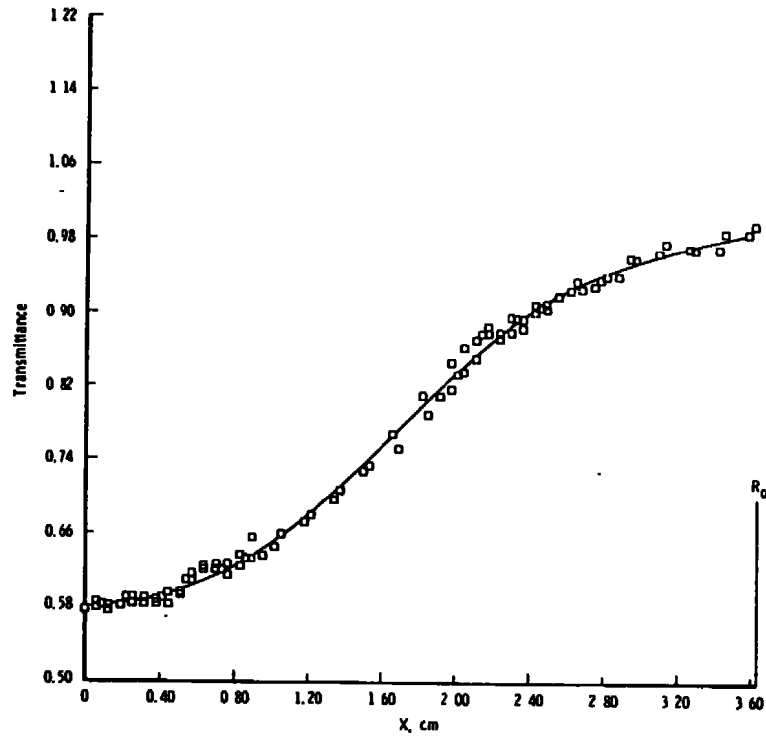
Figure B-27. Transmittance at 794.8 nm, X/D = 4.
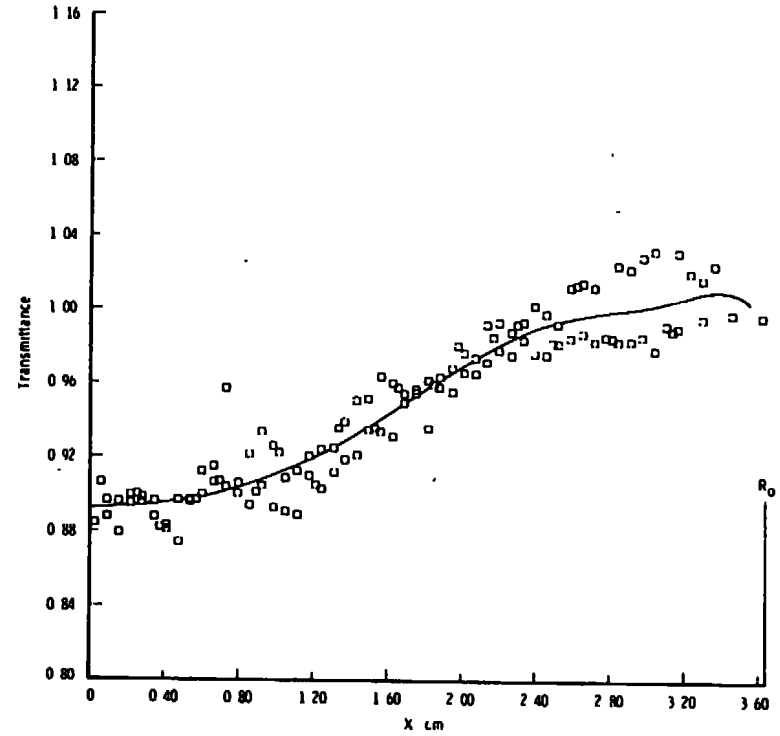
Figure B-28. Transmittance at 750.3 nm, X/D = 4.
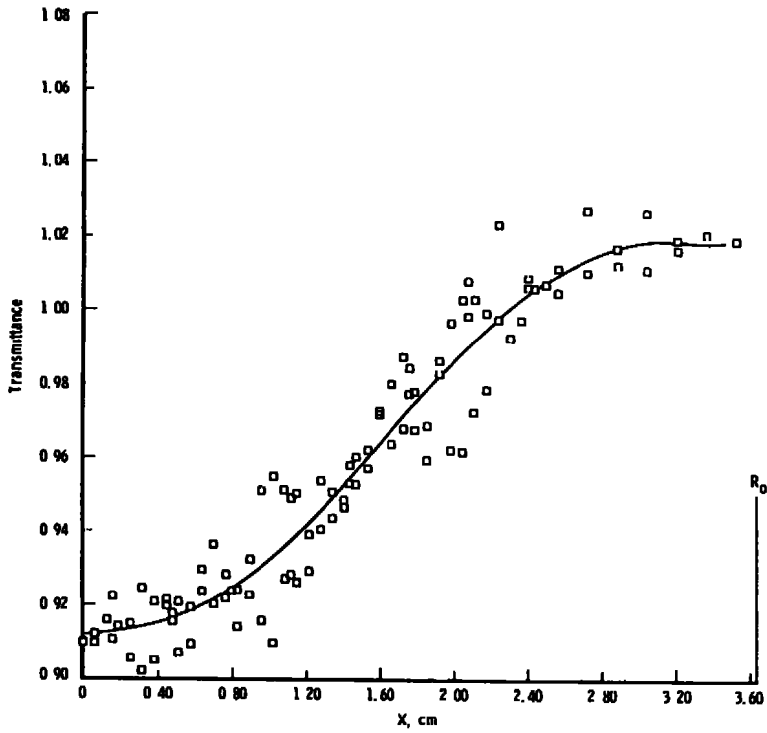
Figure B-29. Transmittance at 922.4 nm, X/D = 4.
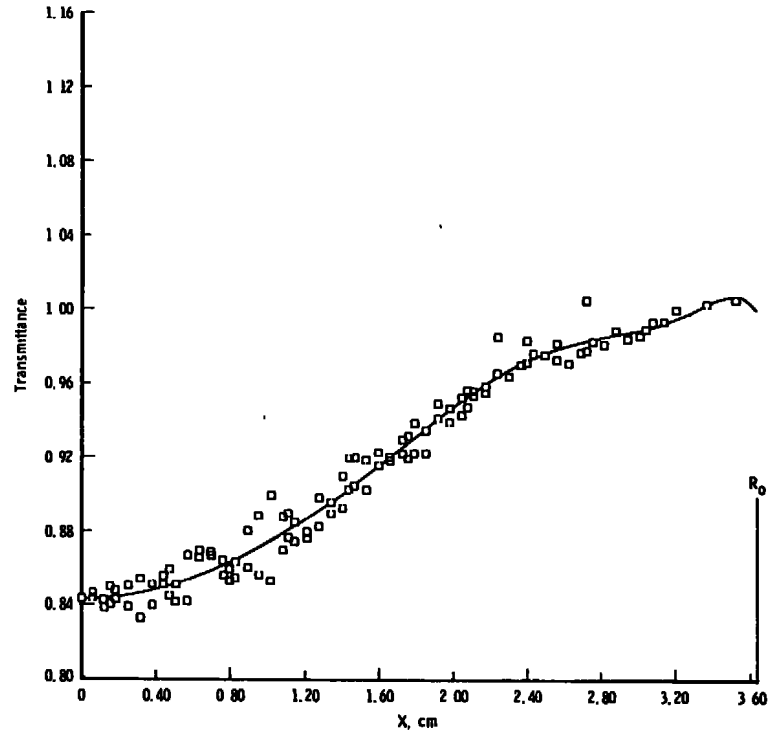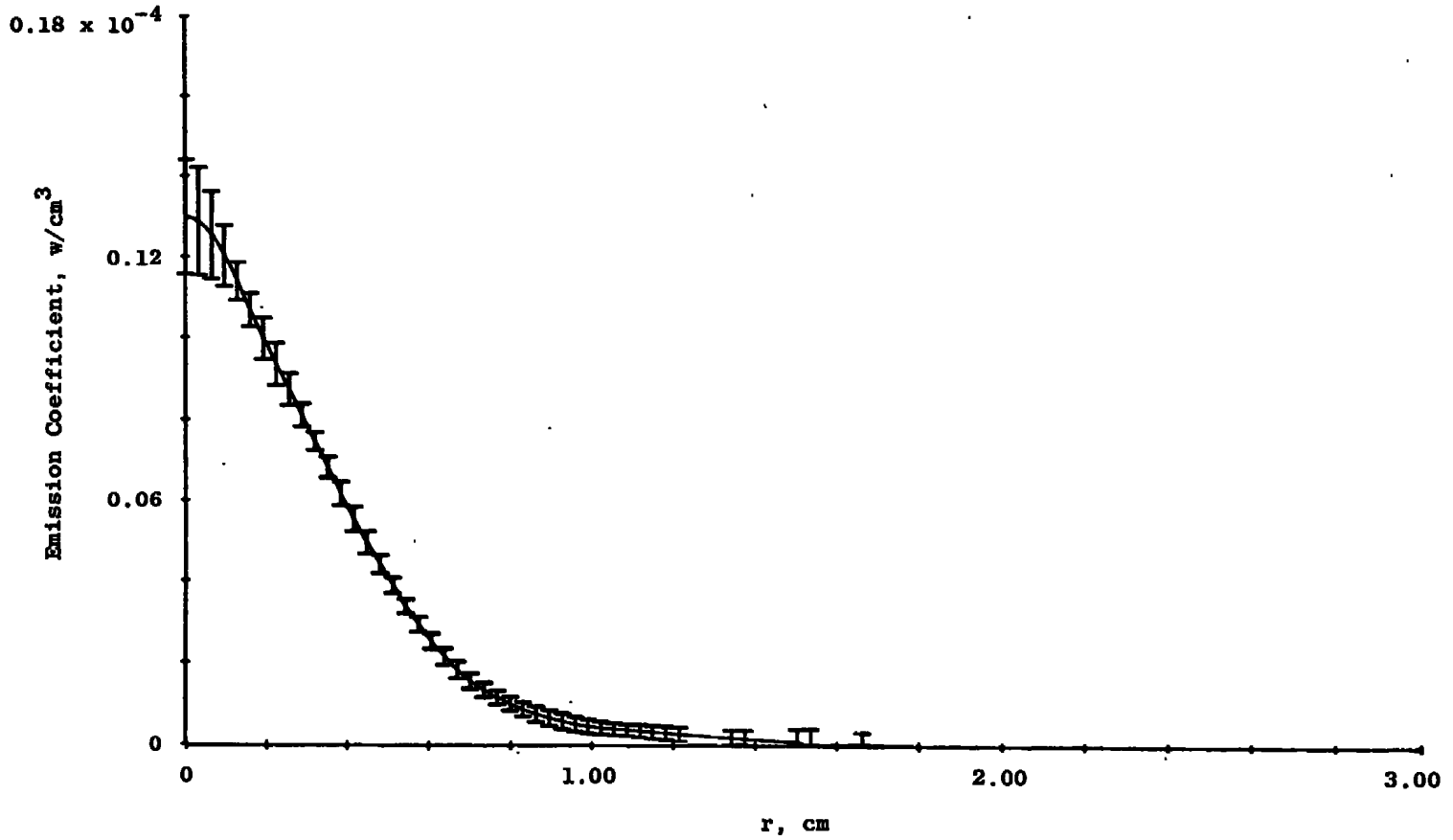

Figure B-30. Transmittance at 846.8 nm, X/D = 4.
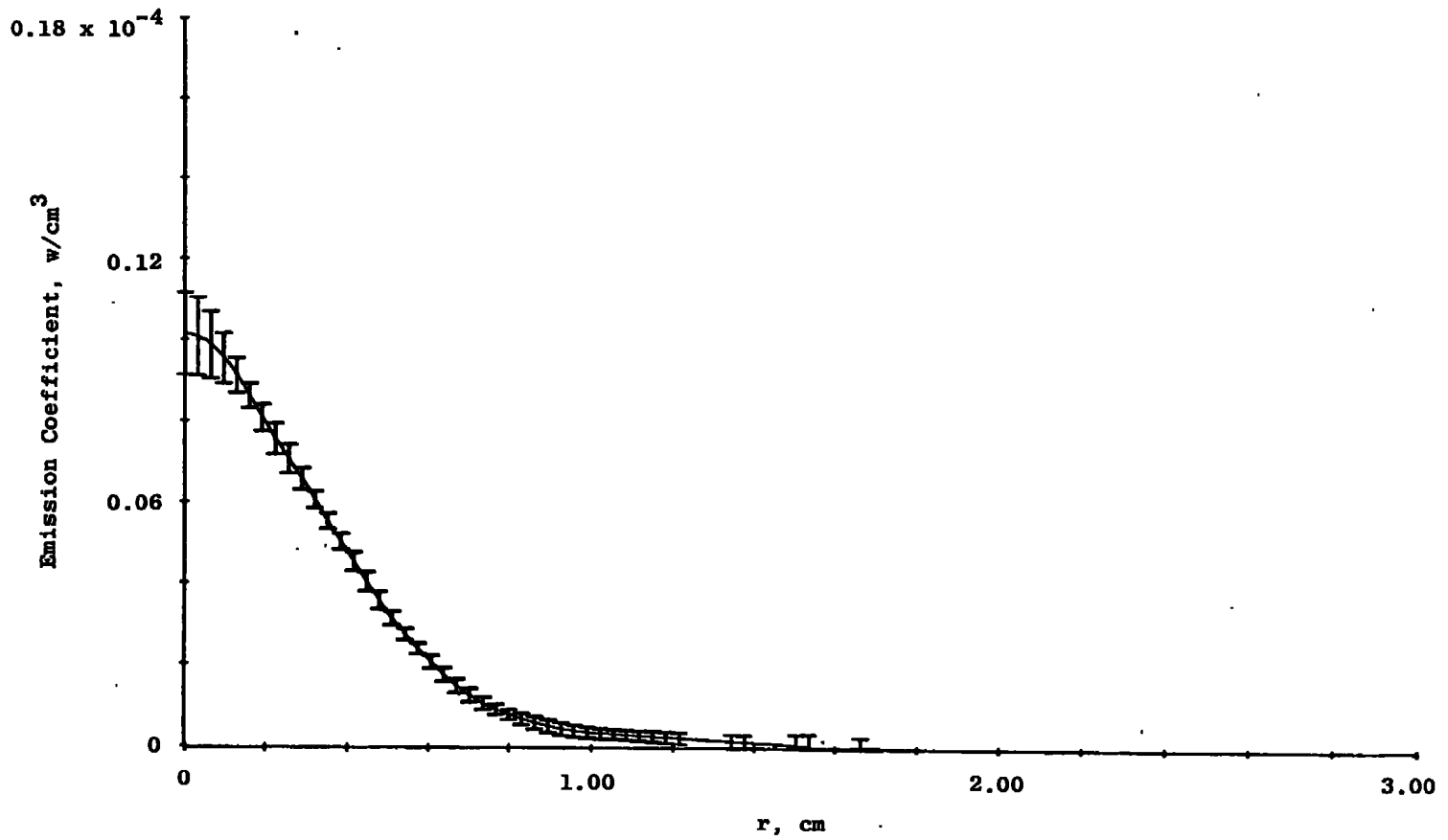
Figure B-31. Emission coefficient profile at 430.0 nm, X/D = 2.
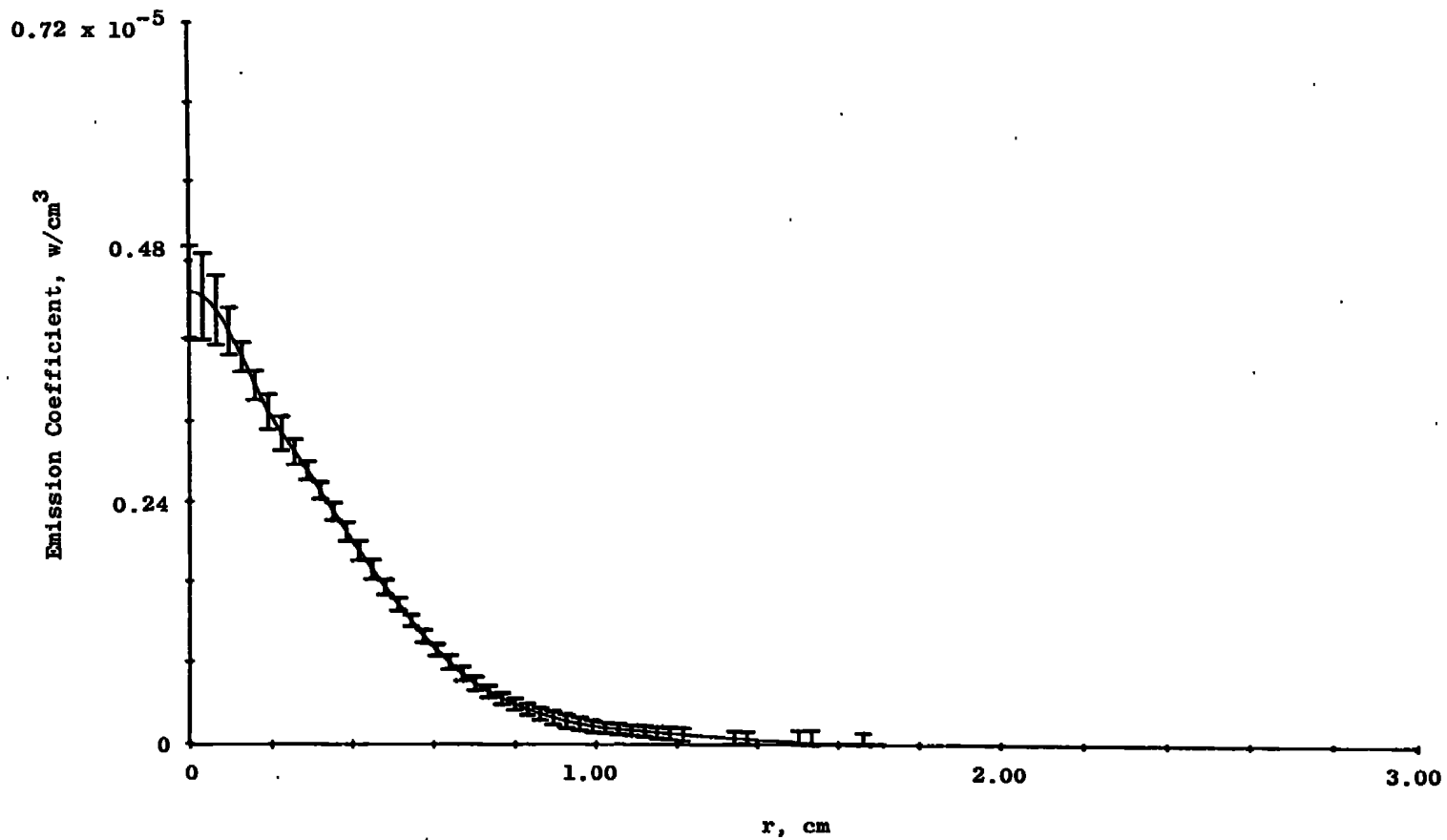
Figure B-32. Emission coefficient profile at 416.4 nm, X/D = 2.
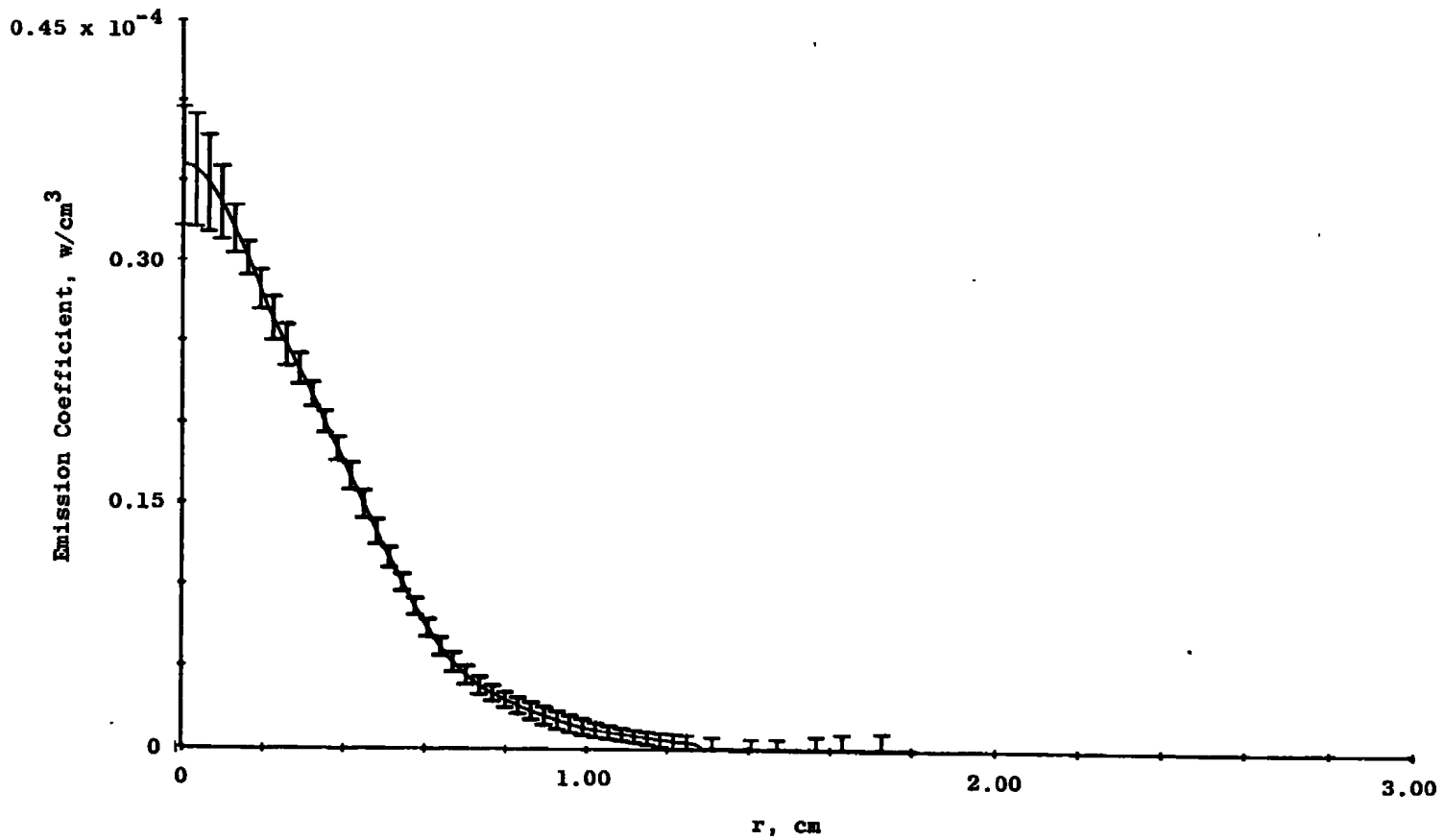
Figure B-33. Emission coefficient profile at 415.8 nm, X/D = 2.
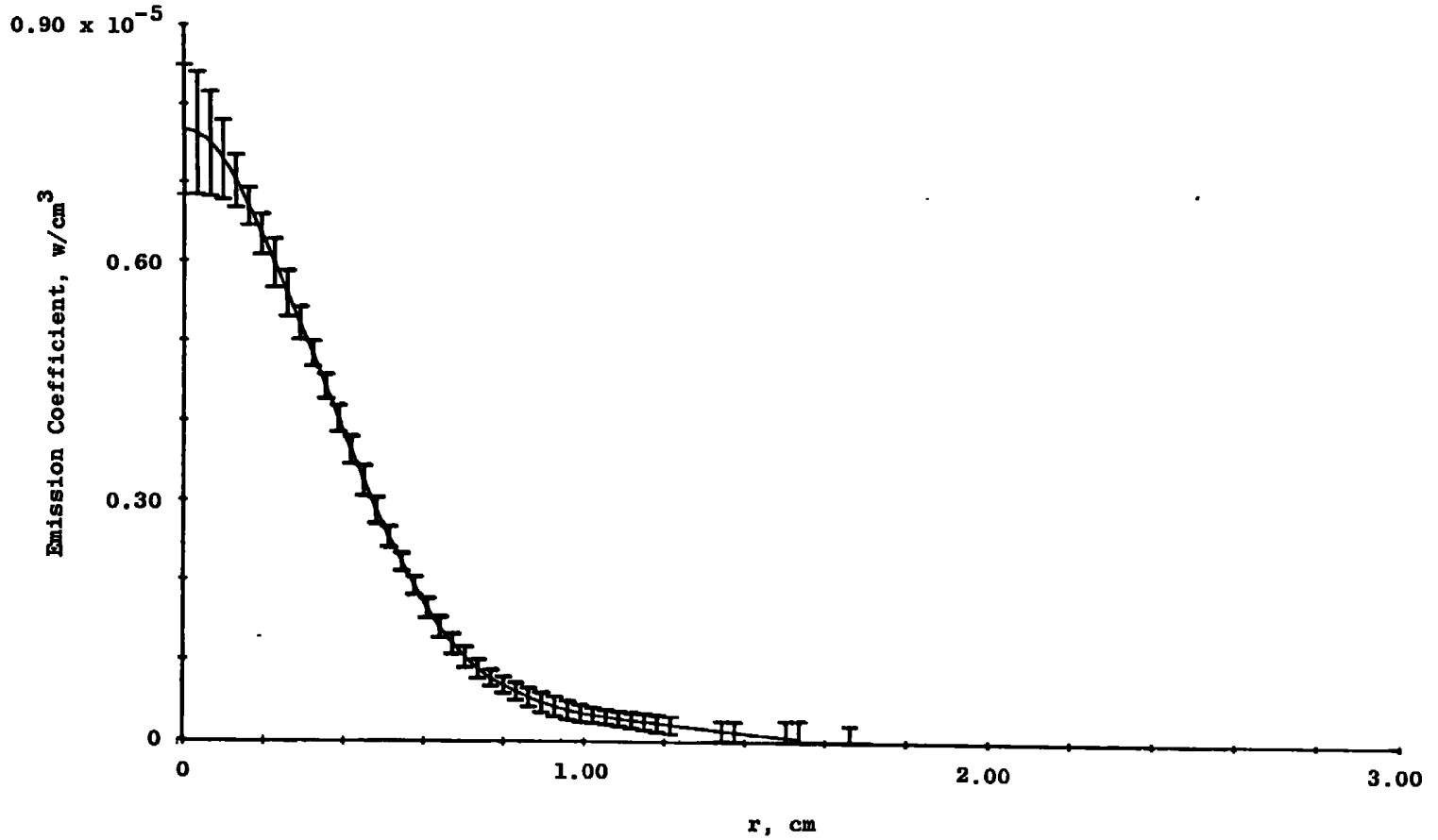
Figure B-34. Emission coefficient profile at 426.6 nm, X/D = 2.

Figure B-35.   Emission coefficient profile at 425.9 nm, X/D = 2.
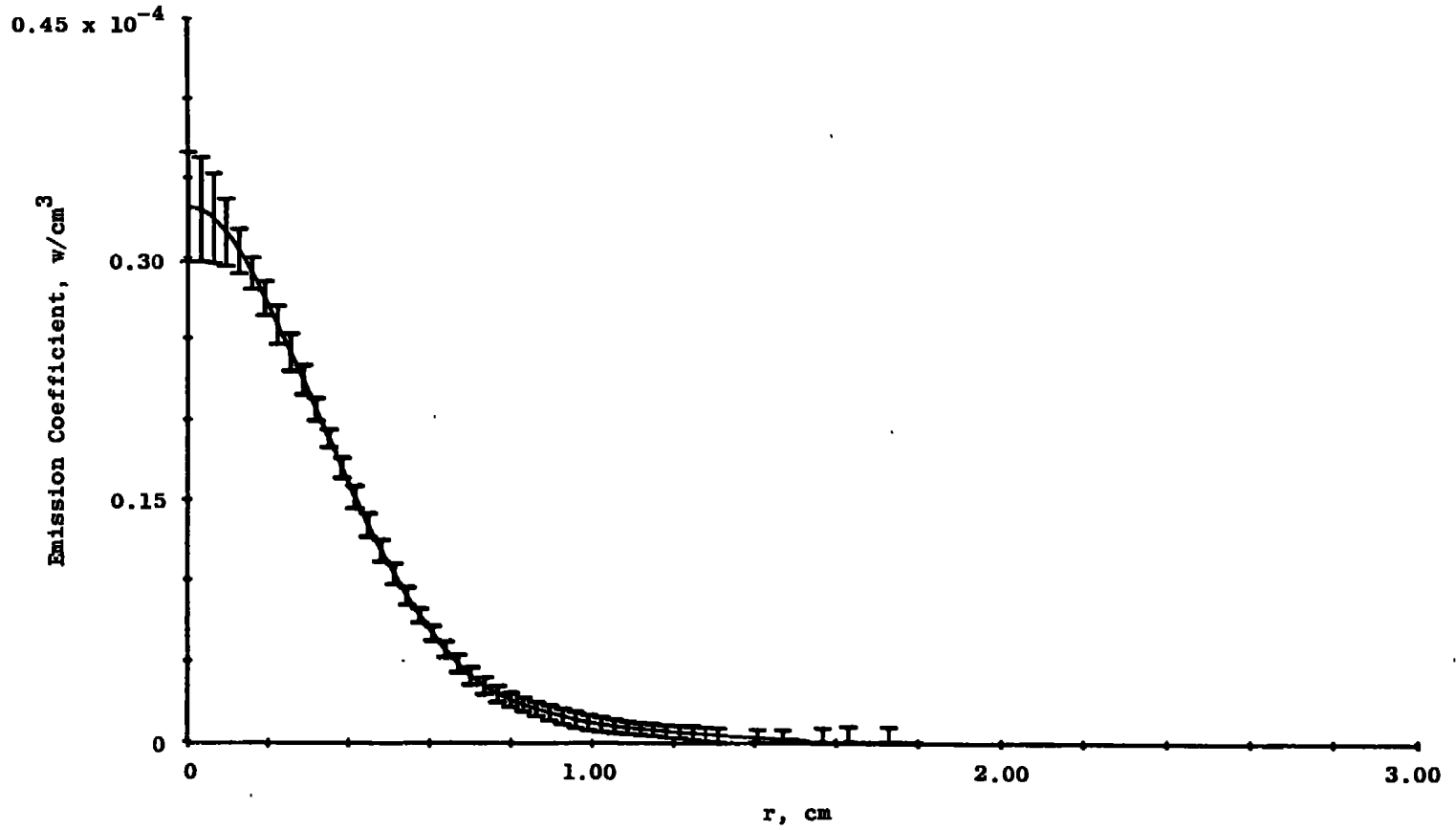
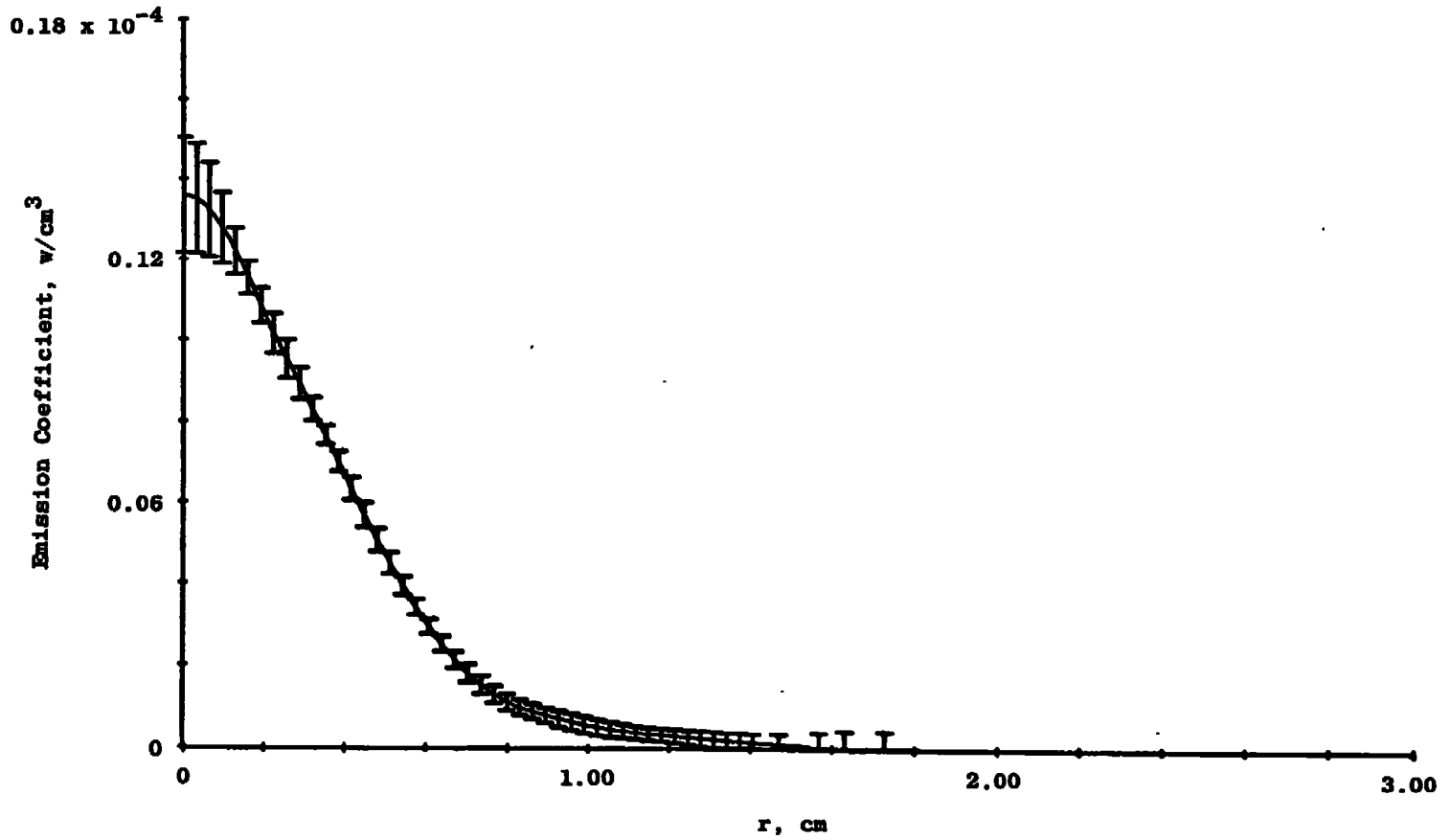Figure B-36. Emission coefficient profile at 603.2 nm, X/D = 2.

Figure B-37. Emission coefficient profile at 604.3 nm, X/D = 2.
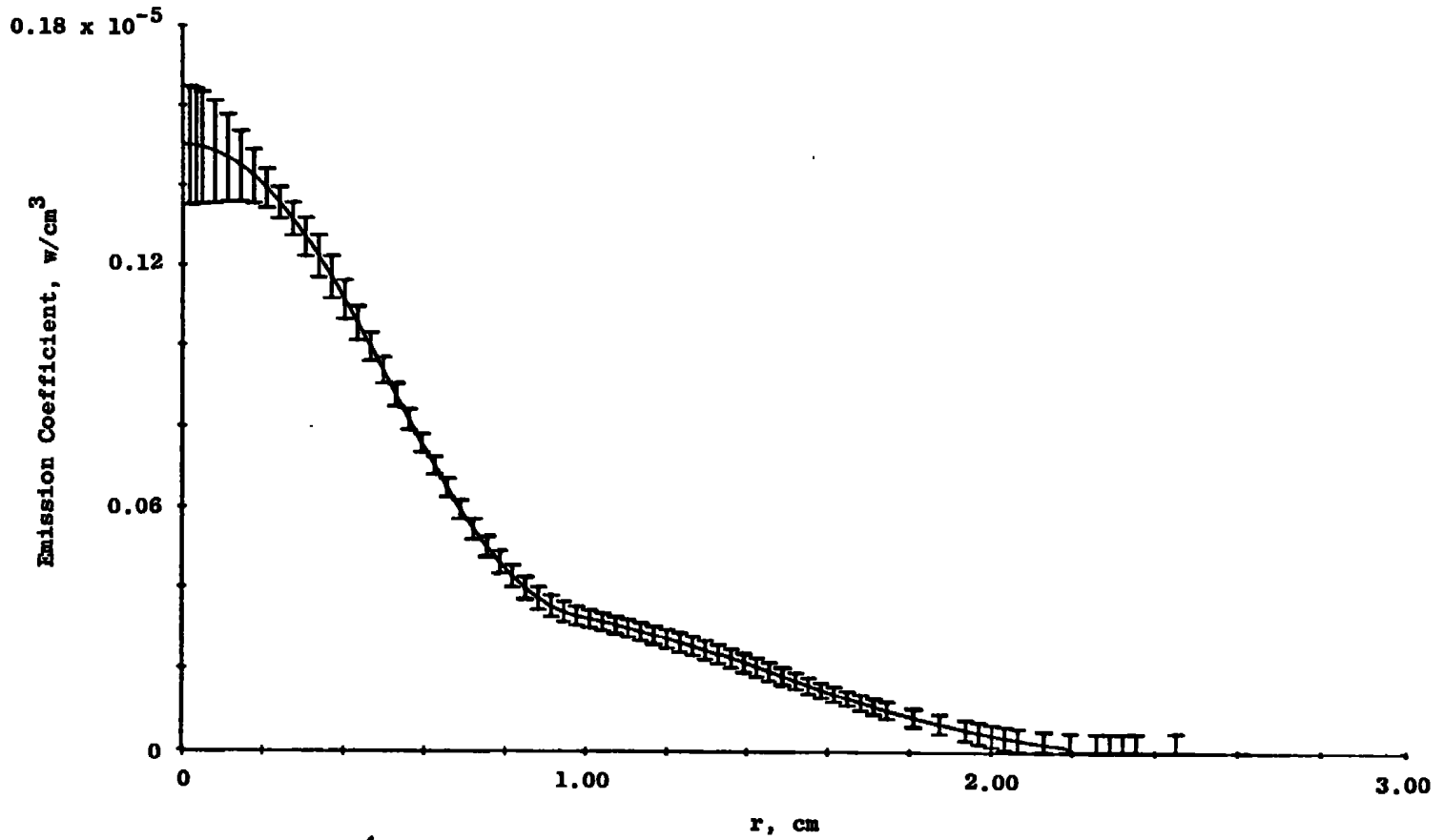
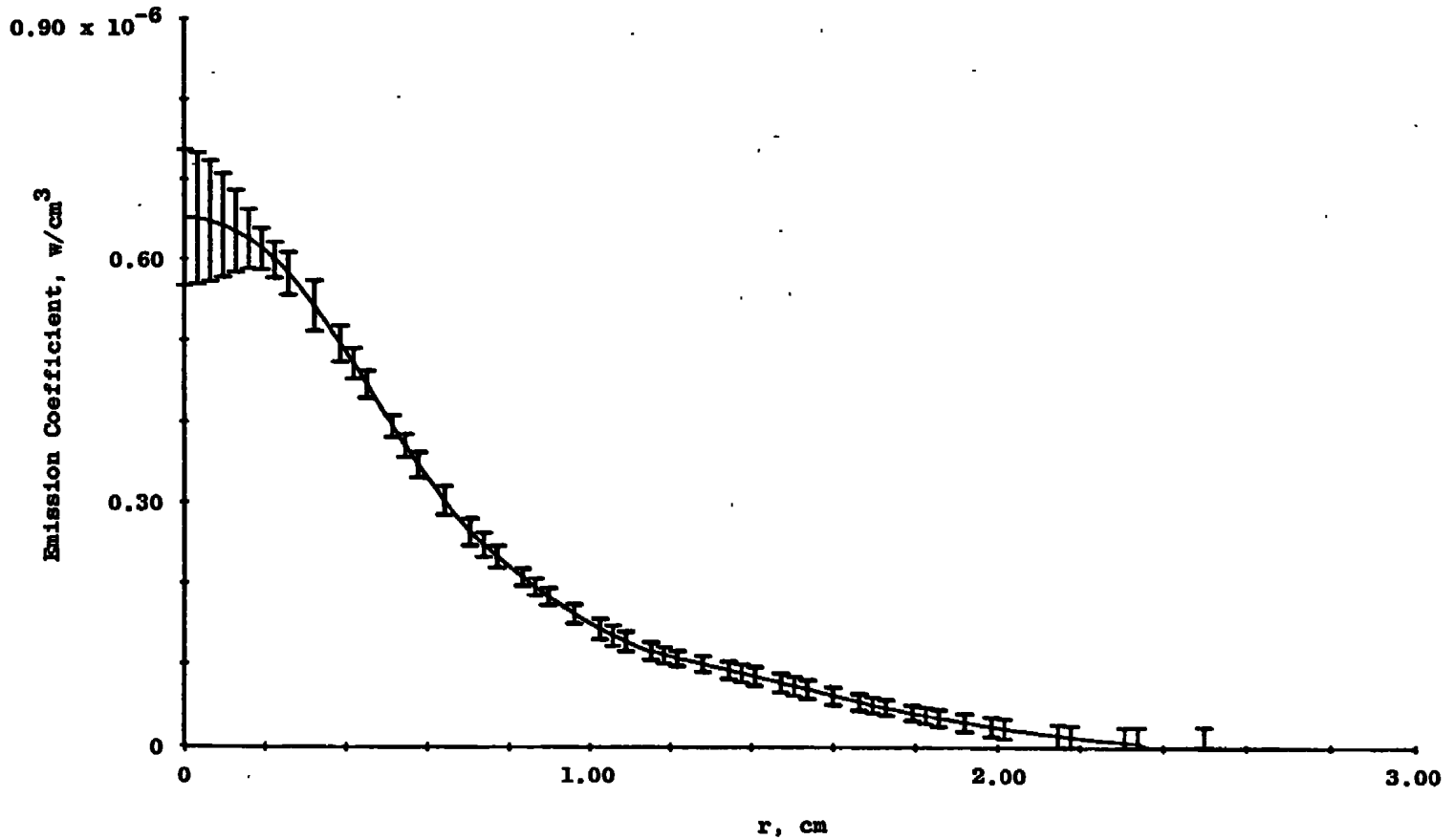Figure B-38.   Emission coefficient profile at 430.0 nm, X/D = 4.

Figure B-39. Emission coefficient profile at 416.4 nm, X/D = 4.
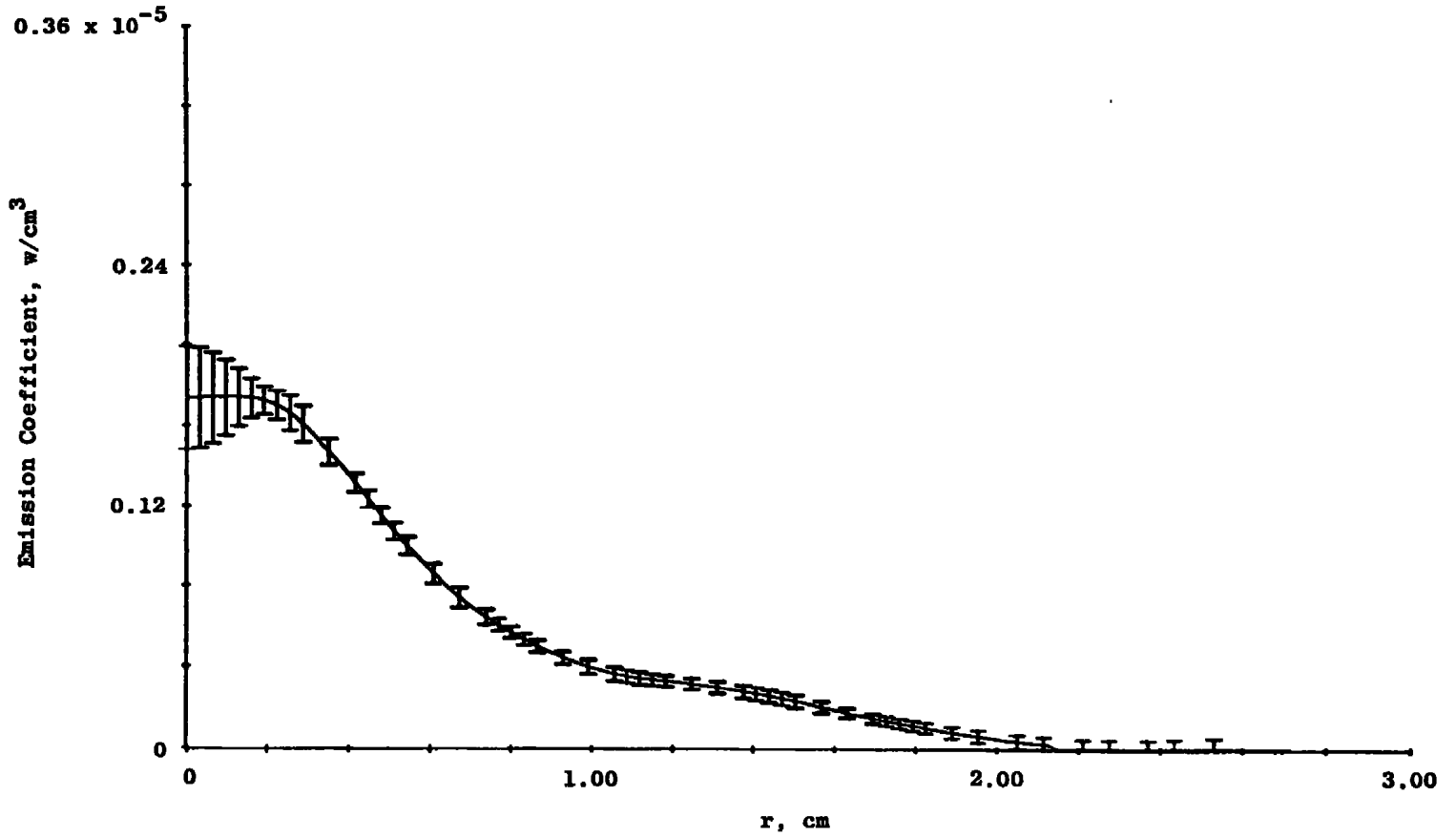
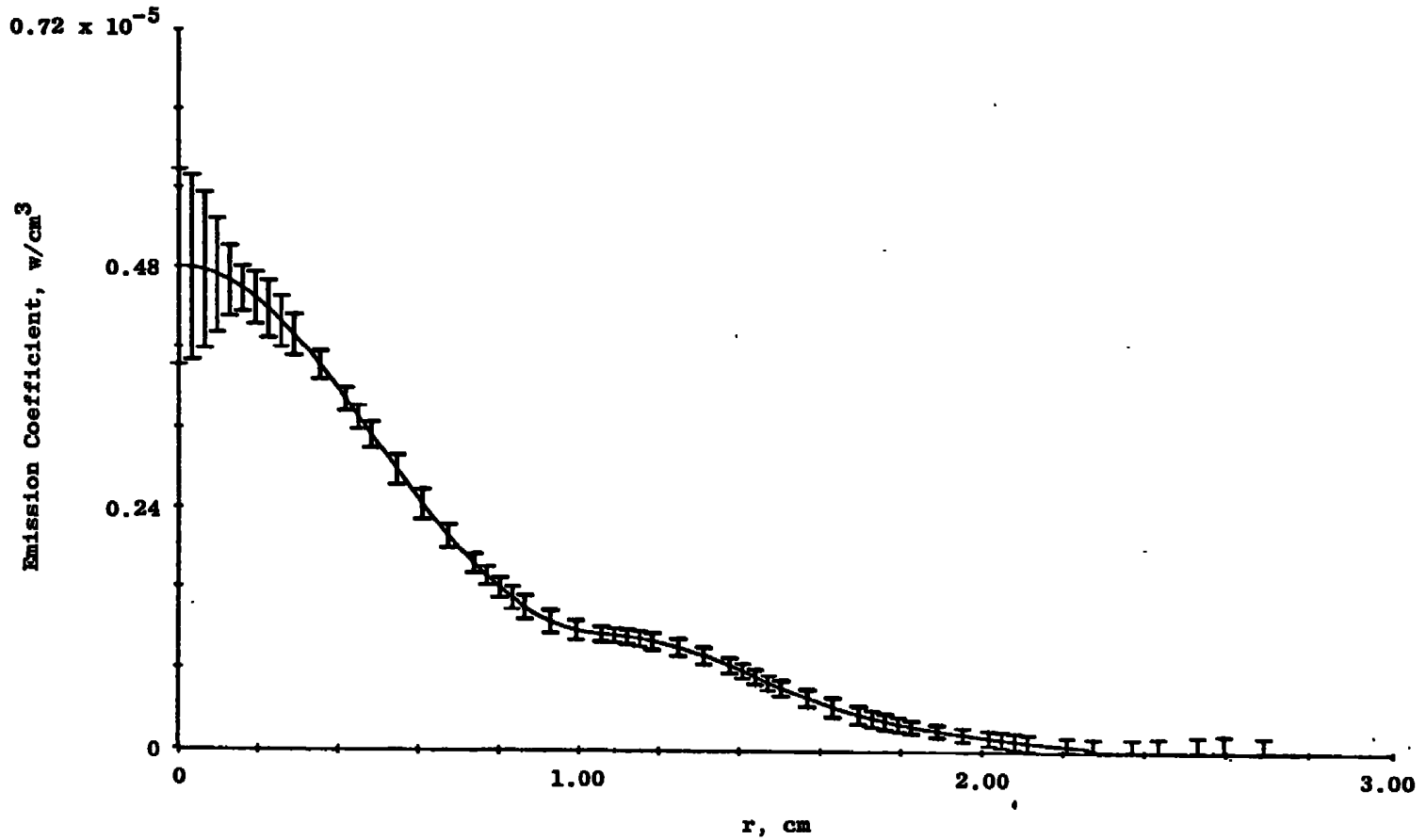Figure B-42.   Emission coefficient profile at 425.9 nm, X/D = 4.

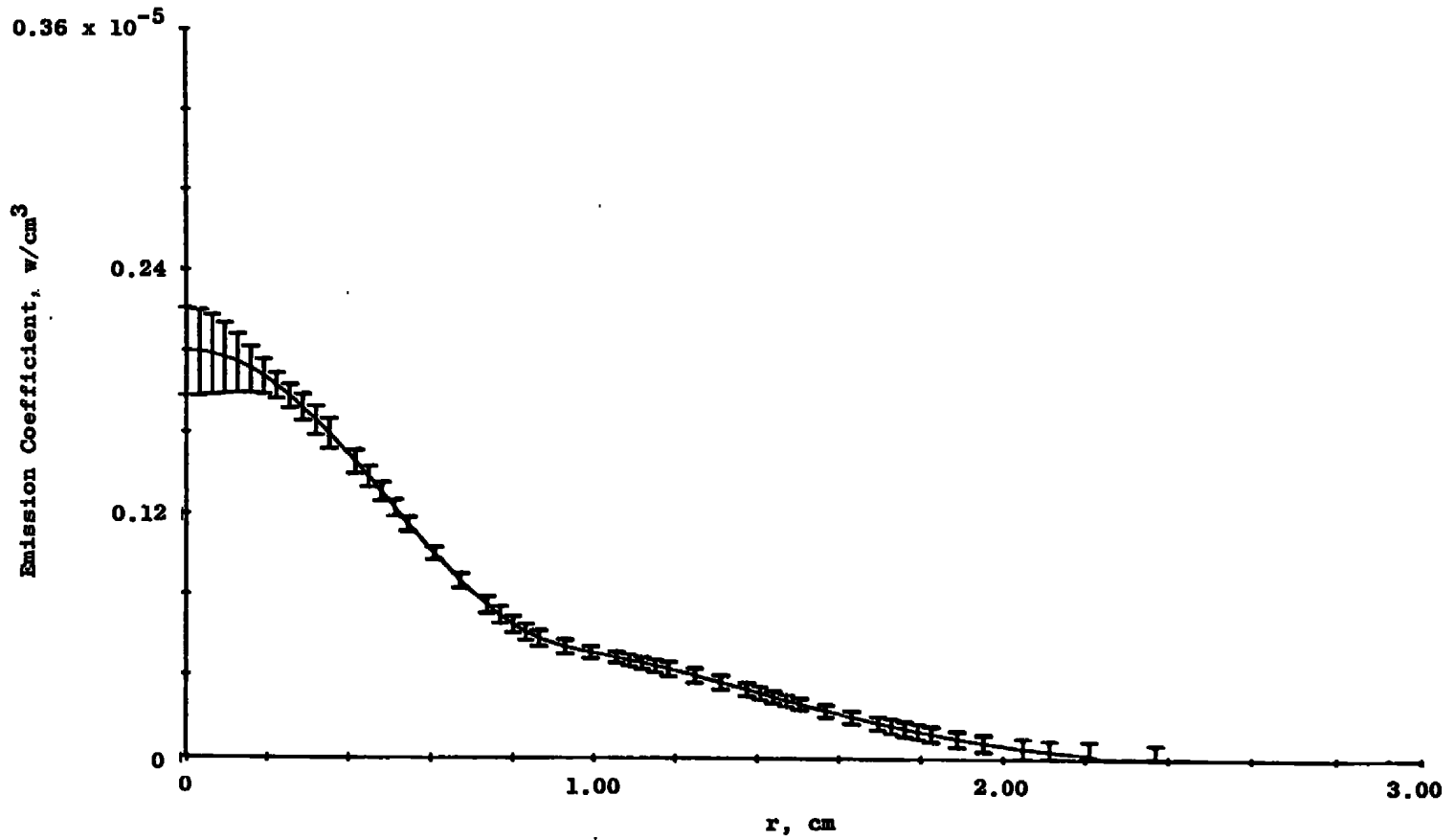Figure B-43. Emission coefficient profile at 603.2 nm, X/D = 4.

Figure B-44. Emission coefficient profile at 604.3 nm, X/D = 4.

NOMENCLATURE

A	Empirical constant in Ashkenas-Sherman relation
$A(p;q)$	Einstein spontaneous radiation probability, $\sec^{-1}$
C	Empirical constant in Ashkenas-Sherman relation
C_o, C_1, C_2	Symbollically represents collection of terms defined in Appendix A
c	Speed of light
D	Nozzle diameter, cm
e	Charge on electron
$F(\nu), G(\nu), H(\nu)$	Convenient collection of functions defined in Appendix A
f	Oscillator strength
g	Statistical weight
h	Planck's constant
$\left.\begin{array}{l} I \\ I_\nu \\ I_o \\ I_{\nu_o} \\ I_{\nu_o}^o \end{array}\right\}$	Radiance, $w/cm^2/sr$
I_p, I_q	Ionization potential, cm^{-1}

$K(c;p)$ Three-body recombination rate coefficient, cm^6/sec

$K(p;c)$ Electron-atom collisional ionization rate coefficient, cm^3/sec

$K(p;q)$ Electron-atom collisional rate coefficient, cm^3/sec

k Boltzmann constant

k_ν Absorption coefficient, cm^{-1}

ℓ Absorption path length, cm

M Mach number

M_a Mass of absorber species, gm

M_s Mass of source species, gm

m_e Mass of electron, gm

N_a Number density of absorber species

P_o Stagnation pressure at nozzle exit, torr

p,q Used to symbollically identify quantum states

Q Cross section, cm^{-2}

R Gas constant, erg/°K

R_o Outer plume radius, cm

r	Radius, cm
T	Temperature, °K
T_o	Stagnation temperature at nozzle exit, °K
t	Time, sec
X	Axial position, cm
X_o	Empirical constant in Ashkenas-Sherman Relation
Z	Displacement perpendicular to axis, cm
α	Collisional-Radiative recombination rate coefficient, cm^6/sec
$\beta(p)$	Electron-ion recombination rate coefficient, cm^3/sec
γ	Ratio of specific heats
ϵ	Emission coefficient, $w/cm^3/sr$
ν	Frequency, sec^{-1}
ν_o	Central frequency of spectral line, sec^{-1}
ρ_o	Stagnation density at nozzle exit, g/cm^3
τ	Transmittance

SUPERSCRIPT

+   Denotes ion properties

SUBSCRIPTS

e   Denotes electron properties

s   Static properties or source molecule properties

i,j   Dummy subscripts